DISSERTATION

THE USE OF COORDINATING SOLVENTS IN GOLD CLUSTER SYNTHESIS

Submitted by

W. Scott Compel

Department of Chemistry

In partial fulfillment of the requirements

For the Degree of Doctor of Philosophy

Colorado State University

Fort Collins, Colorado

Summer 2016

Doctoral Committee:

Advisor: Christopher J. Ackerson

Richard Finke
Diego Krapf
Amy Prieto
Melissa Reynolds

ABSTRACT

THE USE OF COORDINATING SOLVENTS IN GOLD CLUSTER SYNTHESIS

Monolayer-protected clusters (MPCs) are nanoparticles *ca*. 1-3 nm in diameter composed of a metal core and an organic monolayer shell. In this size range MPCs are larger than metal-ligand complexes but too small to exhibit a surface plasmon resonance. The electronic structures of particles in this size regime resemble discrete molecular orbital energy levels as opposed to the band-like behavior observed in larger, plasmonic nanoparticles. MPCs are composed of ten to a few hundred atoms and can be characterized as simple chemical compounds with discrete molecular formulae as opposed to average particle diameters. In these systems, addition or removal of a single metal atom profoundly affects stability and observed properties. This phenomenon gives rise to an exceptionally diverse class of materials with seemingly endless potential evolving from minute compositional changes.

Thiolate-protected gold clusters are exemplary MPCs due to their intrinsic high stability that allows for long-term studies and post-synthetic modification. These clusters exhibit unique physiochemical properties that allow for potential applications in electronics, catalysis, biomedicine, and sensing. The past two decades since their discovery brought about a significant body of research regarding the origin of Au cluster properties and total structure elucidation. However, modern approaches for Au cluster synthesis produce polydisperse mixtures of clusters that must undergo extensive postreaction ripening or fractionalization to obtain a pure, single product. New synthetic approaches for monodisperse Au clusters in high yield must be developed before their applications may be realized.

The motivation behind this work was to explore the issue of polydispersity in Au cluster synthesis. Through combinatorial screening of synthetic co-solvent systems we find that synthesis in coordinating solvents (*i.e.*, glymes) greatly enhances the monodispersity of Au cluster products. During synthesis, glyme chelates the metal in the metallopolymer precursor and modifies the surface of the resulting particle, resulting in a new series of metastable Au clusters. The synthetic methods presented herein result in pure, single products in high yield. The surface modification brought about by diglyme potentially renders the clusters available for single-ligand functionalization to tailor cluster properties for desired functionality. The products are evaluated for biomedical and sensing applications.

ACKNOWLEDGEMENTS

In all honesty, I never planned on graduating from CSU. I thought a Ph.D. was beyond my grasp and unnecessary for the career I desired. Fortunately for me, I met some amazing people that saw potential in me and pushed me to continue on through all the struggles. These people have made me a better scientist and a better person.

My family has been incredibly supportive throughout this entire process. You all inspire me to keep trying harder despite all logical reasoning that indicates failure. I'm not sure if this is a disability or an advantage, but we sure do excel at it.

I owe all of my success in graduate school to my mentors that molded me into the scientist I am today. Chris Ackerson is unquestionably the best mentor I could have possibly worked for; nobody else could put up with my stubborn approach towards science and still help me out of the holes I would dig myself into. Your lab is the goofiest, most creative work environment I've ever been a part of, and I am sad that it is time for me to leave it. Andrea Wong taught me how to approach scientific problems both rationally and with shortsighted fervor. Thank you both for helping me develop my potential into work I am proud of today. I could never imagine my life without the people I have worked with in the Ackerson lab, especially Thomas Ni for being so incredibly helpful and gosh darn silly all the time.

All the faculty and staff at CSU have been overwhelmingly supportive. I am especially thankful for Amy Prieto who set aside an unreasonable amount of time to advise me. I also need to thank Ron Costello, not only for keeping our building standing but also for constantly reminding me that there is more to work than science.

The friends I have made the past five years, in and out of CSU, are some of the best people I have ever met. The times we shared together more made up for all of the low punches chemistry had to offer. I am especially grateful to Marcus, Everett, Wil, and Nicole, who were central to nearly every life-changing experience I have had here. The adventures we shared have had such a profound impact on my life; I can say without fail that I would be a drastically different person, for the worse, had I not met any one of you. I am so excited to watch you all shape the world, and I can't wait until our paths cross again.

Let's go exploring!

Dr. W. Scott "the manhammer" Compel

TABLE OF CONTENTS

CHAPTER 1

An Introduction to Thiolate-Protected Gold Nanoclusters

1.1 Synopsis:

The overarching theme of this dissertation is the synthetic development of thiolate-protected gold nanoclusters. Traditional Au cluster synthesis results in polydisperse products that must be purified, etched, annealed, or size-focused to give atomically precise clusters. New synthetic approaches for monodisperse Au clusters in high yield must be developed before their applications in electronics, catalysis, biomedicine, and sensing may be realized.

The goal of this work is the development of a direct-synthesis approach for pure Au clusters by optimizing solvent composition for narrow product dispersion. The primary hypothesis is that synthesis in coordinating solvents (*i.e.*, glymes) greatly enhances the monodispersity of Au cluster products. During synthesis, glyme is expected to chelate the metal in the metallopolymer precursor and modify the surface of the resulting particle. These combined effects establish a new series of stable Au cluster "magic" sizes capable of forming in high yield through a direct-synthesis approach.

1.2 Research Approach:

1) Chapter 2 presents a combinatorial screen of organic solvents and solvent concentration to explore unexpected roles of solvent in Au cluster synthesis. Two modes of solvent effects are observed: coordination ability of the solvent and cluster solubility in the solvent. Coordinating solvents yield monodisperse products, and alcohols selectively precipitate clusters once they

grow to a certain size. This behavior is observed with three separate ligands, which suggests that these solvent effects are general among water-soluble ligands.

- O. Andrea Wong, **W. Scott Compel**, Christopher J. Ackerson. Combinatorial Discovery of Cosolvent Systems for Production of Narrow Dispersion Thiolate-Protected Gold Nanoparticles. *ACS Combinatorial Science*, *17*(1), 11–18, 2015.

2) In Chapter 3 the study of coordinating solvents is limited to the role of glyme in metallopolymer formation, which constitutes the first step of cluster synthesis. Glyme chelates the metal in the metallopolymer backbone, which prevents metallopolymer crystallization and results in a wholly amorphous entangled polymer network. Varying glyme chain length and water content dictates the extent of polymer interaction and affects the mechanical and optical properties of the material. Overall, glyme is found to play a critical role in the metallopolymer network architecture.

- **W. Scott Compel**. Metallogels Through Glyme Coordination. *Dalton Transactions*, **2016**, *45*, 4509-4512.

3) The biological circulation properties of Au clusters are discussed in Chapter 4. The absorption, distribution, metabolism, and excretion (ADME) and pharmokinetic (PK) properties of Au clusters are characterized. An atomistic model was constructed to test *in vivo* properties for six well-defined Au clusters, including ones synthesized in glyme with glutathione as the ligand. To rationalize the unexpected distribution and excretion properties we defined a set of atomistic structure-activity relationships, including hydrodynamic diameter, net charge, hydrophobic surface area, and surface charge density. Overall, small changes in particle formulation are found to provoke dramatic yet potentially predictable changes in ADME/PK, and biodistribution is shown to depend critically upon the surface structure of the particle.

- Wong, O. Andrea; Hansen, Ryan J.; Ni, Thomas W.; Heinecke, Christine L.; **Compel, W. Scott**; Gustafson, Daniel L.; Ackerson, Christopher J. Structure-activity relationships for biodistribution, pharmacokinetics, and excretion of atomically precise nanoclusters in a murine model. *Nanoscale*, *5*(21), 10525-10533, 2013.

4) In Chapter 5 the study of glymes on Au clusters is expanded to non-aqueous systems. We find that a mixture of 3:1 diglyme:THF is capable of forming a novel $Au_{20}(SR)_{15}$ cluster that lies outside of the magic number series. This cluster spontaneously assembles into a dimer bound by a single molecule of diglyme. The interaction between diglyme and the cluster is weak and renders the assemblies highly responsive to the environment. This phenomenon is expected to be generalizable across metal nanoparticles and shows that the effect of coordinating solvents is not limited to aqueous systems.

- **W. Scott Compel**, O. Andrea Wong, Xi Chen, Chongyue Yi, Roy Geiss, Hannu Häkkinen, Kenneth L. Knappenberger, Jr., Christopher J. Ackerson. Dynamic Diglyme-Mediated Self-Assembly of Gold Nanoclusters. *ACS Nano*, **2015**, *9*(12), 11690–11698.

1.3 Research Background:

Metal nanoparticles are an area of intense research due to their remarkable optical, electronic, and chemical properties. They exhibit properties markedly different from their bulk forms and are highly dependent on the size, shape, and surface chemistry of the particle.[1-5] Notably, the electronic bandgap of metal nanoparticles is directly dependent on particle size;[6] electronic structures become increasingly complex and begin to resemble discrete molecular orbital energy levels as the particles decrease in size[7] (Figure 1). Particle shape also drastically affects properties; for example, rods, prisms, and cubes will scatter light differently due to highly

localized charge polarizations at the edges and corners of the surface of the particles.[3] The fundamental understanding of how structure and composition of these particles alter optical, electronic, catalytic, and magnetic properties represents a large area of modern research.[2-4,8,9]

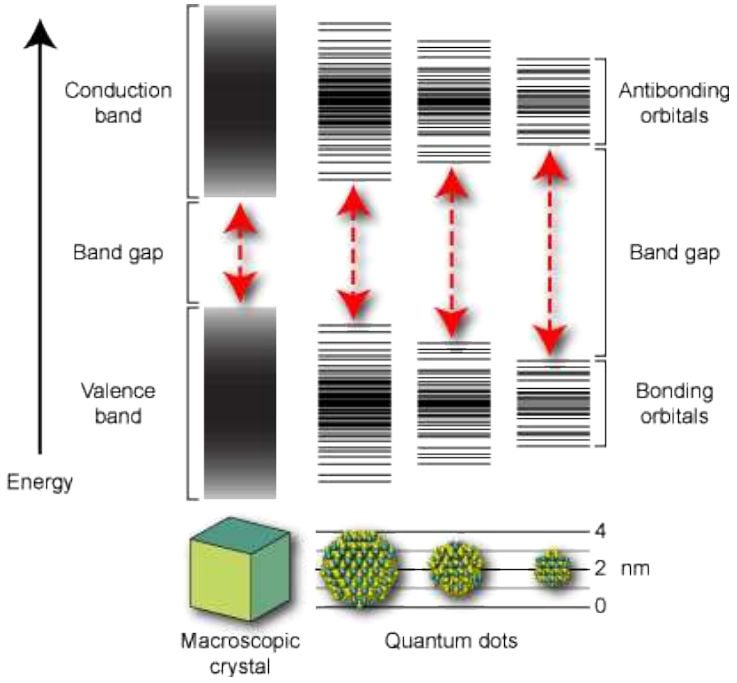

Figure 1. Disintegration of electronic band structure into discrete molecular orbital transitions with decreasing nanoparticle size.

Gold is of special interest to the metal nanoparticle community due to its remarkable chemical stability and processability.[10,11] Although Au nanoparticles have been synthesized for over 2000 years[12] their structures and properties have only relatively recently been studied. This was primarily brought about in 1951 when Turkevich reported a citrate reduction method for the formation of aqueous gold colloids that range from 10-50 nm in size.[13] This method was unique in that citrate plays two vital roles, simultaneously reducing the gold and acting as stabilizing agents. The resulting particles contain a zero-valent Au core protected by a monolayer of citrate.

Subsequent modifications to the Turkevich method led to Au nanoparticles passivated by an array of organic molecules and consequently exhibit different surface chemistries (see examples in Figure 2).

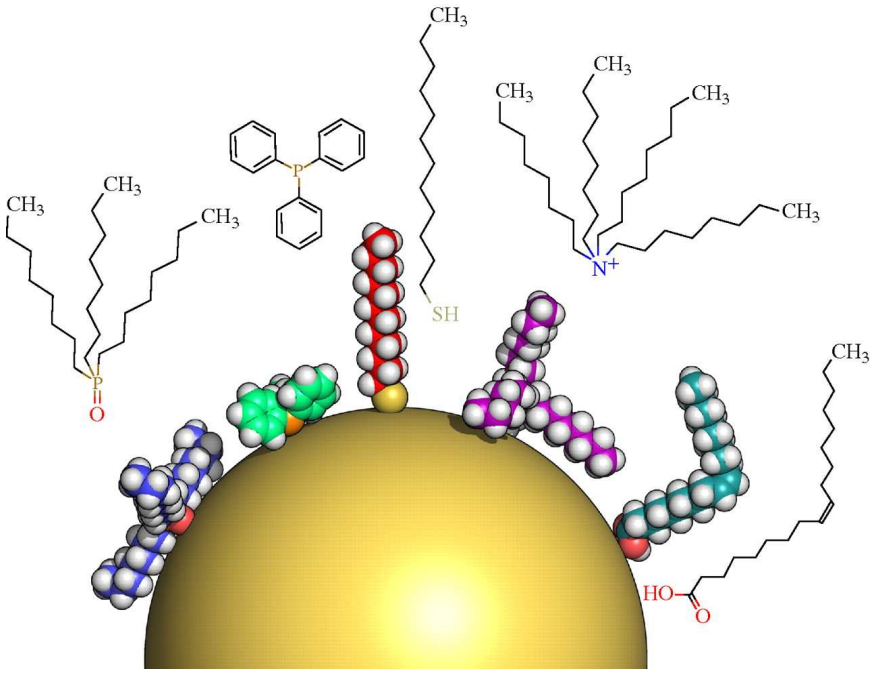

Figure 2. Examples of organic molecules commonly used to passivate a Au nanoparticle surface.

For the past half century, these colloids have found use in a very diverse range of applications, from cosmetics, drug delivery, electronics, sensing, and pollution remediation.[5,8,9,14] However, these applications require monodisperse (*i.e.*, within a few nanometers) particle sizes in large quantities.[3] Purification of products within a narrow size range from crude mixtures proved difficult, and focus quickly shifted to understanding the nature of Au nanoparticle formation and its effect on particle characteristics.[12,14] This task is inordinately complicated by the intimate linkage between thermodynamic and kinetic parameters that collectively govern nanoparticle synthesis.[3]

Varying synthetic conditions such as reactant concentration, synthetic solvent, capping agent, and reaction temperature eventually resulted in the development of monodisperse Au nanoparticles in good yield.[3,12,15] Although this led to control over nanoparticle size, shape, and dispersity,[3,12] the ordinary synthetic products were within the 10 – 100 nm range. Additionally, the Au nanoparticles are unstable to precipitation and slowly agglomerate in solution to increase in dispersity.[16] Collectively, these issues motivated research for the development of entirely new synthetic preparations for highly stable, sub-10 nm Au particles.

In 1994, Brust and Schiffrin demonstrated the landmark synthesis for sub-10 nm Au nanoparticles.[16] In this reaction, dodecanethiol is mixed with organic-phase $AuCl_4^-$, followed by BH_4^- reduction to form thiolate-protected clusters predominantly in the 1-3 nm range.[17] These products were especially interesting because electronic structures in this size regime resemble discrete molecular orbital energy levels that impart unique physiochemical properties.[7] Shortly thereafter, this synthetic approach was found to be general among organo-soluble thiolates and led to the production of a vast array of monolayer-protected clusters (MPCs) (see examples in Figure 3). Unlike their citrate-protected colloidal gold predecessors, MPCs are highly stable and robust enough to survive post-synthetic functionalization.[1] This exceptional stability, together with unique physiochemical properties, allowed MPCs to be realized in a wide variety of applications, including electronics, catalysis, biomedicine, and sensing.[6,9,10,18]

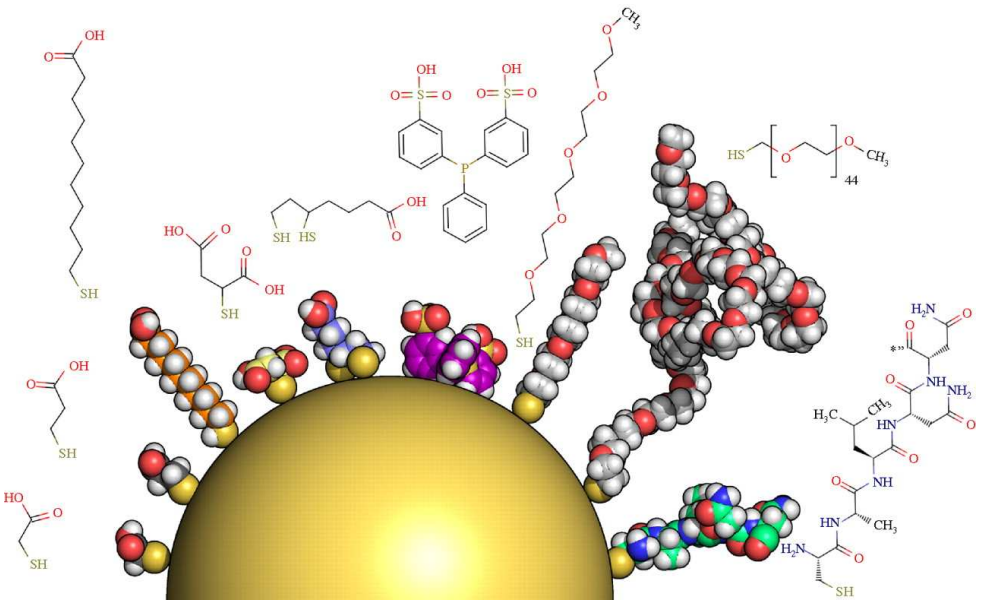

Figure 3. Examples of thiols commonly used to passivate a Au MPC surface.

Clusters in the 1-3 nm range fall in between small metal-ligand complexes and plasmonic nanoparticles, which gives rise to a special class of nanomaterials.[18] These clusters are composed of ten to a few hundred gold atoms and can be characterized as simple chemical compounds with discrete molecular formulae as opposed to average particle diameters. A salient feature of atomically defined composition is a striking correlation between metal atom count and manifested properties; addition or removal of a single metal atom profoundly affects the stability and physiochemical properties of MPCs. This phenomenon gives rise to an exceptionally diverse class of materials with seemingly endless potential evolving from minute compositional changes. However, the products of the Brust and Schiffrin synthesis are polydisperse and contain mixtures of clusters. The mixture must undergo extensive postreaction ripening or fractionalization to produce monodisperse samples before precise structure-property relationships can be understood.[1]

Interestingly, clusters of certain atomic mass were more prominent than others in the crude mixture. Seminal work from the Whetten group identified a series of exceptionally stable species of 5, 8, 14, 22, and 28 kDa masses presumed to form through geometric shell closures.[18] It wasn't until the electrophoretic isolation of a series of water-soluble thiolate-protected Au clusters by the Tsukuda group that these and other "magic sizes" were assigned molecular formulae, notably the highly stable cluster $Au_{25}(SR)_{18}$.[19,20] These "magic number" clusters (Figure 4) are now believed to possess closed electronic shells that impart exceptional stability,[21] which naturally led to an increase of studies on relatively few, highly stable Au clusters.

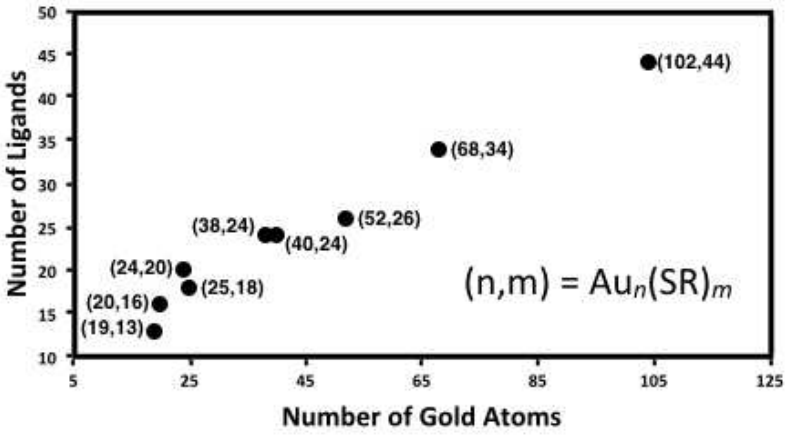

Figure 4. Magic number $Au_x(SR)_y$ clusters that demonstrate exceptional stability.

The single-crystal structure of $Au_{102}(SR)_{44}$ was of paramount importance to understanding the Au-thiol interface of Au clusters.[22] As opposed to Au nanoparticle shells that consist of a purely organic monolayer, Au MPC shells were found to be composed of Au(I)-thiol oligomers. This shell structure is an expected remnant of the Au(I)-thiol precursor that forms when $AuCl_4^-$ is mixed with thiol in the first step of the classic Brust and Schiffrin synthesis. In this case, exogenous reductant is necessary to reduce Au(I) in the oligomer to form the Au(0) cluster core, and remaining Au(I)-thiol oligomers form the passivating layer on the core surface. Thus, the

organic backbone of the thiol constitutes the surface of the Au cluster, which in turn governs behavior such as solubility and reactivity (Figure 5). The appropriate thiol must be chosen during synthesis in order to tailor desirable properties in the resulting Au cluster.

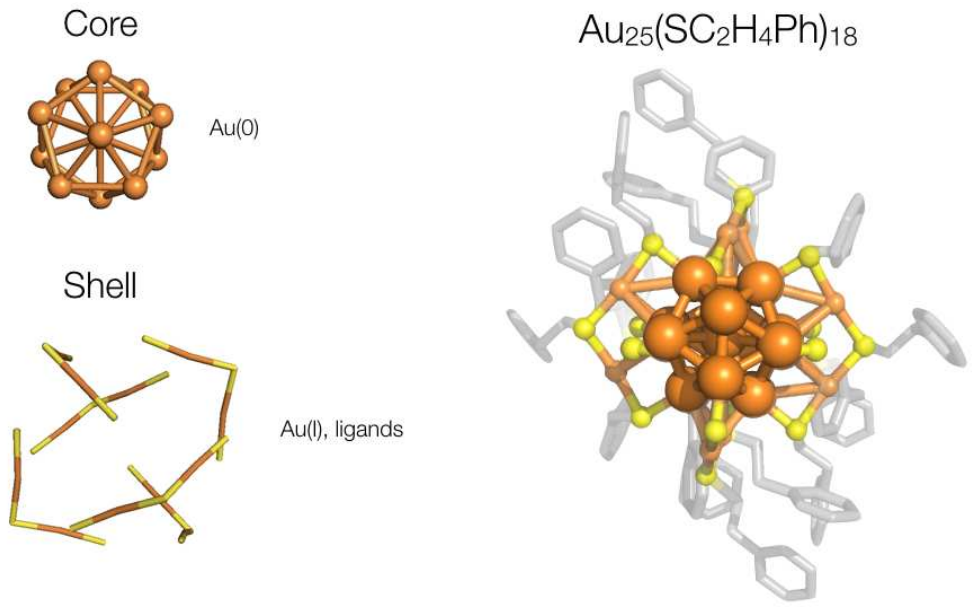

Figure 5. The structure of a $Au_{25}(SR)_{18}$ cluster (Au orange, S yellow, C grey).

The intrinsic high stability of magic number Au clusters allows post-synthetic modification for desired functionality. Techniques like thiol-for-thiol exchange were adopted from classic Au nanoparticle methodology in order to functionalize a cluster surface for fundamental studies or protein conjugation.[8,9,23] Surface modification also grants the availability to use particles as building blocks in self-assembled systems, which is prevalent in Au nanoparticles[6,24-26] but is inchoate in cluster systems. This is likely due to the differences in interparticle interactions at the nanoscale (*e.g.*, van der Waals and electrostatic) between atomically-defined Au clusters and larger colloidal systems.[26]

Ultimately, the field of Au clusters is undeveloped and major fundamental problems have yet to be addressed. Though much progress has been made in understanding the structure of Au clusters and the origin of their properties, synthetic procedures for controlling sample dispersity and modifying the cluster surface are lacking. The goal of this dissertation is to present a novel approach for monodisperse Au cluster synthesis that allows for convenient post-synthetic surface modification and assembly.

REFERENCES

1. Menard, L. D.; Gao, S.-P.; Xu, H.; Twesten, R. D.; Harper, A. S.; Song, Y.; Wang, G.; Douglas, A. D.; Yang, J. C.; Frenkel, A. I.; Nuzzo, R. G.; Murray, R. W. *J. Phys. Chem. B* **2006**, *110* (26), 12874–12883.

2. Albanese, A.; Tang, P. S.; Chan, W. C. W. *Annu. Rev. Biomed. Eng.* **2012**, *14* (1), 1–16.

3. Tao, A. R.; Habas, S.; Yang, P. *Small* **2008**, *4* (3), 310–325.

4. Noguez, C. *J. Phys. Chem. C* **2007**, *111* (10), 3806–3819.

5. Luo, X.; Morrin, A.; Killard, A. J.; Smyth, M. R. *Electroanalysis* **2006**, *18* (4), 319–326.

6. Shenhar, R.; Norsten, T. B.; Rotello, V. M. *Adv. Mater.* **2005**, *17* (6), 657–669.

7. Qian, H.; Zhu, M.; Wu, Z.; Jin, R. *Acc. Chem. Res.* **2012**, *45* (9), 1470–1479.

8. De, M.; Ghosh, P. S.; Rotello, V. M. *Adv. Mater.* **2008**, *20* (22), 4225–4241.

9. Thomas, K. G.; Kamat, P. V. *Acc. Chem. Res.* **2003**, *36* (12), 888–898.

10. Liz-Marzán, L. M. *Chem. Commun.* **2013**, *49* (1), 16–18.

11. Hakkinen, H. *Nature Publishing Group* **2012**, *4* (6), 443–455.

12. Grzelczak, M.; Pérez-Juste, J.; Mulvaney, P.; Liz-Marzán, L. M. *Chem. Soc. Rev.* **2008**, *37* (9), 1783.

13. Turkevich, J.; Stevenson, P. C.; Hillier, J. *Discuss. Faraday Soc.* **1951**, *11*, 55.

14. Zabetakis, K.; Ghann, W. E.; Kumar, S.; Daniel, M.-C. *Gold Bull* **2012**, *45* (4), 203–211.

15. Jana, N. R.; Gearheart, L.; Murphy, C. J. *J. Phys. Chem. B* **2001**, *105* (19), 4065–4067.

16. Brust, M.; Walker, M.; Bethell, D.; Schiffrin, D. J.; Whyman, R. *J. Chem. Soc., Chem. Commun.* **1994**, No. 7, 801.

17. Templeton, A. C.; Wuelfing, W. P.; Murray, R. W. *Acc. Chem. Res.* **2000**, *33* (1), 27–36.

18. Jin, R. *Nanoscale* **2015**, *7* (5), 1549–1565.

19. Negishi, Y.; Takasugi, Y.; Sato, S.; Yao, H.; Kimura, K.; Tsukuda, T. *J. Am. Chem. Soc.* **2004**, *126* (21), 6518–6519.

20. Negishi, Y.; Nobusada, K.; Tsukuda, T. *J. Am. Chem. Soc.* **2005**, *127* (14), 5261–5270.

21. Tofanelli, M. A.; Ni, T. W.; Phillips, B. D. *Inorganic …* **2016**.

22. Jadzinsky, P. D.; Calero, G.; Ackerson, C. J.; Bushnell, D. A.; Kornberg, R. D. *Science* **2007**, *318* (5849), 430–433.

23. Rosi, N. L.; Mirkin, C. A. *Chem. Rev.* **2005**, *105* (4), 1547–1562.

24. Grzelczak, M.; Vermant, J.; Furst, E. M.; Liz-Marzán, L. M. *ACS Nano* **2010**, *4* (7), 3591–3605.

25. Min, Y.; Akbulut, M.; Kristiansen, K.; Golan, Y.; Israelachvili, J. *Nat Mater* **2008**, *7* (7), 527–538.

26. Bishop, K. J. M.; Wilmer, C. E.; Soh, S.; Grzybowski, B. A. *Small* **2009**, *5* (14), 1600–1630.

CHAPTER 2

Combinatorial Discovery of Cosolvent Systems for Production of Narrow Dispersion Thiolate-Protected Gold Nanoparticles*

2.1 Synopsis

The effect of aqueous solvent concentration in the synthesis of water-soluble thiolate-protected gold nanoparticles (AuNPs) was investigated for 13 water-miscible solvents and three thiolate ligands (*p*-mercaptobenzoic acid, thiomalic acid, and glutathione). The results were analyzed by construction of heat maps that rank each reaction result for polydispersity. When solvents were organized in the heat map according to their Dimroth–Reichardt E_T parameter (an approximate measure of polarity), two 'hot spots' become apparent that are independent of the ligand used. We speculate that one hot spot may arise in part from the metal chelation or coordination ability of solvents that include diglyme, 1,2-dimethoxyethane, 1,4-dioxane, and tetrahydrofuran. The second hot spot arises at concentrations of alcohols including 2-propanol and 1-butanol that appear to selectively precipitate a growing product, presumably stopping its growth at a certain size. We observe some tightly dispersed products that appear novel. Overall, this study expands the number of tightly dispersed water-soluble AuNPs that can be directly

---

* *The work presented herein is published in ACS Combinatorial Science. W. Scott Compel's contributions to this work include experimental design, data analysis, synthetic development and characterization of the glutathione-protected gold nanoclusters used in this study.* *ACS Combinatorial Science*, *17(1)*, *11–18*, *2015*.

synthesized.

2.2 Introduction

The landmark Brust-Schiffrin synthesis[1,2] and its derivatives[3-6] preceded a now large body of literature concerning thiolate-ligated gold nanoparticles (AuNPs). This synthesis generally produces polydisperse products which can be purified,[7] etched,[7,8] annealed or 'size-focused'[9,10] to give products of atomically precise formulae.[11,12] The 5 kDa, 8 kDa, 14 kDa, 21 kDa, and 29 kDa products identified earlier[13-16] are now assigned as $Au_{25}(SR)_{18}$, $Au_{36}(SR)_{24}$, $Au_{38}(SR)_{24}$, $Au_{40}(SR)_{24}$, $Au_{67}(SR)_{35}$, $Au_{102}(SR)_{44}$, and $Au_{144}(SR)_{60}$.[17-22] The special stabilities of these clusters are explained by electronic or geometric shell filling.[23,24] The widespread adoption of these compounds by chemists,[25] biologists,[26] and physicists[27] is a testament to their robust nature.

Methods based on oxidative etching are now widespread for synthesis of the especially stable clusters.[10,28-31] These methods excel at isolating exceptionally stable clusters with nonpolar ligand shells. Also, the purification of well-defined nanoclusters from similarly sized clusters, such as the purification of $Au_{38}(SR)_{24}$ from $Au_{40}(SR)_{24}$, is increasingly well developed.[32,33] For water-soluble clusters (needed for biological applications), application of etching methods is much more limited, and is shown only for two cases so far.[34,35] Synthetic methods are also lagging for clusters that are insufficiently stable to survive the etching process.[21,36]

A less mature method for limiting the polydispersity of a cluster preparation involves selection of reaction conditions so that a single nanocluster product, rather than a product distribution, is favored. This method was developed for water soluble clusters, notably the *p*-mercaptobenzoic acid (*p*MBA) protected $Au_{144}(p\text{MBA})_{60}$ and $Au_{102}(p\text{MBA})_{44}$

clusters.[36,37] Reaction conditions that produced these syntheses were found by screening each of the synthetic parameters in the Brust synthesis, including ligand:Au ratio, solvent composition, and reductant molar excess. The direct synthesis differs from etching methods in that ligand is generally not present in excess. Compared to the now relatively mature etching approaches, this direct-synthesis approach may allow production of "less stable" clusters, presently synthetically elusive clusters,[3,5,6] and a larger panel of biologically useful water-soluble clusters than is presently available.

Previous work speculated that solvent composition is among the most important parameters in this direct synthesis of nanoparticles.[7,37] Herein we attempt to gain additional insight into which solvent compositions are associated with narrow dispersion in the Brust-type synthesis. By screening in a combinatorial manner the synthetic effects of aqueous compositions of 13 water-miscible solvents, we observe the emergence of hot spots of overall solvent polarity associated with very narrow product distribution. Overall our results suggest the existence of several so far unidentified discrete water-soluble nanoparticles.

2.3 Experimental Methods

Materials

All commercially available reagents were used without further purification. Tetrachloroauric (III) acid ($HAuCl_4 \cdot 3H_2O$ 99.99% metal basis, Alfa Aesar), *p*-mercaptobenzoic acid (>95.0%, TCI America), L-glutathione reduced (≥98%, Sigma-Aldrich), thiomalic acid (≥99.0%, Sigma-Aldrich), $NaBH_4$ (98-99%, MP Biomedicals), 1,4-dioxane (ACS grade, Mallinckrodt Chemicals), tetrahydrofuran (ACS grade, Mallinckrodt

Chemicals), dimethoxyethane (99+%, Alfa Aesar), diethylene glycol dimethyl ether (99%, Sigma-Aldrich), dimethylformamide (reagent grade, Amresco), dimethylsulfoxide (99.9% Fisher Scientific), acetonitrile (ACS grade, Fisher Scientific), 2-propanol (ACS grade, Fisher Scientific), 1-butanol (ACS grade, Fisher Scientific), 1-propanol (99.0%, Mallinckrodt Chemicals), ethanol (200 proof ACS grade, Pharmco-AAPER), methanol (99.9%, Fisher Scientific), dimethoxymethane (98%, Alfa Aesar). Nanopure water (resistivity 18.2 MΩ-cm) was produced with a Barnstead NANOpure water system.

Solvent screen with p-mercaptobenzoic acid as the ligand

Synthesis of polymer with *p*-mercaptobenzoic acid: *p*-mercaptobenzoic acid (3.4 mmol, 0.524 g, 3.4 equiv.) was dissolved in H_2O (24 mL), 10 M aq. NaOH (1.6 mL) was added to the suspension. The resulting solution was mixed and the pH was checked to be >13 and the solution was diluted with H_2O to a final volume of 50 mL. $HAuCl_4 \cdot 3H_2O$ (1 mmol, 0.394 g, 1 equiv.) was dissolved in H_2O (50 mL) in a separate beaker. The *p*MBA solution and the gold solution were mixed to yield a clear bright red solution. The bright red solution was stirred at rt overnight, which changes to yellow after about 1 h.

96-well plate solvent screen: Distribute 50 µL of the above polymer solution in each well using a multichannel pipet. Add the appropriate amount of organic solvent to each well (e.g. 25 µL for 10%, 200 µL for 80%) and backfill with the appropriate amount of H_2O (e.g. 175 µL for 10%, 0 µL for 80%) to result in a final reaction volume of 250 µL. 4 µL of freshly made 0.125 M aq. $NaBH_4$ was added to each well with a multichannel pipet. The 96-well plate was then placed in an incubating shaker at 30 ºC for 17 h. MeOH (1 mL) and 2.0 M NH_4OAc (25 µL) was added to each well and the 96-well plate was centrifuged in a

swinging bucket rotor at 4000 rpm and 4 ºC for 10 min. The clear and colorless supernatant was then removed with a multichannel pipet and the precipitate was air dried. Gel electrophoresis visualization was run on a 15% polyacrylamide gel (19:1, acrylamide : bisacrylamide) at 110 V for 1.5 h. The nanoparticle bands were visible by eye and with a UV transilluminator, thus no staining steps were performed for visualization.

Solvent screen with thiomalic acid as the ligand

Synthesis of polymer with thiomalic acid: Thiomalic acid (3.0 mmol, 0.450 g, 3.0 equiv.) was dissolved in H_2O (20 mL), 10 M aq. NaOH (2.0 mL) was added to the suspension. The resulting solution was mixed and the pH was checked to be >13 and the solution was diluted with H_2O to a final volume of 50 mL. $HAuCl_4 \cdot 3H_2O$ (1 mmol, 0.394 g, 1 equiv.) was dissolved in H_2O (50 mL) in a separate beaker. The thiomalic acid solution and the gold solution were mixed to yield a clear bright red solution. The bright red solution was stirred at rt overnight, which changes to yellow after about 1 h.

96-well plate solvent screen: Distribute 50 µL of the above polymer solution in each well using a multichannel pipet. Add the appropriate amount of organic solvent to each well (e.g. 25 µL for 10%, 200 µL for 80%) and backfill with the appropriate amount of H_2O (e.g. 175 µL for 10%, 0 µL for 80%) to result in a final reaction volume of 250 µL. 3 µL of freshly made 0.25 M aq. $NaBH_4$ was added to each well with a multichannel pipet. The 96-well plate was then placed in an incubating shaker at 30 ºC for 17 h. MeOH (1 mL) and 2.0 M NH_4OAc (25 µL) was added to each well and the 96-well plate was centrifuged in a swinging bucket rotor at 4000 rpm and 4 ºC for 10 min. The clear and colorless supernatant was then removed with a multichannel pipet and the precipitate was air dried.

Gel electrophoresis visualization was run on a 15% polyacrylamide gel (19:1, acrylamide : bisacrylamide) at 110 V for 1.5 h. The nanoparticle bands were visible by eye and with a UV transilluminator, thus no staining steps were performed for visualization.

Direct synthesis of thiomalic acid-protected red AuNP (Figure 4, right)

In a 15 mL conical was added in order 1 mL of Au-Tm polymer solution (from above, 0.01 mmol Au), 2.5 mL DME, and 1.5 mL H_2O. The reaction was allowed to cool in a 4 ^oC fridge for 10 min. 60 µL of 0.25 M $NaBH_4$ (0.015 mmol, 1.5 equiv. with respect to Au) was added and the reaction was gently mixed and left to sit at 4 ^oC (without mixing/shaking) for 3 days. MeOH was then added to the reaction to a total volume of 15 mL, 200 µL of 2.0 M NH_4OAc was also added, and the reaction was then shaken to mix and was centrifuged at 4 ^oC for 10 min. The supernatant was removed and the resulting pellet (red product) was air dried. Gel electrophoresis visualization was run on a 22% polyacrylamide gel (19:1, acrylamide : bisacrylamide) at 110 V for 1.5 h. The nanoparticle bands were visible by eye and with a UV transilluminator, thus no staining steps were performed for visualization.

Solvent screen with glutathione as the ligand

96-well plate solvent screen with L-glutathione as the ligand: Dissolve $HAuCl_4 \cdot 3H_2O$ (111.2 mg) in H_2O (2.824 mL) in a 15-mL conical to yield a 100 mM Au solution. Dissolve L-glutathione (169.4 mg) in 0.3 M aq. NaOH (5.512 mL) in a separate conical to yield a 100 mM glutathione solution (pH = 9.5). Add 10 µL of Au solution then 30 µL glutathione solution to each well of a 96-well plate. Add the appropriate amount of H_2O (e.g. 400 µL for 10% and 50 µL for 80%) then the appropriate amount of organic solvent (e.g. 50 µL for

10% and 400 µL for 80%). The resulting solution was shaken at 4 ºC for 45 min. 10 µL of freshly made 300 mM aq. $NaBH_4$ was added to each well (500 µL total reaction volume) and the plate was shaken at 4 ºC for 2 h and 15 min. MeOH (1 mL) and 2.0 M NH_4OAc (25 µL) was added to each well and the 96-well plate was centrifuged in a swinging bucket rotor at 4000 rpm and 4 ºC for 10 min. The supernatant was then removed with a glass pipet connected to an aspirator and the precipitate was dried under vacuum overnight. Gel electrophoresis visualization was run on a 22% polyacrylamide gel (19:1, acrylamide : bisacrylamide) at 110 V for 1.5 h. The nanoparticle bands were visible by eye and with a UV transilluminator, thus no staining steps were performed for visualization.

Transmission Electron Microscopy

Imaging was performed with a JEOL 1400 at an acceleration voltage of 100 kV and images were recordeed on Orius SC1000 (~4kx3k). The gold nanocluster samples were applied to carbon support film on 400 mesh copper speciment grids. The excess liquid was blotted with a piece of filter paper, and the grids were allowed to dry in air.

Size Exclusion Chromatography

Separation of cluster compounds were conducted on an ÄKTApurifier HPLC system equipped with a Superdex 75 PC 3.2/30 (2.4 mL) size exclusion column. Detection was performed at a wavelength of 254 nm. Samples were injected in Nanopure H2O and eluted at 0.02 mL/min in phosphate buffer (50 mM sodium phosphate, 150 mM NaCl, pH 7.0). Thyroglobulin, γ-globulin, ovalbumin, myoglobin, aprotinin and vitamin B-12

correesponding to Stokes-Einstein radii of 8.6, 5.1, 2.8. 1.9, 1.35 and 0.85 nm were used to generate a calibration curve for the column.

2.4 Results

Previous work suggests that two of the most important parameters for direct synthesis are ligand identity and solvent composition. We reasoned that systematic investigation of these two synthetic influences may reveal promising synthetic conditions for novel products. We tested the ligands *p*-mercaptobenzoic acid (*p*MBA), thiomalic acid (Tm), and glutathione (GSH, deprotonated: GS) in systematically varied aqueous mixtures of the solvents 1,4-dioxane (dioxane), dimethoxymethane (DMM), tetrahydrofuran (THF), dimethoxyethane (DME), diethylene glycol dimethyl ether (diglyme), *N*,*N*-dimethylformamide (DMF), dimethylsulfoxide (DMSO), acetonitrile (MeCN), 2-propanol (*i*PrOH), 1-butanol (*n*BuOH), 1-propanol (*n*PrOH), ethanol (EtOH), and methanol (MeOH).

The general approach to the combinatorial screening of reaction conditions involved attempting as many as 96 reactions, examining the effect of two synthetic variables at a time, in a matrix as large as 12x8. Each reaction was analyzed initially by polyacrylamide gel electrophoresis[7,8] (PAGE). To enable facile comparison of reaction conditions, we scored each lane of analytical PAGE gel corresponding to each tested reaction condition. The scoring system extracts three key pieces of information on a direct synthesis condition: (1) how many products were produced; (2) the apparent dispersity of the products; (3) the relative sizes of the products. An example of how we scored a small set of reactions run in varying concentrations of aqueous ethanol is shown in Figure 1. Relative dispersity is shown as a heat value and relative size and number of products are

depicted in the bottom panel. Overall, this scoring system allows compact comparison of the effects of solvent system and ligand choice in gold nanoparticle synthesis. While the PAGE gels give an excellent comparison of synthetic conditions, they may not fully account for minor products present.

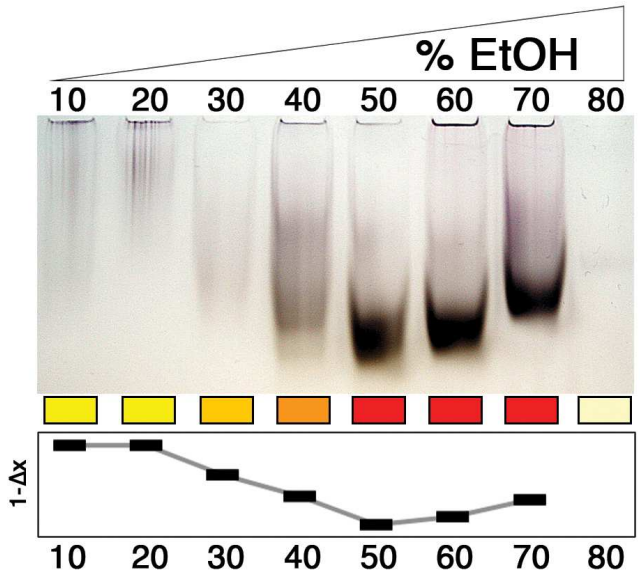

Figure 1. Example of a scored PAGE, showing heat map that encodes dispersity, and a relative size graph. The darker red in the heat map indicates a more tightly dispersed product and the relative size graph on the bottom encodes the mobility (i.e., relative size) of the products within the same gel.

Solvent effects on synthesis of p-mercaptobenzoic acid (pMBA) protected clusters

The solvent screen with *p*MBA was carried out with a 1:3.4 Au:*p*MBA ratio with initial [Au] = 2 mM and 1 equivalent of $NaBH_4$ with respect to Au. These initial screening parameters are similar to those of the published $Au_{102}(pMBA)_{44}$ synthesis which serve as a good starting point for our initial screen.[16,31] The reactions were allowed to proceed for 17 h at 30 ^{o}C in a shaking incubator. All reactions were identical except for the solvent composition. We attempted synthesis in aqueous mixtures of each of the 13 solvents, with

solvent compositions ranging from 10% to 80% solvent in water. The results of this solvent screen are shown in Figure 2.

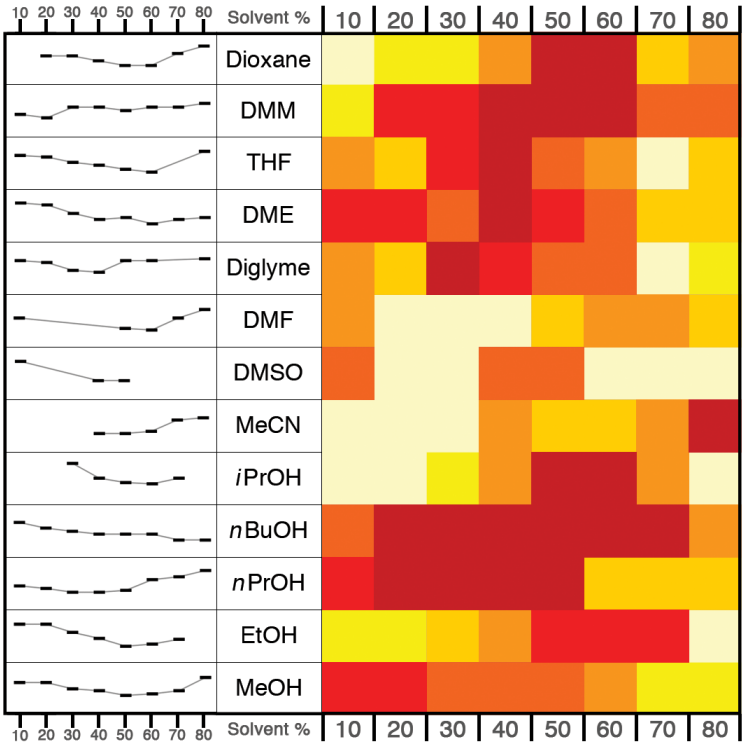

Figure 2. The solvent screen results for the synthesis of gold nanoparticles using *p*MBA as the ligand. Left panel shows the relative size of the clusters as shown by PAGE analysis. The conditions that lack a size indicator indicate no visible product formation. The right panel shows the dispersity of the products with the darkest red being the most monodispersed product. The pale yellow squares indicate no visible product formation.

Figure 2 shows the relative size of the product (with the y-axis defined as 1-Δx to resemble the bands on the original polyacrylamide gel, Δx is the distance the product travelled from the well). Some screened conditions yield either no product or non-visible product and those conditions do not have a marker on the relative size graph and these are displayed as pale yellow space in the heat map. The Δx for the polydispersed products is measured in the center of the product streak.

The right panel of Figure 2 shows the dispersity of the product, with tighter dispersion indicated by darker red, and wider dispersion indicated by lighter colors. The x-axis of Figure 2 is organized according to the percentage cosolvent in water. We constructed preliminary heat maps with the solvent identity (y-axis) arranged according to dielectric constant, dipole moment, chelating ability, and density (Figures S1 – S12) and observed that when solvents are organized according to polarity (or ionizing power, Dimroth-Reichardt E_T parameter[9,10]) of the solvents, hot spots become apparent that are independent of ligand used. We discounted the possibility that the redox potential of the solvents may play a role in product formation because the Au is in redox-stable -Au(I)-SR- complexes before it is exposed to solvents other than water, and we do not see evidence for oxidation or reduction upon solvent addition as judged by stable color of the solutions that form.

Table 1 gives a listing of E_T parameters for each solvent used. Figure 2 and other heat maps shown in this paper arrange the solvents from least-polar to most polar. The value of E_T parameter of DMM was not available. For the purpose of the heat maps, DMM was placed between dioxane and THF using the dielectric constant of the three solvents.

In Figure 2 there are two hot spots, one centered at 50% DMM and another centered at 40% *n*BuOH. Based on 1-Δx values, the products created at these hot spots are not identical. Because of similarities between the hot spots found in the *p*MBA screen and those found for other ligands, we present a unified, expanded discussion below.

Using $Au_{102}(p\text{MBA})_{44}$ and $Au_{144}(p\text{MBA})_{60}$ as standard markers in each PAGE analysis, we found eight solvent conditions that make monodispersed products, as judged by the appearance of a single, very discrete band in PAGE. Some of these solvent conditions

yield products that are in between $Au_{102}(p\text{MBA})_{44}$ and $Au_{144}(p\text{MBA})_{60}$. These conditions include (50-60 % *i*PrOH, 40% THF, 50-60% dioxane, 30% diglyme, and 40% DME). As judged by relative gel mobility, it is likely that one or more of these products is novel, and not, for instance Au_{130}.[36]

Other conditions are notable for making particles larger than $Au_{144}(SR)_{60}$, including 20-70% *n*BuOH, 80% MeCN, and 40-60% DMM. The conditions that makes that most monodispersed products are correlated to the darkest red spots in the heat map.

We further characterized the products of some of the reactions that produced narrow dispersity products by transmission electron microscopy. Figure 3 shows transmission electron micrographs for the 40% THF and 60% nBuOH conditions corresponding to products from each hotspot in figure 2. TEM reveals narrow dispersity products in each case, with the 40% THF condition corresponding to 1.84 nm ± 0.30 nm nanoparticles and the 60% nBuOH condition corresponding to 1.96 nm ± 0.29 nm. The approximate diameters correspond to molecular formulae of $Au_{228}p\text{MBA}_{75}$ and $Au_{188}p\text{MBA}_{66}$ respectively. Some of the apparent dispersity in this measurement may be attributed to the difficulty in determining the precise edge of sub 5-nm diameter particles in transmission electron micrographs—most of the measured dispersity may be inherent to the TEM technique itself as applied here. Some of the dispersity, especially larger particles, may also be attributed to electron-beam induced sintering of adjacent particles. The particles appear spherical in morphology in each case, and are of sufficiently tight dispersity to form extended 2D hexagonal lattices.

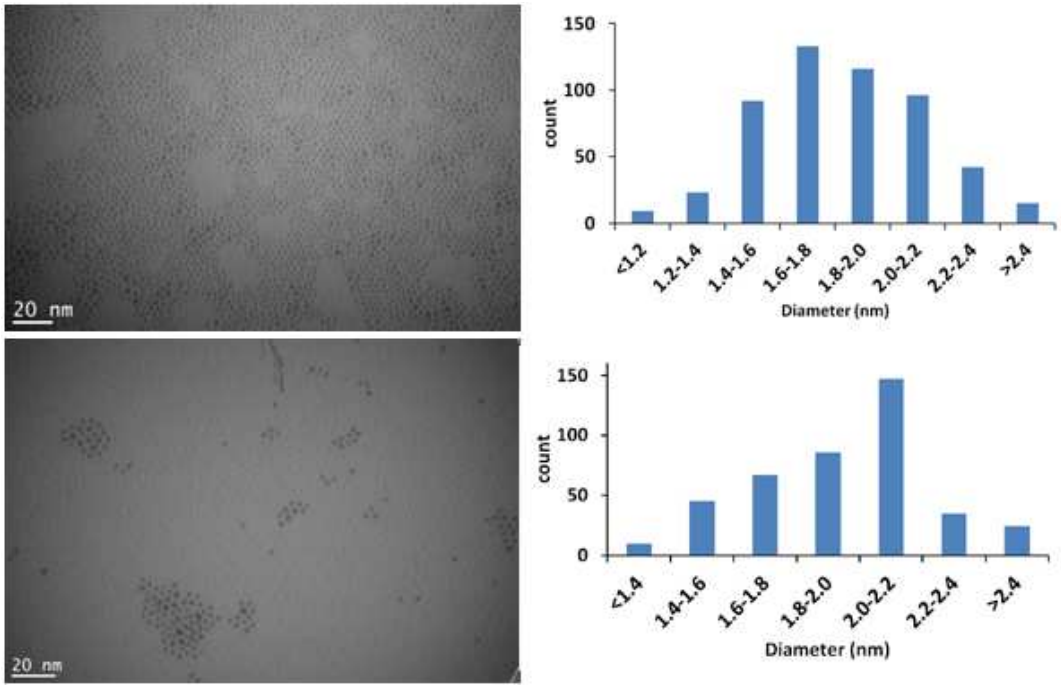

Figure 3. TEM image and histogram of the *p*MBA-protected gold nanoclusters synthesized using 40% THF (top, 1.84 nm ± 0.30 nm, Au_{188}*p*MBA_{66}) and 60% *n*BuOH (bottom, 1.96 nm ± 0.29 nm, Au_{228}*p*MBA_{75}).

After identifying the hotspots, we sought to improve the existing direct synthesis for Au_{102}(*p*$MBA)_{44}$. The existing literature synthesis uses 47% aq. MeOH, [Au] = 3 mM, [*p*MBA] = 12 mM, at a 0.036 mmol Au scale. Four solvent conditions emerged to make clusters that have the same 1-Δx values on the PAGE analysis (80% *n*BuOH, 10% DMF, 10% diglyme, and 50% MeOH). A series of refinements, including the adjustment of solvent percentages in finer increments, order of addition, method of addition, temperature, [*p*MBA], [BH_4^-], degassed solvents vs. non-degassed solvents, equilibration time of the polymer, and the addition of solid $NaBH_4$ vs. aqueous $NaBH_4$ were carried out for the synthesis of Au_{102}(*p*$MBA)_{44}$. We came to a condition that allows us to make Au_{102}*p*MBA_{44} in a 0.5 mmol Au scale in reasonable purity and yield. The reaction is 50 times larger than the original reactions scale and reproducibility may be improved. The synthetic condition

changes to the published synthesis are minor, suggesting that the published synthesis was already very well optimized. We found that the published solvent (47% aq. MeOH) made the most monodispersed $Au_{102}(p\text{MBA})_{44}$. Operational changes that improved the reproducibility and scalability include the rapid mixing of the reagents during polymer synthesis and using solid $NaBH_4$ instead of an aqueous solution. Notably, the approach does not allow elimination of the second product almost always observed in $Au_{102}(p\text{MBA})_{44}$ syntheses that is generally removed by fractional precipitation.

Solvent effects on synthesis of thiomalate (Tm) protected clusters

Similar to the initial solvent screen with *p*MBA, the solvent screen with Tm as the ligand was carried out with 1:3 Au:Tm ratio with [Au] = 2 mM and 1.5 equivalents of $NaBH_4$ with respect to Au. The reactions were allowed to proceed for 17 h at 30 ºC in a shaking incubator. The results of this solvent screen are shown in Figure 3.

Table 1. Solvent used in the Synthetic Screening as Ranked in Dimroth–Reichardt E_T parameter[35]

Solvent	Dimroth–Reichardt E_T parameter, kcal/mol
1,4-Dioxane	36.0
Dimethoxymethane (DMM)	N/A
Tetrahydrofuran (THF)	37.4
1,2-Dimethoxyethane (DME)	38.2
Diethylene glycol dimethyl ether (Diglyme)	38.6
Dimethylformamide (DMF)	43.8
Dimethylsulfoxide (DMSO)	45.1
Acetonitrile (MeCN)	45.6
2-Propanol (*i* PrOH)	49.2
1-Butanol (*n* BuOH)	50.2
1-Propanol (*n* PrOH)	50.7
Ethanol (EtOH)	51.9
Methanol (MeOH)	55.4

A hotspot appears centered at 30% THF, with additional areas of tight dispersity observed in isolated conditions of 60 and 80% *n*BuOH, and 10% and 60-70% EtOH (shown as dark red squares in the heat map). Thus, the optimal solvent for synthesis of narrowly dispersed products using Tm as the ligand can be found in the low percentages of the lower polarity solvents, except in the case of *n*BuOH which appears to be advantageous to

monodispersity at all percentages. The large hot spot at lower concentrations of solvent may share a phenomenological origin with the similar hotspot for *p*MBA, with a shift toward lower cosolvent concentrations arising because Tm is more charged (thus more polar) compared to *p*MBA.

Many of the solvents result in two distinguishable tight bands (dioxane, DME, MeCN, *n*PrOH, and EtOH), as shown in the depiction of two products in the left panel. Since the heat map considers the entire reaction, some of these conditions are scored as polydisperse, even though they may contain notably monodisperse individual products.

The smaller band in each of the two product producing reactions can be further resolved into three products, notable for their distinctive colors (red, green, and yellow; Figure 4, left). These are similar to the colors reported by Tsukuda,[37] for GSH protected clusters smaller than $Au_{25}(SG)_{18}$. The color order does not match, however, so suggestions of molecular formula cannot be made by analogy, other than these are likely to be clusters smaller than $Au_{25}(SR)_{18}$.

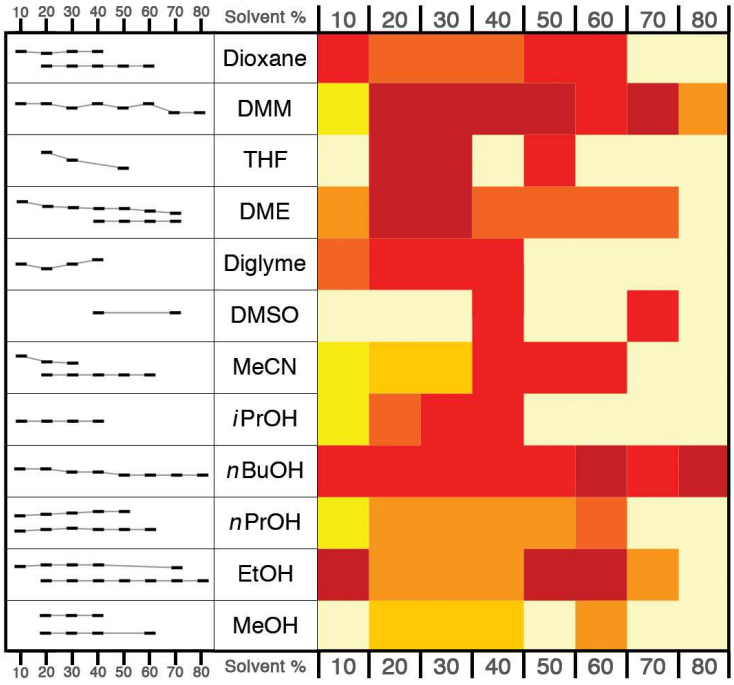

Figure 4. The solvent screen results for the synthesis of gold nanoclusters using Tm as the ligand. The left panel shows the relative size of the clusters as shown by PAGE analysis. The conditions that lack a size marker indicate no visible product formation. The conditions that have two size markers indicate the formation of two relatively tight bands. The right panel shows the dispersity of the products with the darkest red being the most monodispersed product. The pale yellow squares indicate no visible product formation.

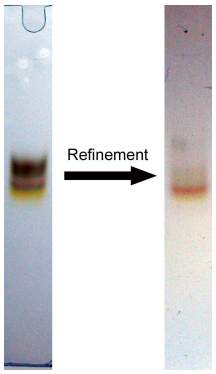

Figure 5. Refinement progress of the "triple product" band to a red band. The PAGE lane on the left is the "triple product" band before the refinement process and the PAGE lane on the right is the resulting red band after the refinement process.

To demonstrate the potential of systematic screening of reaction conditions, we further refined the synthesis that produces this set of three products, so that that only the red product is produced (Figure 4, right). The refinement process included adjustment of temperature, Au:Tm ratio, pH, reaction time, [NaOH], amount of O_2 in the solvent, and [BH_4^-] (see Experimental Section for the synthesis of the red product). The parameters that have been adjusted are commonly screened parameters in the refinement of gold nanocluster syntheses in our laboratory. The refinement process is mainly determined by the results of the previous screen until no further optimization can be obtained. Some parameters, such as [$NaBH_4$], need to be revisited after other parameters are set.

Solvent effects on synthesis of glutathione (GSH) protected clusters

The solvent screen with GSH as the ligand was carried out with 1:3 Au:GSH with [Au] = 2 mM and 3 equivalent of BH_4^- with respect to Au. The reactions were allowed to proceed for 2 h and 15 min at 4 ºC. These conditions were the result of an initial optimization. The result of this solvent screen is shown in Figure 5. As in the case for other ligands, we observe two hot spots in the heat map. One can be found in the low to mid percentages (20-40%) of low polarity solvents (DME and diglyme), the second is found in the low percentages (10-30%) of the alcohols (*i*PrOH, *n*BuOH, and *n*PrOH).

The products observed at the hot-spots when GSH is used as a ligand are less than 1.5nm in diameter and essentially of insufficient size for routine and accurate analysis by transmission electron microscopy. To characterize the approximate composition and dispersity of GSH protected nanoparticles we used size exclusion chromatography. A Superdex 75 gel filtration column (GE Health Sciences is used routinely to separate

proteins in the 3 to 70 kDa range. By comparison of actual and computed Stokes-Einstein radii, we estimate that the column is capable of resolving spherical clusters with approximate formulae of $Au_{10}(SG)_{11}$ to $Au_{998}(SG)_{161}$. We calibrated with protein standards as described in the methods section and shown in Figure S18. We tested experimentally the elution of the product synthesized at 76% aqueous diglyme, which appears to contain several products as observed in the PAGE, although one product appears more abundant (Figure S16). By chromatographic analysis we see that the 76% diglyme product also contains many products, and similar to the appearance in the gel, a single product dominates. The dominant product has a Stokes-Einstein radius of 1.11 nm (Figure 7), corresponding to an approximate molecular formula of $Au_{53}(GS)_{26}$. To arrive at this approximate molecular formula, we assume that GSH contributes 0.35 nm to the total hydrodynamic diameter of 2.44 nm, as calculated previously.[11] The remaining diameter is occupied by gold atoms. The full-width at half maximum of the main peak is slightly broader than that of the protein standards injected, consistent with a the appearance of the second most abundant product in the gel at lower molecular weight, and the tailing at what corresponds to lower molecular weight also suggests that the PAGE gel is an accurate depiction of the dispersity of the sample.

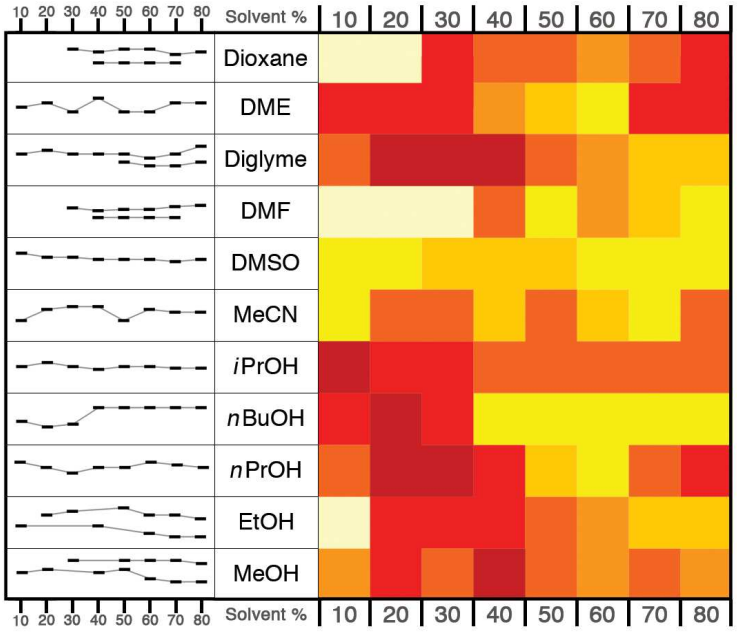

Figure 6. The solvent screen results for the synthesis of gold nanoclusters using GSH as the ligand. Left panel shows the relative size of the clusters as shown by PAGE analysis. The conditions that lack a size indicator indicate no visible product formation. The conditions that have two size markers indicate the formation of two relatively tight bands. The right panel shows the dispersity of the products with the darkest red being the most monodispersed product. The pale yellow squares indicate no visible product formation.

One goal at the outset of this screen was to attempt to find a direct, large scale synthesis of $Au_{25}(GS)_{18}$.[7,35,38] We found that one of our screened solvent conditions produced a product with the expected orange appearance, and approximately expected gel mobility. MALDI characterization of this product is not consistent with $Au_{25}(GS)_{18}$ and is instead consistent with a novel nanocluster with properties that are the subject of a future report. It is presently unclear if it is possible to directly synthesize $Au_{25}(GS)_{18}$ with this direct synthesis approach.

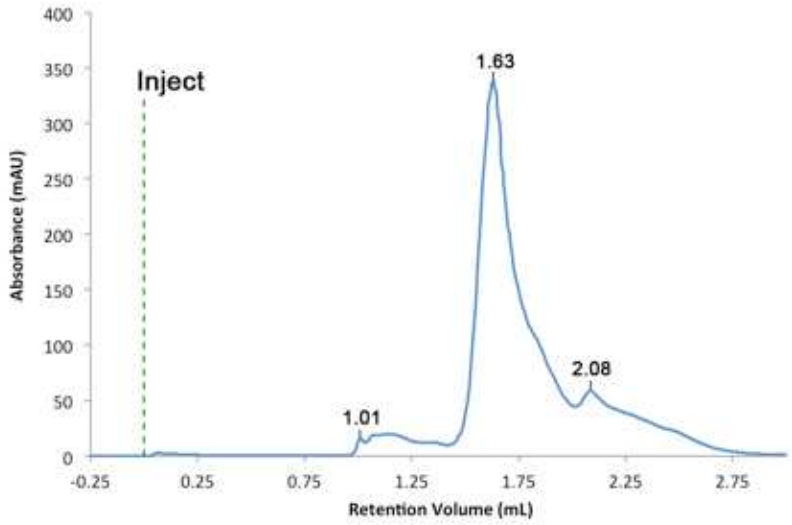

Figure 7. Superdex 75 Elution Profile for GS protected nanoparticles synthesized in 76% diglyme.

2.5 Discussion

Two hot spots of high monodispersity appear in each of the combinatorial solvent screens, independent of the organothiolate ligand that protects the resulting nanoparticles. One of the hot spots occurs in lower polarity solvents such as dioxane, DME, THF, and diglyme. These solvents are interesting in that, with the exception of THF, each is potentially both a solvent and a metal chelating ligand (Figure 6). These coordinating or chelating solvents may interact with either the $(Au\text{-}SR)_n$ polymer precursors, perhaps to enforce a particular polymer size prior to the $NaBH_4$ reduction step. This is suggested by others as a means to narrow the dispersity of cluster syntheses.[39] These solvents may also interact competitively with organothiolates to occupy the Au^0 surfaces of nanoclusters. The multidentate nature of these ligands and their extraordinarily high concentration relative to thiols may make these oxygen-containing molecules capable of such

competition. We speculate that either one of these effects may help to stabilize a particular cluster molecular formula, leading to the observed narrow dispersity.

The other hot spot appears for alcohols with longer hydrophobic chains, such as *i*PrOH, *n*BuOH, and *n*PrOH. We speculate that this hot spot arises because the nanoclusters grow until they reach a size at become insoluble in the aqueous alcohol mixture, at which point they precipitate. The precipitated nanoclusters then cease to grow. Under these circumstances, growing and completed clusters are separated in two physical phases, resulting in narrow size distribution.

This work highlights several solvents that do not correlate with monodisperse product preparation. Solvents that do not appear to produce narrow dispersion products include MeOH DMF, DMSO, and MeCN. The absence of monodisperse products in methanol is of special note. Most water soluble thiolate ligated gold nanoclusters reported to date are synthesized in aqueous methanol.[7,35-38,40-43] We observe here that methanol consistently results in more polydispersed product than its more non-polar and more bulky counterparts.

2.6 Conclusions

Early work on thiolate protected gold nanoclusters identified the approximate masses of especially abundant (magic-sized) clusters. Etching or size-focusing methods now reliably produce these clusters in many labs around the world with organic ligand shells. Synthetic methods for making water-soluble clusters and also particles that do not conform to the 'magic' sizes are not yet widely available. By combinatorial screening of solvent conditions we observe hot spots of low product dispersity, suggesting routes for

direct synthesis of well-defined water-soluble particles. We also observe in some cases the synthesis of well-defined products of sizes apparently in between the magic sizes. For instance we observe five solvent conditions that produce narrow dispersity products that are between $Au_{102}(p\text{MBA})_{44}$ and $Au_{144}(p\text{MBA})_{60}$. From the combinatorial solvent screen, there seem to be two modes of solvent effects: chelating or coordinating ability of the solvent and cluster solubility in the solvent. Full development of either one of these modes may greatly expand the availability of water-soluble clusters for applications in biology, for instance as contrast markers,[44] delivery vectors,[4] or RF heating antennae.[45]

REFERENCES

1. Brust, M.; Walker, M.; Bethell, D.; Schiffrin, D.; Whyman, R. Synthesis of thiol-derivatized gold nanoparticles in a two-phase liquid-liquid system. *J. Chem. Soc., Chem. Commun.* **1994**, 801–802.

2. Brust, M.; Fink, J.; Bethell, D.; Schiffrin, D.; Kiely, C. Synthesis and reactions of functionalized gold nanoparticles. *J. Chem. Soc., Chem. Commun.* **1995**, 1655–1656.

3. Dass, A. Mass spectrometric identification of $Au_{68}(SR)_{34}$ molecular gold nanoclusters with 34-electron shell closing. *J. Am. Chem. Soc.* **2009**, *131*, 11666–11667.

4. Bowman, M.-C.; Ballard, T.E.; Ackerson, C.J.; Feldheim, D.L.; Margolis, D.M.; Melander, C. Inhibition of HIV fusion with multivalent gold nanoparticles. *J. Am. Chem. Soc.* **2008**, *130*, 6896–6897.

5. Templeton, A.; Wuelfing, W.; Murray, R. Monolayer-Protected Cluster Molecules. *Acc. Chem. Res.* **2000**, *33*, 27–36.

6. Wyrwas, R.B.; Alvarez, M.M.; Khoury, J.T.; Price, R.C.; Schaaff, T.G.; Whetten, R.L. The colours of nanometric gold - Optical response functions of selected gold-cluster thiolates. *Eur. Phys. J. D.* **2007**, *43*, 91–95.

7. Schaaff, T.; Knight, G.; Shafigullin, M.; Borkman, R.; Whetten, R. Isolation and Selected Properties of a 10.4 kDa Gold:Glutathione Cluster Compound. *J. Phys. Chem. B* **1998**, *102*, 10643–10646.

8. Schaaff, T.; Whetten, R. Controlled Etching of Au:SR Cluster Compounds. *J. Phys. Chem. B* **1999**, *103*, 9394–9396.

9. Reichardt, C. Solvatochromic Dyes as Solvent Polarity Indicators. *Chem. Rev.* **1994**, *94*, 2319–2358.

10. Qian, H.; Zhu, Y.; Jin, R. Size-focusing synthesis, optical and electrochemical properties of monodisperse $Au_{38}(SC_2H_4Ph)_{24}$ nanoclusters. *ACS Nano* **2009**, *3*, 3795–3803.

11. Wong, O.A.; Hansen, RJ.; Ni, T.W.; Heinecke, C.L.; Compel, W.S.; Gustafson, D.L.; Ackerson, C.J. Structure-activity relationships for biodistribution, pharmacokinetics, and excretion of atomically precise nanoclusters in a murine model. *Nanoscale* **2013**, *5*, 10525–10533.

12. Jin, R. Quantum sized, thiolate-protected gold nanoclusters. *Nanoscale* **2010**, *2*, 343–362.

13. Alvarez, M.M.; Khoury, J.T.; Schaaff, T.G.; Shafigullin, M.; Vezmar, I.; Whetten, R.L. Critical sizes in the growth of Au clusters. *Chem. Phys. Lett.* **1997**, *266*, 91–98.

14. Cleveland, C.L.; Landman, U.; Schaaff, T.G.; Shafigullin, M.N.; Stephens, P.W.; Whetten, R.L. Structural evolution of smaller gold nanocrystals: The truncated decahedral motif. *Phys. Rev. Lett.* **1997**, *79*, 1873–1876.

15. Cleveland, C.L; Landman, U.; Shafigullin, M.N.; Stephens, P.W.; Whetten, R.L. Structural evolution of larger gold clusters. *Z Phys. D* **1997**, *40*, 503–508.

16. Whetten, R.L.; Khoury, J.T.; Alvarez, M.M.; Murthy, S.; Vezmar, I.; Wang, Z.L.; Stephens, P.W.; Cleaveland, C.L.; Luedtke, W.D.; Landman, U. Nanocrystal gold molecules. *Adv. Mater.* **1996**, *8*, 428–433.

17. Heaven, M. W.; Dass, A.; White, P. S.; Holt, K. M.; Murray, R. W. Crystal structure of the gold nanoparticle $[N(C_8H_{17})_4][Au_{25}(SCH_2CH_2Ph)_{18}]$ *J. Am. Chem. Soc.* **2008**, *130*, 3754–3755.

18. Zhu, M.; Aikens, C. M.; Hollander, F. J.; Schatz, G. C.; Jin, R. Correlating the crystal structure of a thiol-protected Au_{25} cluster and optical properties. *J. Am. Chem. Soc.* **2008**, *130*, 5883–5885.

19. Qian, H.; Eckenhoff, W. T.; Zhu, Y.; Pintauer, T.; Jin, R. Total structure determination of thiolate-protected Au_{38} nanoparticles. *J. Am. Chem. Soc.* **2010**, *132*, 8280–8281.

20. Nimmala, P.R.; Yoon, B.; Whetten, R.L.; Landman, U.; Dass, A. $Au_{67}(SR)_{35}$ nanomolecules: characteristic size-specific optical, electrochemical, structural properties and first-principles theoretical analysis. *J. Phys. Chem. A* **2013**, *117*, 504–517.

21. Jadzinsky, P.D.; Calero, G.; Ackerson, C.J.; Bushnell, D.A.; Kornberg, R.D. Structure of a thiol monolayer-protected gold nanoparticle at 1.1 A resolution. *Science* **2007**, *318*, 430–433.

22. Chaki, N.K.; Negishi, Y.; Tsunoyama, H.; Shichibu, Y.; Tsukuda, T. Ubiquitous 8 and 29 kDa gold:alkanethiolate cluster compounds: mass-spectrometric determination of molecular formulas and structural implications. *J. Am. Chem. Soc.* **2008**, *130*, 8608–8610.

23. Walter, M.; Häkkinen, H. A hollow tetrahedral cage of hexadecagold dianion provides a robust backbone for a tuneable sub-nanometer oxidation and reduction agent via endohedral doping. *Phys. Chem. Chem. Phys.* **2006**, *8*, 5407–5411.

24. Deheer, W. The physics of simple metal-clusters - experimental aspects and simple models. *Rev. Mod. Phys.* **1993**, *65*, 611–676.

25. Daniel, M.-C.; Astruc, D. Gold nanoparticles: assembly, supramolecular chemistry, quantum-size-related properties, and applications toward biology, catalysis, and nanotechnology. *Chem. Rev.* **2004**, *104*, 293–346.

26. Mathew-Fenn, R.S.; Das, R.; Harbury, P.A.B. Remeasuring the double helix. *Science* **2008**, *322*, 446–449.

27. Crespo, P.; Litrán, R.; Rojas, T.C.; Multigner, M.; de la Fuente, J.M.; Sánchez-López, J.C.; García, M.A.; Hernando, A.; Penadés, S.; Fernández, A. Permanent magnetism, magnetic anisotropy, and hysteresis of thiol-capped gold nanoparticles. *Phys. Rev. Lett.* **2004**, *93*, 087204.

28. Dass, A. Faradaurate Nanomolecules: A Superstable Plasmonic 76.3 kDa Cluster. *J. Am. Chem. Soc.* **2011**, *133*, 19259–19261.

29. Kumara, C.; Dass, A. $(AuAg)_{144}(SR)_{60}$ alloy nanomolecules. *Nanoscale* **2011**, *3*, 3064–3067.

30. Qian, H.; Jin, R. Controlling nanoparticles with atomic precision: the case of $Au_{144}(SCH_2CH_2Ph)_{60}$. *Nano Lett.* **2009**, *9*, 4083–4087.

31. Qian, H.; Zhu, Y.; Jin, R. Atomically precise gold nanocrystal molecules with surface plasmon resonance. *Proc. Natl. Acad. Sci. USA* **2012**, *109*, 696-700.

32. Knoppe, S.; Boudon, J.; Dolamic, I.; Dass, A.; Bürgi, T. Size Exclusion Chromatography for Semipreparative Scale Separation of $Au_{38}(SR)_{24}$ and $Au_{40}(SR)_{24}$ and Larger Clusters. *Anal. Chem.* **2011**, *83*, 5056-5061.

33. Qian, H.; Zhu, Y.; Jin, R. Isolation of ubiquitous $Au_{40}(SR)_{24}$ clusters from the 8 kDa gold clusters. *J. Am. Chem. Soc.* **2010**, *132*, 4583–4585.

34. Kumar, S.; Jin, R. Water-soluble $Au_{25}(Capt)_{18}$ nanoclusters: synthesis, thermal stability, and optical properties. *Nanoscale* **2012**, *4*, 4222–4227.

35. Wu, Z.; Chen, J.; Jin, R. One-Pot Synthesis of $Au_{25}(SG)_{18}$ 2- and 4-nm Gold Nanoparticles and Comparison of Their Size-Dependent Properties. *Adv. Funct. Mater.* **2010**, *21*, 177–183.

36. Levi-Kalisman, Y.; Jadzinsky, P.D.; Kalisman, N.; Tsunoyama, H.; Tsukuda, T.; Bushnell, D.A.; Kornberg, R.D. Synthesis and characterization of Au_{102}(*p*-MBA)$_{44}$ nanoparticles. *J. Am. Chem. Soc.* **2011**, *133*, 2976–2982.

37. Ackerson, C.J.; Jadzinsky, P.D.; Sexton, J.Z.; Bushnell, D.A.; Kornberg, R.D. Synthesis and bioconjugation of 2 and 3 nm-diameter gold nanoparticles. *Bioconjug. Chem.* **2010**, *21*, 214–218.

38. Negishi, Y.; Takasugi, Y.; Sato, S.; Yao, H.; Kimura, K.; Tsukuda, T. Magic-Numbered Aun Clusters Protected by Glutathione Monolayers (n = 18, 21, 25, 28, 32, 39): Isolation and Spectroscopic Characterization. *J. Am. Chem. Soc.* **2004**, *126*, 6518–6519.

39. Briñas, R.P.; Hu, M.; Qian, L.; Lymar, E.S.; Hainfeld, J.F. Gold nanoparticle size controlled by polymeric Au(I) thiolate precursor size. *J. Am. Chem. Soc.* **2008**, *130*, 975–982.

40. Schaaff, T.; Whetten, R. Giant gold-glutathione cluster compounds: Intense Optical Activity in Metal-Based Transitions. *J. Phys. Chem. B* **2000**, *104*, 2630–2641.

41. Negishi, Y.; Nobusada, K.; Tsukuda, T. Glutathione-protected gold clusters revisited: bridging the gap between gold(I)-thiolate complexes and thiolate-protected gold nanocrystals. *J. Am. Chem. Soc.* **2005**, *127*, 5261–5270.

42. Sousa, A.A.; Morgan, J.T.; Brown, P.H.; Adams, A.; Jayasekara, M.P.; Zhang, G.; Ackerson, C.J.; Kruhlak, M.J.; Leapman, R.D. Synthesis, Characterization, and Direct Intracellular Imaging of Ultrasmall and Uniform Glutathione-Coated Gold Nanoparticles. *Small* **2012**, *8*, 2277-2286.

43. Ackerson, C.J.; Jadzinsky, P.D.; Kornberg, R.D. Thiolate ligands for synthesis of water-soluble gold clusters. *J. Am. Chem. Soc.* **2005**, *127*, 6550–6551.

44. Hainfeld, J.F.; Slatkin, D.N.; Focella, T.M.; Smilowitz, H.M. Gold nanoparticles: a new X-ray contrast agent. *Brit. J. Radiol.* **2006**, *79*, 248–253.

45. Hamad-Schifferli, K.; Schwartz, J.J.; Santos, A.T.; Zhang, S.; Jacobson J.M. Remote electronic control of DNA hybridization through inductive coupling to an attached metal nanocrystal antenna. *Nature* **2002**, *415*, 152–5.

CHAPTER 3

Metallogels Through Glyme Coordination*

3.1 Synopsis

Glyme intercalation in copper-thiolate polymers is studied. The amorphous polymer network observed is significantly stronger than previously reported coinage metal-thiolate supramolecular hydrogels synthesized without glyme. Glyme chain length and water content strongly influence mechanical and optical behavior.

3.2 Introduction

Coinage metals (Cu, Ag, Au) react with thiols to form straight-chain polymers of 1:1 M(I):SR stoichiometry.[1-5] These complexes are precursors for functional materials including metal nanoparticles[6] and supramolecular hydrogels.[7-9] In the latter, metallophilic interactions drive self-assembly into two-dimensional (2D) sheets that stack in the third dimension to form lamellar structures.[9-11] These gels are currently studied for their potential applications in medicine,[2,9] adhesives,[4] and sensing.[8]

In this report, copper-thiolate polymers (CMTPs) form novel materials when synthesized in the presence of aqueous polyethylene glycol dimethoxy ethers (glyme, G*n*). Glyme intercalation prevents the formation of 2D sheets normally observed in metal-thiolate complexes. Paradoxically, glyme incorporation strengthens the materials. Varying

---

* *The work presented herein is published in Dalton Transactions. W. Scott Compel's contributions in this study include the entire body of work.* *© 2016 Royal Society of Chemistry. Dalton Transactions*, *2016*, *45*, *4509-4512*.

glyme chain length and water content provides explicit control over mechanical strength and visible absorption. All coinage metals are capable of forming homologous materials with a variety of thiolates containing carboxylic acid moieties (Table 1, Figure 1). For simplicity, the copper-thiomalic acid (Cu-TM) system is presented.

Table 1 Reagents capable of forming the reported metallogel

Metal Salt	Thiol	Glyme
copper(II) chloride dihydrate ($CuCl_2 \bullet 2H_2O$)	glutathione (GSH)	1,2-dimethoxyethane (G1)
silver(I) nitrate ($AgNO_3$)	thiomalic acid (TM)	diethylene glycol dimethyl ether (G2)
gold(III) chloride trihydrate ($HAuCl_4 \bullet 3H_2O$)	L-cysteine (Cys)	triethylene glycol dimethyl ether (G3)
		tetraethylene glycol dimethyl ether (G4)
		dimethyl polyethylene glycol M_n~250 (G~5)

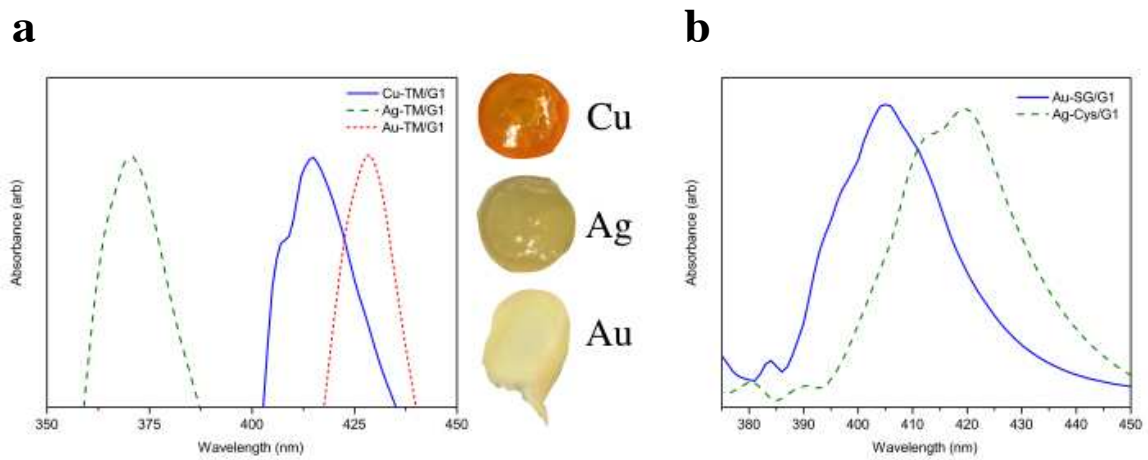

Figure 1. Linear absorption of samples prepared from reagents listed in Table S1: (a) Comparison of peak absorbance between materials made with Cu, Ag, and Au, along with pictures of each material; (b) gold-glutathione (Au-SG) and silver-cysteine (Ag-Cys) as examples of materials made with other thiols. Data presented were smoothed under Savitzky-Golay method with a 10-point window.

3.3 Experimental Methods

Materials

All chemicals were obtained from commercial suppliers and used without further purification unless otherwise noted. Copper(II) chloride dihydrate (ACS Reagent, ≥99.0%), thiomalic acid (*ReagentPlus*, ≥99.0%), diethylene glycol dimethyl ether (*ReagentPlus*, 99%), tetraethylene glycol dimethyl ether (≥99%), and poly(ethylene glycol) dimethyl ether (average M_n~250) were obtained from Sigma-Aldrich. 1,2-dimethoxy ethane (99+% stab. with BHT) and triethylene glycol dimethyl ether (99%) were obtained from Alfa Aesar. Filters used were VWR syringe filters, 0.2 μM cellulose acetate.

Cu-TM/G1 Synthesis

A 100 mM solution of thiomalic acid (1.2 mmol, 3 eq., in 12 mL 0.3 M NaOH) and 100 mM solution of $CuCl_2$•$2H_2O$ (0.4 mmol, 1 eq., in 4 mL H_2O) were filtered. The thiol solution was added to the blue copper chloride solution in a 50-mL polypropylene centrifugation tube and turned the solution black. 1,2-dimethoxyethane (G1, 12 mL) was immediately added, and the resulting cloudy white suspension shook at 4 ºC for 45 min or until a dense yellow phase was apparent. After centrifugation at 3220 g for 10 min at 4 ºC the clear, colorless supernatant was siphoned off of the viscous yellow liquid. Only the bottom portion of the liquid was used in experimentation to be sure no residual solvent was brought over into the final product.

All glymes studied (G1-G~5) are capable of substituting G1 in the above synthesis. Other metal salts and thiolates (examples found in Table S1) are replaceable with one

minor alteration to the synthetic method: 18 mL of glyme should be added when using glutathione or cysteine in place of thiomalic acid.

It is important to note that a 1:3 metal:thiol ratio is necessary to form the material regardless of the metal oxidation state (*i.e.*, 3 equivalents of $AgNO_3$ are necessary to form Ag-SR/G*n* despite Ag(I) already in the necessary +1 oxidation state).

Instrumentation

Oscillatory shear measurements were performed on a TA Instruments ARES rheometer. Dynamic frequency sweeps were performed for each sample using a 0.1% shear strain (verified linear viscoelastic region) over a frequency range of 0.05 to 1000 rad s^{-1}. Strain sweeps were performed for each sample at 1 rad s^{-1} over a range of 0.01 to 90%.

Small angle X-ray scattering (SAXS) data were collected on a Rigaku S-Max 3000 High Brilliance 3 Pinhole SAXS system outfitted with a MicroMax-007HFM Rotating Anode (CuKα), Confocal Max-FluxTM Optic, Gabriel Multiwire Area Detector and a Linkham thermal stage. The feature at q=0.25 is an artifact at the edge of the detector.

X-ray diffraction (XRD) was performed on a Scintag X-2 Advanced Diffraction system equipped with CuKα radiation (λ = 1.54 Å).

Scanning electron microscopy (SEM) was performed on a JEOL JSM-6500F microscope operating at an accelerating voltage of 15 kV.

UV-Visible spectroscopy (UV-Vis) was performed on a Nanocrop 2000c Spectrophotometer on a 1-mm path length pedestal. Data were smoothed under Savitzky-Golay method with a 10-point window to make trends more apparent (raw data available in Figure S20).

Rheometry Sample Preparation

Immediately after its synthesis, 150 μL of the viscous liquid was transferred into an 8-mm diameter rubber mold on parafilm. After drying for 24 h in ambient laboratory conditions it was transferred to a dessicator (RH = 0%) and dried for another 24 h at ambient temperature and pressure. This method allowed water to slowly diffuse out of the gel to evaporate and prevented the material from cracking. The resulting puck fits perfectly under the 8-mm top plate on the rheometer. This method provided reproducible and accurate rheological measurement of the material.

3.4 Results and Discussion

Metallopolymer was prepared by mixing $CuCl_2 \bullet 2H_2O$ with TM in a 1:3 molar ratio. Immediate addition of a large molar excess of glyme precipitates a dense yellow phase (denoted as Cu-TM/G*n*). The isolated material is a viscous liquid that consists of *ca*. 50 *wt*% water. Dynamic rheological studies corroborate a marked increase in elasticity as water evaporates (Figure 2).

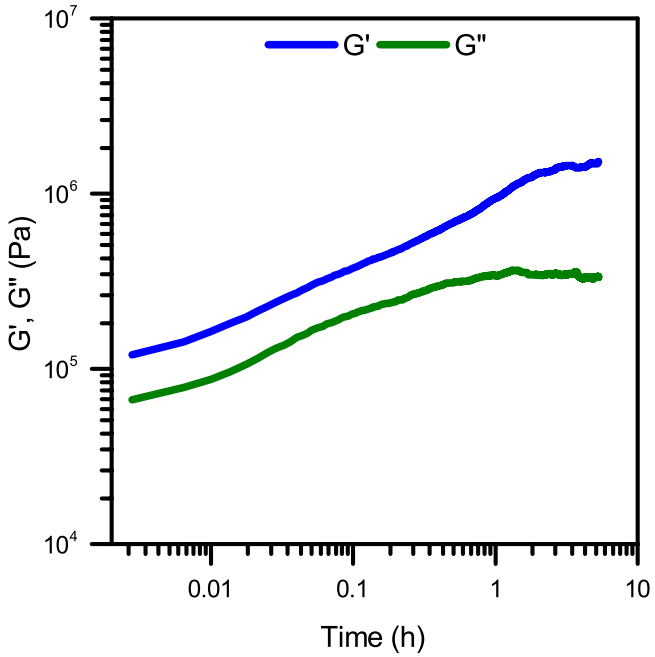

Figure 2. Time sweep rheometry of Cu-TM/G1 shows elasticity increase as the sample dries in ambient conditions.

Due to its hygroscopic nature, the material changes form as water concentration reaches equilibrium with the relative humidity (RH) of the environment. After drying to *ca*. 30 *wt*% water the material exhibits gel-like behavior by supporting its own weight and surviving the "inversion test."[12] The gels adopt a variety of solid forms contingent on how the remaining water is removed: freeze-drying forms powders, dropcasting forms thin films, and thermal treatment forms porous foams (Figure 3). Independent of its solid form, rehydrating the material to *ca*. 30 *wt*% water reforms the original gel phase (see video in Supplementary Information online).

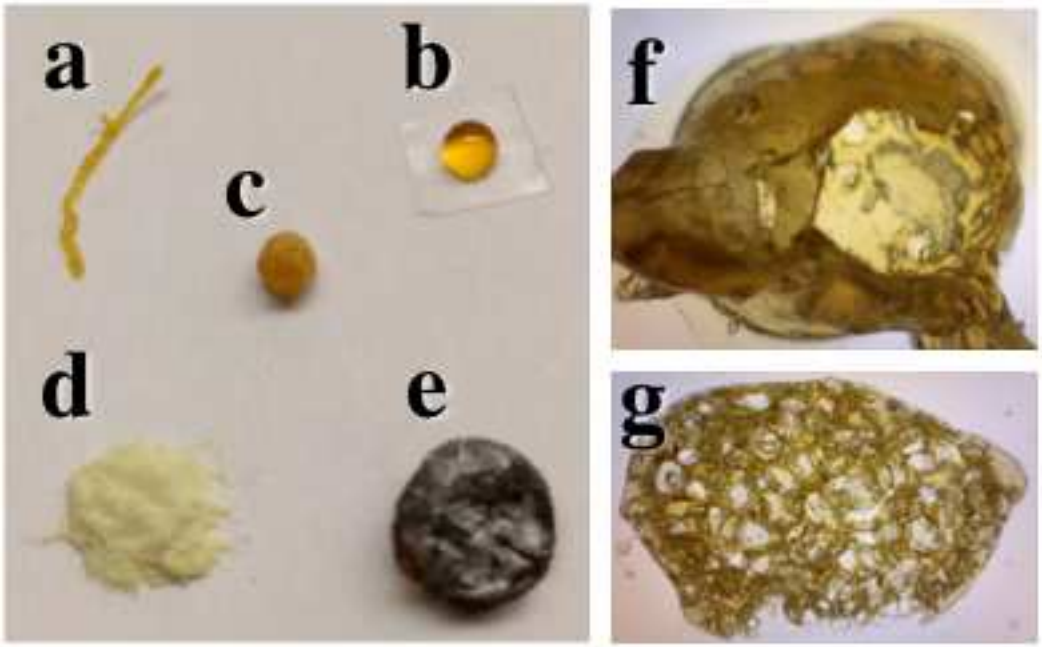

Figure 3. Pictures of Cu-TM/G1 in various solid forms: (a) wire, (b) gel, (c) hard sphere, (d) powder, (e) rigid puck, (f) hollow sphere, and (g) foam.

Time-dependent mechanical properties were probed by oscillatory strain rheometry to quantify the elastic (G') and viscous (G") moduli of the materials made with different glyme chain lengths. The gels were molded into rigid pucks by slow evaporation under 0% RH; this method is expected to preserve the hydrogen-bonded structure of water trapped in high molecular weight glyme films[13] and ensures homogeneity among samples. All samples display broadly similar behavior in each test. Rheometric properties are summarized in Table 2 and representative curves can be found in Figure 4.

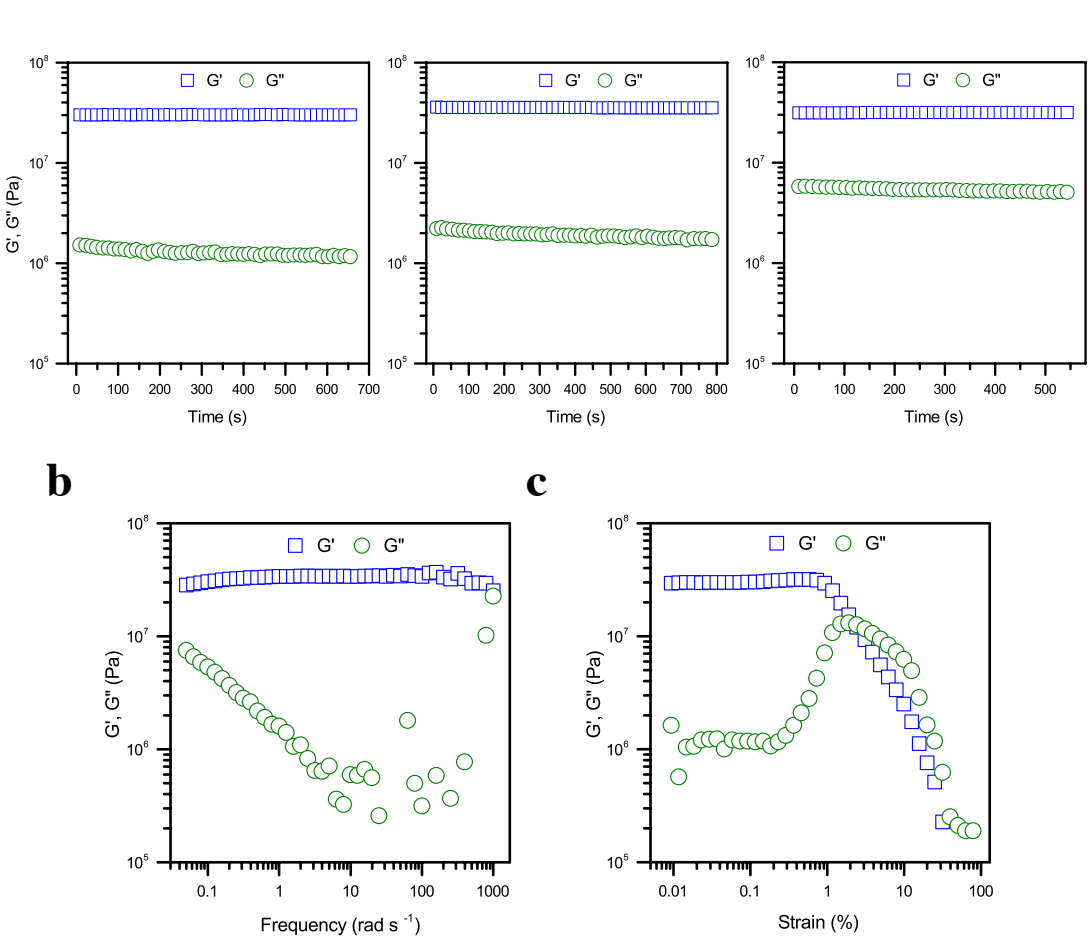

Figure 4. Representative Cu-TM/G1 curves used to obtain data in Table 1. (a) Time sweep on three separate samples prepared simultaneously. (b) Frequency sweep run at fixed strain (γ = 0.1%). (c) Strain sweep run at fixed frequency (ω = 1 Hz).

Table 2. Cu-TM/G*n* rheometric properties

Sample	G' (MPa)	G" (MPa)	tan(∂)	Yield Point (%)
Cu-TM/G1	32.5 ± 2.72	2.75 ± 2.18	0.0854 ± 0.0695	2.27
Cu-TM/G2	30.8 ± 1.82	2.72 ± 1.63	0.0864 ± 0.0492	2.78
Cu-TM/G3	30.4 ± 1.27	2.54 ± 1.62	0.0825 ± 0.0499	2.66
Cu-TM/G4	22.1 ± 0.505	0.735 ± 0.251	0.0330 ± 0.0107	2.14
Cu-TM/G~5[a]	17.3 ± 2.38	1.13 ± 0.243	0.0646 ± 0.0056	5.41

[a] G~5: $M_n \approx 250$ g mol^{-1}

G’ is approximately an order of magnitude greater than G” within the linear viscoelastic range, which validates the solid-like nature of the gel. Frequency sweep rheometry further confirms elastic behavior (G’ > G”) over all time scales probed. The material behaves as a viscoelastic solid at low strain amplitudes until the yield point (G’ = G”) at 2-5% applied stress. At this point, the molecular network is disrupted and the material starts to flow. Each sample shows an increase in G” prior to the yield point, suggesting a change in the molecular structure that results in network disintegration.[14]

Increasing glyme chain length results in a significant decrease in magnitude of G’ (Figure 5). Cu-TM/G1 affords the highest G’ at 32.5 MPa, and G’ decreases incrementally with increasing glyme chain length to 17.3 MPa with Cu-TM/G~5 (G~5: $M_n \approx 250$ g mol^{-1}). The large overall difference of 15.2 MPa indicates that longer glymes produce weaker network architectures. This relationship between glyme size and network strength suggests the existence of an ideal network that is preferential towards shorter glymes. Metallopolymer chain length cannot be precisely determined because the metallopolymer must be synthesized in the presence of glyme to precipitate the material (*vide infra*). For the purpose of this study, metallopolymer chain length is assumed to be approximately equivalent across all Cu-TM/G*n* because the ligand and solution pH are constant throughout runs.[5a]

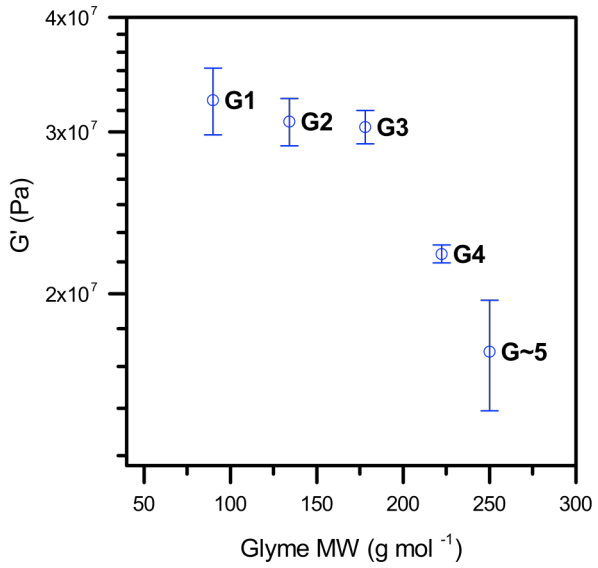

Figure 5. Comparison of Cu-TM/G*n* elastic moduli.

Network structure influences mechanical properties of materials. X-ray diffraction (XRD)[9,10] and small-angle X-ray scattering (SAXS)[11] studies on CMTPs synthesized without glyme underlie models of metallophilic interactions that enforce metallopolymer self-assembly in 2D sheets. Scanning electron microscopy (SEM) studies are consistent with XRD and SAXS and furthermore reveal porous 2D microplates.[1,2,7] The boundaries between sheets in the resulting lamellar structures represent defect sites that may shear under external force. Typical G' values are on the order of 10 Pa, though modification through crosslinking can increase G' up to thousands of Pascal while maintaining sheet structure.[4,9]

In the present system, XRD, SAXS, and SEM on glyme-containing CMTPs do not reveal sheet-like structures (Figure 6). These studies jointly suggest that glyme intercalation enforces an amorphous network. Metallophilic interactions underlie the 2D sheets previously observed,[11] suggesting glyme must be interacting with the

metallopolymer in a way that prevents this interaction and assembly. A model that accounts for this observation is one in which glyme chelates the metal in the backbone of the metallopolymer (Figure 7). This hinges on the chelation ability of glymes and is consistent with recent work on polyether coordination to metals in multinuclear complexes.[15] Distortion of the metal coordination sphere influences metallophilic interactions[16] and prevents metallopolymer assembly into sheets. G' on the order of 10^7 Pa suggests that the amorphous network is less susceptible to shear than previously reported CMTPs.

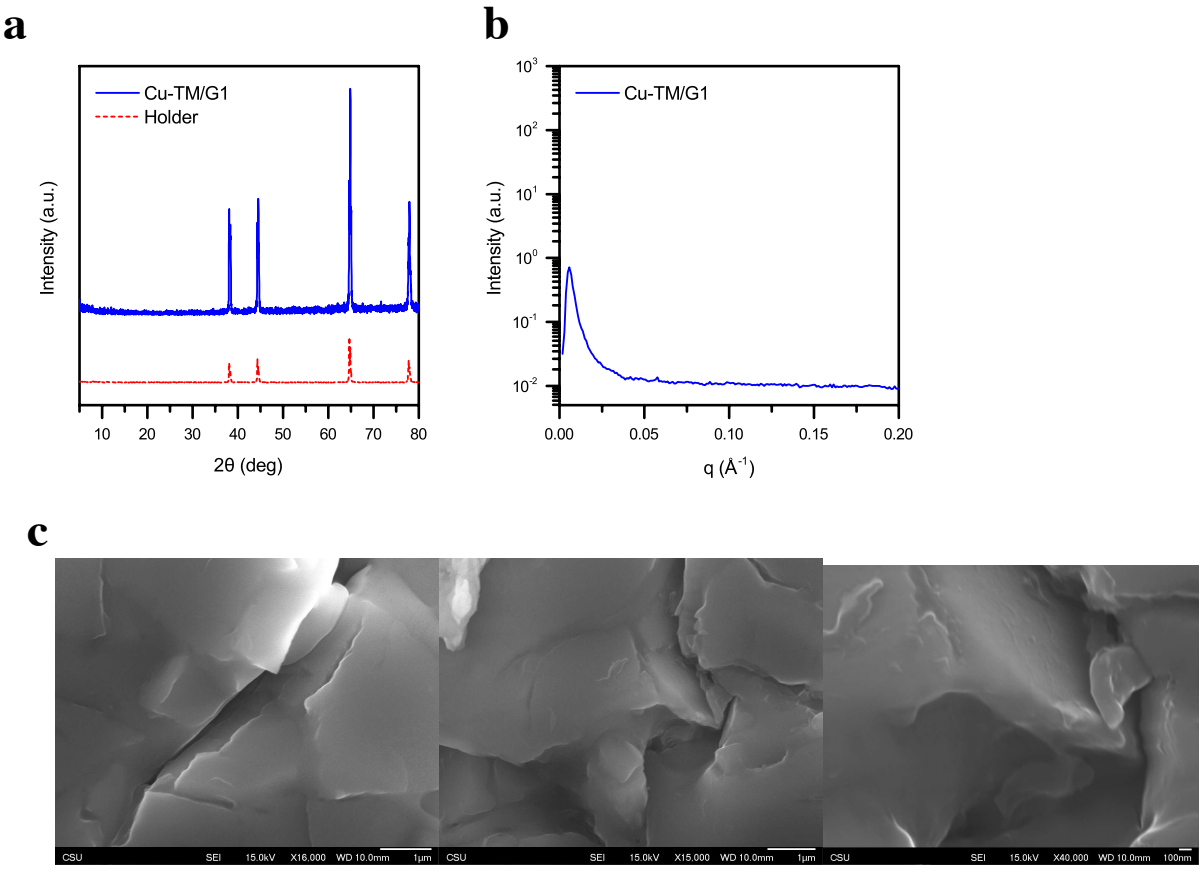

Figure 6. (a) XRD of the sample (solid blue line) only shows diffraction peaks attributed to the sample holder (dashed red line). (b) SAXS displays one feature (q = 0.25) that is an artifact at the edge of the detector; no other diffraction peaks are apparent. (c) SEM micrographs of Cu-TM/G1 display a uniform surface around cracks that formed as the sample dried. Scale bar is1 μM for the top two images and 100 nm for the bottom image.

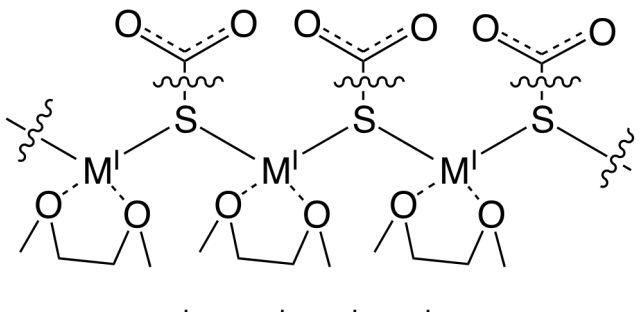

Figure 7. G1 chelates the metal in the metallopolymer backbone

The metallopolymer is insoluble in neat glyme, but synthesis in the presence of aqueous glyme allows the polymers to form an entangled network. ^{1}H-^{1}H correlation spectroscopy provides evidence that polymer chains interact through non-covalent forces (Figure 8). Water conceivably permits glyme penetration into the metallopolymer network and the large molar excess of glyme (*e.g.*, 385 equivalents of G1 to Cu) subsequently drives precipitation of the material. The resulting viscous liquid consists of roughly 50% water, and differential scanning calorimetry (DSC) indicates the presence of water as free solvent and trapped in the network (Figure 9). The degree of polymer interaction is dictated by water content: the network condenses as the material dries, resulting in increased elasticity and marked color changes.

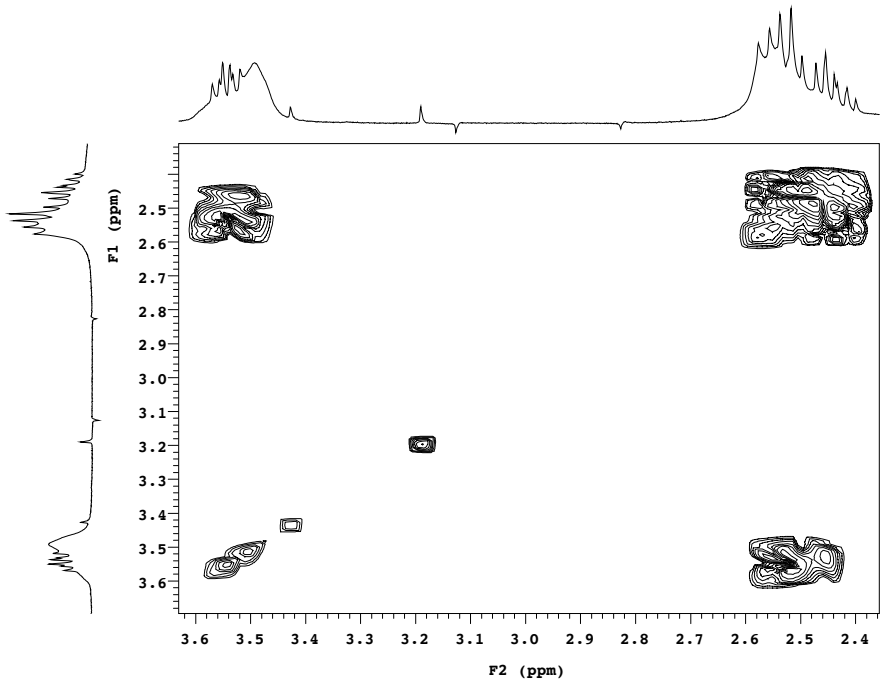

Figure 8. ^{1}H-^{1}H correlation spectroscopy of Cu-TM/G1 synthesized in D_2O. The peaks at 3.2 and 3.4 ppm correspond to G1 and all other peaks correspond to metallopolymer. The absence of off-diagonal peaks between G1 and metallopolymer suggests that G1 interacts non-covalently with the metallopolymer.

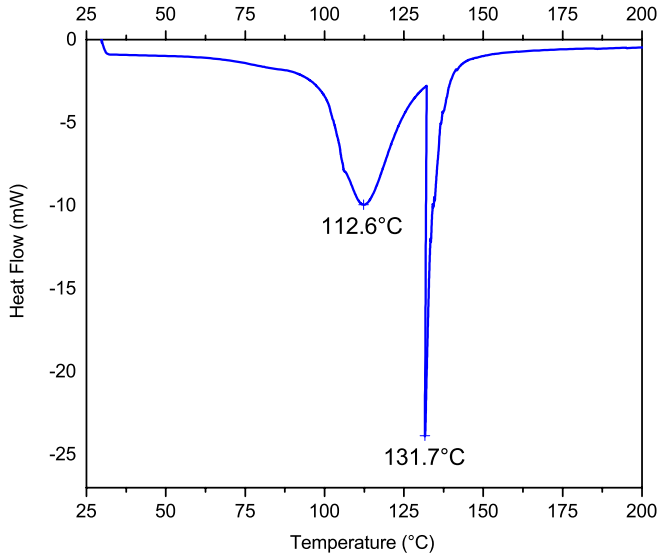

Figure 9. Differential scanning calorimetry of freshly synthesized Cu-TM/G1 differentiates between free solvent water (low temperature) and water trapped in the molecular network (high temperature). These peaks are attributed to water loss because they are irreversible and are not apparent in dessicated material. 3.7 mg of water (59 wt%) was lost during the experiment.

Fourier transform infrared spectroscopy (FTIR) studies exhibit a constant carbonyl stretch at 1548 cm^{-1} as the sample dries (Figure 10), which indicates that the carboxylate environment remains unchanged. There are two glyme ether peaks centered around 1380 cm^{-1} that shift in intensity as the sample dries. This result implies that glyme exists in two concentration-dependent forms and suggests the polymers are bound through metal-glyme coordination rather than carboxylate-glyme interactions.

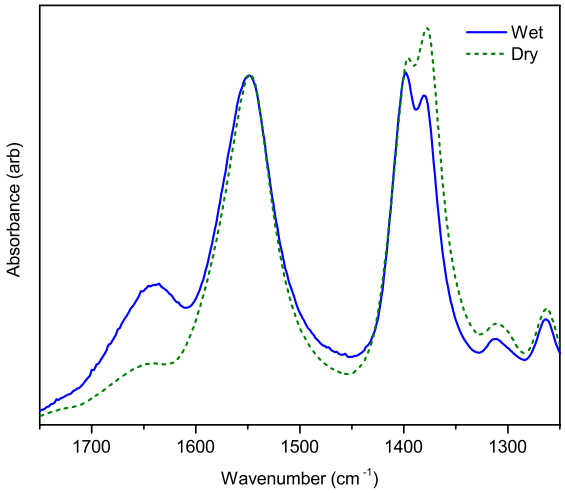

Figure 10. Infrared spectroscopy of freshly synthesized Cu-TM/G1 (solid blue line) and after drying for 12 h (dashed green line). The peak at 1548 cm^{-1} (carbonyl stretch) does not shift in energy while the sample dries and implies that the carboxylate environment remains unchanged. The peaks at ~1380 cm^{-1} (glyme ether stretch) display a shift in relative intensity, which indicate the local environment of glyme ether changes while the sample dries.

The concentration-dependence on network structure is observable through changes in visible absorbance, which is strongly influenced by metallophilic interactions[3,17] and the nature of the metal coordination sphere.[18] UV-Visible spectroscopy (UV-Vis) shows a single absorption (λ_{max} = 414 nm) for Cu-TM/G1 as-synthesized, and periodic monitoring of the drying sample reveals a bathochromic shift (smoothed data in Figure 11a, raw data in Supplemental Information Figure S20a). This is a characteristic of a change in the metal coordination environment as water evaporates. The result suggests the metal is initially ligated by water, and glyme coordination follows as water is lost and the network condenses.

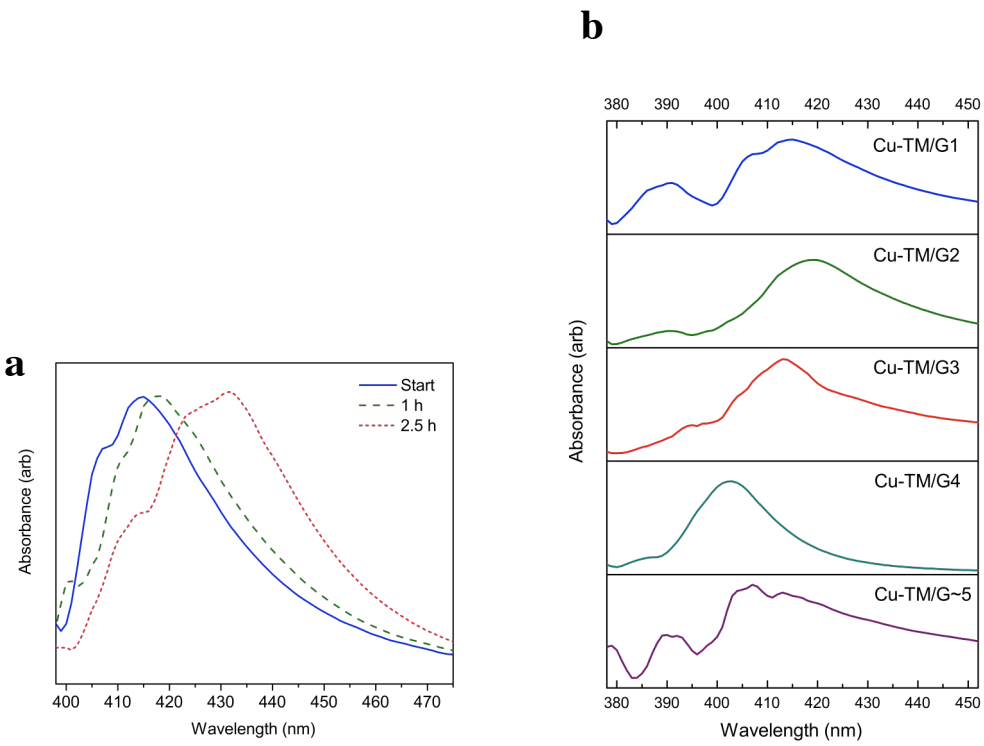

Figure 11. Smoothed linear absorption (a) of Cu-TM/G1 while drying and (b) comparison between Cu-TM/G*n*.

Interestingly, varying glyme chain length in Cu-TM/G*n* results in minimal change in λ_{max} over the range of 403-418 nm (smoothed data in Figure 11b, raw data in Supplemental Information Figure S20b). Such a minor change in linear absorption suggests that all glymes have similar coordination to the metal. This appears counter-intuitive, since binding affinity generally increases with glyme length and number of binding sites.[19] However, it is likely that the metal reaches coordinative saturation, where steric constraints prevent coordination from all available oxygens.[20] The limited solvent accessibility of the metal generates similar coordination environments for all glymes independent of chain length.

Rheological studies support coordinative saturation and propose that G1 produces the strongest network. Longer glymes introduce non-coordinating oxygens that extend past the primary coordination sphere of the metal. This effectively produces polyethylene side chains that branch out into the molecular network and add rotational degrees of freedom that bestow increased flexibility. The tail ends of glyme could also coordinate two metal centers to create physical crosslinks between metallopolymers. The relatively small differences in G' between materials made with G1-G3 suggest that these chains are too short to noticeably contribute to this effect. The critical chain length appears to be G4, as there is a substantial decrease in G' upon G4 intercalation that continues with G~5. This complements the benchtop observation that longer glymes form more fragile gels. It is not known whether this trend continues to longer glymes that could coordinate to three or more metal centers, as this may strengthen the molecular network.

3.5 Conclusions

Copper-thiolate polymers form an entangled polymer network when synthesized in the presence of glymes. The data presented support a hypothesis in which glyme chelates the metal in the metallopolymer backbone. This interaction prevents metallopolymer crystallization and results in a wholly amorphous material that is stronger than previously reported coinage metal-thiolate supramolecular hydrogels synthesized without glyme. Varying glyme chain length and water content dictates the extent of polymer interaction and affects the mechanical and optical properties of the material. Though this report establishes a novel approach toward metallopolymer gelation using Cu-TM/G*n* systems, an

extension to other coordination metal polymers is currently under investigation. Further study of this system is anticipated to provide stimuli-responsive, self-healing materials.

REFERENCES

1. I. Odriozola, I. Loinaz, J. A. Pomposo and H. J. Grande, *J. Mater. Chem.*, 2007, **17**, 4843; I. Odriozola, N. Ormategui, I. Loinaz, J. A. Pomposo and H. J. Grande, *Macromol. Symp.*, 2008, **266**, 96–100.

2. P. Casuso, P. Carrasco, I. Loinaz, H. J. Grande and I. Odriozola, *Org. Biomol. Chem.*, 2010, **8**, 5455.

3. C. Lavenn, L. Okhrimenko, N. Guillou, M. Monge, G. Ledoux, C. Dujardin, R. Chiriac, A. Fateeva and A. Demessence, *J. Mater. Chem. C*, 2015, **3**, 4115–4125.

4. A. Ruiz de Luzuriaga, A. Rekondo, R. Martin, G. Cabañero, H. J. Grande and I. Odriozola, *J. Polym. Sci. Part A: Polym. Chem.*, 2015, **53**, 1061–1066.

5. R. P. Briñas, M. Hu, L. Qian, E. S. Lymar and J. F. Hainfeld, *J. Am. Chem. Soc.*, 2008, **130**, 975–982; R. Bau, *J. Am. Chem. Soc.*, 1998, 9380–9381.

6. R. Jin, *Nanoscale*, 2015, **7**, 1549–1565; L. G. AbdulHalim, S. Ashraf, K. Katsiev, A. R. Kirmani, N. Kothalawala, D. H. Anjum, S. Abbas, A. Amassian, F. Stellacci, A. Dass, I. Hussain and O. M. Bakr, *J. Mater. Chem. A*, 2013, **1**, 10148; D. Mott, J. Yin, M. Engelhard, R. Loukrakpam, P. Chang, G. Miller, I.-T. Bae, N. Chandra Das, C. Wang, J. Luo and C.-J. Zhong, *Chem. Mater.*, 2010, **22**, 261–271.

7. I. Odriozola, P. Casuso, I. Loinaz, G. Cabañero and H. J. Grande, *Org. Biomol. Chem.*, 2011, **9**, 5059.

8. J.-S. Shen, D.-H. Li, Q.-G. Cai and Y.-B. Jiang, *J. Mater. Chem.*, 2009, **19**, 6219.

9. Y. Liu, W. Ma, W. Liu, C. Li, Y. Liu, X. Jiang and Z. Tang, *J. Mater. Chem.*, 2011, **21**, 19214.

10. F. Bensebaa, T. H. Ellis, E. Kruus, R. Voicu and Y. Zhou, *Langmuir*, 1998, **14**, 6579–6587; F. Bensebaa, T. H. Ellis and E. Kruus, *Canadian Journal of Chemistry*, 1998, 1654–1659; A. N. Parikh, S. D. Gillmor, J. D. Beers, K. M. Beardmore, R. W. Cutts and B. I. Swanson, *J. Phys. Chem. B*, 1999, **103**, 2850–2861.

11. B. Söptei, J. Mihály, I. C. Szigyártó, A. Wacha, C. Németh, I. Bertóti, Z. May, P. Baranyai, I. E. Sajó and A. Bóta, *Colloids and Surfaces A: Physicochemical and Engineering Aspects*, 2015, **470**, 8–14.

12. D. K. Kumar and J. W. Steed, *Chem. Soc. Rev.*, 2014, **43**, 2080–2088.

13. M. Gemmei-Ide, T. Motonaga and H. Kitano, *Langmuir*, 2006, **22**, 2422–2425.

14. P. Byrne, G. O. Lloyd, L. Applegarth, K. M. Anderson, N. Clarke and J. W. Steed, *New J. Chem.*, 2010, **34**, 2261.

15. S. Mishra, G. Ledoux, E. Jeanneau, S. Daniele and M.-F. Joubert, *Dalton Trans.*, 2012, **41**, 1490–1502; I. Chevrier, J. L. Sagué, P. S. Brunetto, N. Khanna, Z. Rajacic and K. M. Fromm, *Dalton Trans.*, 2013, **42**, 217–231.

16. I. G. Dance, L. J. Fitzpatrick, A. D. Rae and M. L. Scudder, *Inorg. Chem.*, 1983, 3785; J.-P. Zhang, Y.-B. Wang, X.-C. Huang, Y.-Y. Lin and X.-M. Chen, *Chem. Eur. J.*, 2005, **11**, 552–561.

17. A. Y.-Y. Tam and V. W.-W. Yam, *Chem. Soc. Rev.*, 2013, **42**, 1540; A. J. McConnell, C. S. Wood, P. P. Neelakandan and J. R. Nitschke, *Chem. Rev.*, 2015, **115**, 7729–7793.

18. S.-I. Kawano, N. Fujita and S. Shinkai, *J. Am. Chem. Soc.*, 2004, **126**, 8592–8593.

19. P. Johansson, J. Tegenfeldt and J. Lindgren, *Polymer*, 1999, **40**, 4399–4406; S. Terada, T. Mandai, R. Nozawa, K. Yoshida, K. Ueno, S. Tsuzuki, K. Dokko and M. Watanabe, *Phys. Chem. Chem. Phys.*, 2014, **16**, 11737; S. Tang and H. Zhao, *RSC Adv.*, 2014, **4**, 11251.

20. P. R. Markies, O. S. Akkerman and F. Bickelhaupt, *Organometallics*, 1994, **13**, 2616–2627; T. Mandai, H. Masu and P. Johansson, *Dalton Trans.*, 2015, **44**, 11259–11263.

CHAPTER 4

Structure-Activity Relationships for Biodistribution, Pharmacokinetics, and Excretion of Atomically Precise Nanoclusters in a Murine Model

4.1 Synopsis

The absorption, distribution, metabolism and excretion (ADME) and pharmacokinetic (PK) properties of inorganic nanoparticles with hydrodynamic diameters between 2 and 20 nm are presently unpredictable. It is unclear whether unpredictable *in vivo* properties and effects arise from a subset of molecules in a nanomaterials preparation, or if the ADME/PK properties are ensemble properties of an entire preparation. Here we characterize the ADME/PK properties of atomically precise preparations of ligand protected gold nanoclusters in a murine model system. We constructed atomistic models and tested *in vivo* properties for six well defined compounds, based on crystallographically resolved $Au_{25}(SR)_{18}$ and $Au_{102}(SR)_{44}$ nanoclusters with different (SR) ligand shells. To rationalize unexpected distribution and excretion properties observed for several clusters in this study and others, we defined a set of atomistic structure-activity relationships (SAR) for nanoparticles, which includes previously investigated parameters such as particle hydrodynamic diameter and net charge, and new parameters such as hydrophobic surface area and surface charge density. Overall we find that small changes in particle formulation

---

[*] *The work presented herein is published in Nanoscale. W. Scott Compel's contributions include the synthetic development and characterization of gold nanoclusters used in this study.* *Nanoscale*, *5(21)*, *10525-10533*, *2013*.

can provoke dramatic yet potentially predictable changes in ADME/PK.

4.2 Introduction

Ligand passivated metal and semiconductor nanoparticles can encode several physical properties of clinical interest for diagnostic imaging and therapy. Investigated diagnostic imaging properties include X-ray contrast,[1-3] luminescence,[4-6] and PET/SPECT.[7] Preclinical therapeutics based on these nanomaterials can be analogous to antibody mimetics,[8] or be targeted hyperthermal therapeutics,[9,10,11] where the inorganic core of the nanomaterial interacts with extrinsic radiation (typically IR or RF) to produce localized therapeutic heat.

Predictive and complete understanding of biological absorption, distribution, metabolism, excretion (ADME) and pharmacokinetics (PK) of metal and semiconductor nanoparticles is important for realizing a comprehensive set of design criteria for determining which nanomaterials may ultimately be useful in clinic. Ideally a set of structure-activity relationships (SAR) will emerge, enabling design, synthesis and application of nanoparticles with accurately predicted circulation lifetimes, metabolism and clearance mechanisms, tissue penetrations, cellular and subcellular trafficking, and high localization efficiency to desired corporeal targets.

Current predictive understanding of the ADME/PK of inorganic nanoparticles is incomplete, in part because these experiments combine complex mixtures of nanoparticles (i.e., a 10.0 ± 1.0 nm gold colloid preparation contains on the order of 40,000 discrete molecular formulae) with blood which is also a complex mixture itself. The uncertainties inherent in nanoparticle preparation complicate the analysis of their biological activity.

Some very general conclusions about ADME/PK can be drawn. For instance, nanoparticles substantially larger than 20 nm in hydrodynamic diameter (i.e., the size of the smallest viruses) are relatively predictable in their PK and biodistribution.[12-14] Such particles are generally cleared by the reticuloendothelial system (RES), with some control in circulation time imparted by the surface layer, where poly- and oligo- ethylene glycols are shown to dramatically increase blood circulation half life.[15,16] The metabolism and excretion of inorganic particles in the RES is unpredictable.[4,5] Some reports begin to establish metabolism and excretion with mechanism,[17,18] while other reports conclude in long-term RES accumulation with unknown consequence,[13] and RES toxicity[13,19] all present and all arising from particle preparations of different nature.

The 2-20 nm hydrodynamic diameter range (smaller than viruses and other pathogens for which mammals have well established mechanisms for blood clearance) is a less predictable size regime, and one in which ADME/PK properties may be tunable for desired clinical applications. Predictive circulation lifetime is important as diagnostic imaging applications generally specify short circulation lifetimes while therapeutic applications generally benefit from extended circulation times.[20]

Within this size regime, three hydrodynamic diameter thresholds are important determinants of ADME/PK. These are the ~8 nm hydrodynamic threshold of glomular wall filtration in the kidney, the 5 nm threshold for rapid extravascular equilibration, and the ~20 nm threshold for Enhanced Permeability and Retention (EPR).[16,21] The glomural wall of the kidney has a nominal pore size of 8 nm and as a negatively charged structure is more selective for filtration of positively charged particles. Zwitterionic particles may need to be as small as 5.5 nm to pass efficiently,[4] and negatively charged particles can have

unpredictable behavior including apparently extended circulation times[18] and kidney accumulation,[1] sometimes with notable associated toxicity.[22] Still renal clearance of nanoparticles is often viewed as a favorable result,[4,5] since it results in predictable clearance of nanoparticles relative to RES clearance. Toxicity in this size range also appears unpredictable, with 1.4 nm and 13 nm particles observed as causing acute toxicity,[19,23,24] while other sizes appear essentially non-toxic in short term studies.

The study of ADME/PK of nanomaterials is complicated by the complex natures of both nanomaterial preparations and biological systems. While obvious that blood is a complicated mixture, less frequently highlighted is that most nanomaterials preparations are also complex mixtures. For instance, implicit in even 'monodisperse' preparations of nanomaterials is a 10% standard deviation in dimension measurement, suggesting that a 'monodisperse' 10±1 nm spherical gold nanoparticle preparation corresponds to a statistical gold composition of 244,000 ± 70,000 atoms. The *purity* of the exactly 10 nm diameter $Au_{244,000}$ core is less than 1% in this preparation. Further complicating these mixtures is frequently an additional distribution in ligand shell composition, especially for mixed ligand shells.

In the present study, we make the first examination of the ADME/PK properties of 'magic number' gold clusters,[25,26] specifically those scaffolded by the crystallographically determined $Au_{25}(SR)_{18}$ and $Au_{102}(SR)_{44}$ nanoclusters. We prepared each compound with three different ligand shells: an as-synthesized ligand shell (*p*-mercaptobenzoic acid and glutathione for Au_{102} and Au_{25}, respectively) and two partially ligand exchanged shells with tetraethylene glycol functionality introduced in varying amounts. We modeled each of the six compounds as idealized atomistic models, and suggest that the structural features of

these models give novel insight into the surprising ADME/PK activity observed for some of these preparations.

4.3 Experimental Methods

Generation of Models

Models of the ligands on $Au_{25}(GSH)_{18}$ (**1**), $Au_{25}(GSH)_9[S(CH_2)_6(EG)_4OH]_9$ (**2**), $Au_{25}(GSH)_6[S(CH_2)_6(EG)_4OH]_{12}$ (**3**), $Au_{102}(p\text{MBA})_{44}$ (**4**), $Au_{102}(p\text{MBA})_{22}[S(CH_2)_{11}(EG)_4OH]_{22}$ (**5**), $Au_{102}(p\text{MBA})_{14}[S(CH_2)_{11}(EG)_4OH]_{30}$ (**6**) were generated with PRODRG[27] and manually modeled onto clusters in PyMOL.[28]

Calculation of Hydrodynamic Radius

Models were inputted into Hydropro10[29] with 0.0035 Pa·s to simulate the viscosity of serum at 37 °C.[30] Settings were left as recommended by Ortega *et al*.[29], except molecular weight and partial specific volume. Partial specific volume was calculated according to Durchschlag *et al*.[31] for each of the ligands then multiplied by the number of ligands and added to the partial specific volume of the gold cluster divided by the molecular weight to obtain ν_c.

Calculation of Solvent Accessible Area

Solvent accessible area was calculated using PyMOL's ability to calculate area. Hydrophilic atoms were set as nitrogen and oxygen and hydrophobic areas were set as carbon and sulfur. Solvent radius was set at 1.4 Å and modeled and the total area around each of the areas was calculated.

Calculation of Surface Charge

Models of ligands were input into PDB2PQR[32,33] to convert models from PDB format to PQR, which was then input into Adaptive Poisson-Boltmann Solver (APBS)[34] to calculate total surface charge. The force field chosen for the calculations was SWANSON, the model was also allowed to optimize the hydrogen bonding network.

Reagents

All commercially available reagents were used without further purification. Tetrachloroauric (III) acid ($HAuCl_4 \cdot 3H_2O$ 99.99% metal basis, Alfa Aesar), *p*-mercaptobenzoic acid (>95.0%, TCI America), $NaBH_4$ (98-99%, MP Biomedicals), MeOH (99.9%, Fisher Scientific), L-glutathione reduced (≥98%, Sigma-Aldrich), Diethylene glycol dimethyl ether (99%, Sigma-Aldrich), 2-[2-(1-mercaptoundec-6-yloxy)-ethoxy]-ethoxy-ethoxy-ethanol (HS-$(CH_2)_6$-EG_4-OH, Prochimia Surfaces), ([11-(Methylcarbonylthio)undecyl]tetra(ethylene glycol) (AcS-$(CH_2)_{11}$-EG_4-OH, 95%, Sigma-Aldrich). Nanopure water (resistivity 18.2 MΩ-cm) was produced with a Barnstead NANOpure water system.

Synthesis and Characterization of Au@GSH (Compound 1)

A 50 mL conical was charged with 6 mL 100 mM glutathione (0.6 mmol, 3 equiv.) in 0.3 M NaOH solution. 2 mL of $HAuCl_4 \cdot 3H_2O$ in diethylene glycol dimethyl ether solution (0.2 mmol, 1 equiv., a non-metal spatula should be used to weigh out $HAuCl_4 \cdot 3H_2O$) was also added to the conical. The reaction was shaken at rt for 30 min. 5 min prior to the end of the 30 min, a suspension of 0.5 mM $NaBH_4$ in dry diethylene glycol dimethyl ether (about

19 mL) was sonicated at rt for 5 min. 17 mL of the $NaBH_4$ suspension of (0.0085 mmol, 0.043 equiv.) was added to the reaction which turned orange over about 20 seconds and was quenched by the addition of methanol (to a final volume of about 50 mL). The content of the conical was then mixed and then centrifuged in a swinging bucket rotor at 4,000 rpm and 4 ºC for 10 min. The clear and colorless supernatant was then decanted and the orange precipitate was air dried. Gel electrophoresis visualization was run on a 30% polyacrylamide gel (19:1, acrylamide : bisacrylamide) at 175 V for 3 h. The nanoparticle bands were visible by eye and with a UV transilluminator, thus no staining steps were performed for visualization.

Ligand exchange reaction of Au@GSH (1) cluster with 18-mercapto-3,6,9,12-tetraoxaoctadecan-1-ol (HS-$(CH_2)_6$-EG_4-OH) (Compounds 2 and 3).

A 500 μM solution of Au@GSH (0.001 mmol, 10 mg in 2 mL H_2O) and a 0.1 M solution of the HS-$(CH_2)_6$-EG_4-OH (0.04 mmol, 12.4 mg in 0.4 mL THF) were prepared. For the 1:1 incoming ligand:outgoing ligand reaction (Compound **2**): 1 mL of Au@GSH solution and 0.125 mL of HS-$(CH_2)_6$-EG_4-OH solution were mixed then diluted with H_2O to a final volume of 5 mL, shaken at rt for 1 h. The crude product was purified by ultrafiltration spin columns (5000 Da cutoff) and washed with 3 x 10 mL 1:1 H_2O:MeOH. The remaining orange liquid was placed into a 15 mL conical and was lyophilized until dry. For the 2:1 incoming ligand:outgoing ligand reaction (Compound **3**): 0.250 mL of HS-$(CH_2)_6$-EG_4-OH solution was used instead of 0.125 mL (see above).

Synthesis and Characterization of $Au_{102}pMBA_{44}$ (Compound 4).

Au_{102}*p*MBA_{44} was synthesized according to published procedure.[46] $HAuCl_4 \cdot 3H_2O$ was dissolved (0.209 g, 0.50 mmol, a non-metal spatula should be used to weigh out $HAuCl_4 \cdot 3H_2O$) in nanopure H_2O (19.0 mL, 0.028 M based on Au) in a 50 mL conical. In a separate 50 mL conical, *p*-mercaptobenzoic acid (0.292 g, 1.89 mmol) was dissolved in a solution composed of nanopure H_2O (18.43 mL) and 10 M NaOH (0.57 mL, 5.70 mmol). The resulting *p*-mercaptobenzoic acid/NaOH solution was 0.10 M based on *p*-mercaptobenzoic acid, 0.30 M based on NaOH, and the pH was determined to be >9. A 1 L Erlenmeyer flask was equipped with a stir bar and nanopure H_2O was added to it (51.5 mL). In three separate beakers, the following solutions were dispensed: 1) 0.028 M $HAuCl_4$ solution (17.8 mL, 0.5 mmol, 1.0 equiv.), 2) 0.10 M *p*-mercaptobenzoic acid / 0.30 M NaOH (15.5 mL, 1.5 mmol, 3.0 equiv. of *p*-mercaptobenzoic acid and 5.7 mmol, 11.4 equiv. of NaOH) solution, 3) MeOH (75 mL). Under stirring, the $HAuCl_4$ solution was poured into the 1 L Erlenmeyer flask (containing H_2O), this was immediately followed by the addition of the *p*-mercaptobenzoic acid/NaOH solution. The reaction turned from yellow to orange upon the addition of the *p*-mercaptobenzoic acid/NaOH solution. Immediately afterwards the beaker of MeOH was also added to the 1 L flask. The reaction was allowed to stir at room temperature for 1 h. During that time, the reaction turned from dark orange to light orange. After 1 hour, pulverized solid $NaBH_4$ (20.8 mg, 0.55 mmol, 1.1 equiv.) was added to the stirring reaction to reduce the polymer; the reaction continued to stir at room temperature for 17 h. The reaction turned black upon the addition of solid $NaBH_4$. After 17 h MeOH was added to the 1 L flask until the total volume was approximately 800 mL, then 5 M NH_4OAc (40 mL) was also added. The reaction was then split into about twenty 50 mL conicals, which were capped and then centrifuged in a swinging bucket rotor at 4,000 rpm

and 4 ºC for 10 min. The supernatant was then decanted and the precipitate was allowed to dry by inverting the conical on a paper towel for about 1 hour. The precipitate in each conical was then dissolved in about 200 μL of nanopure water. The nanoparticle solutions were then combined into 4 conicals. Next, the particles were washed by performing the following: 500 μL of 2 M NH_4OAc was added to each of the four conicals, then MeOH was added until the total volume in each conical was about 45 mL. The conicals were shaken to mix and were centrifuged at 4,000 rpm and 4 ºC for 10 min in a swinging bucket rotor. The resulting supernatant was decanted and the precipitates were dried *in vacuo* at room temperature for at least 2 h. Gel electrophoresis visualization was run on a 20% polyacrylamide gel (19:1, acrylamide : bisacrylamide) at 110 V for 2 h. The nanoparticle bands were visible by eye, thus no staining steps were performed for visualization. The synthesized particles were run against a standard Au_{102}*p*MBA_{44} sample of which the formula/structure has been confirmed by X-ray crystallography.

Fractional precipitation of $Au_{102}(pMBA)_{44}$

The reaction outcome varies depending on the quality of the solid $NaBH_4$. In the case where many large and/or insoluble products were formed, a simple fractional precipitation removed the majority of the larger products. First, all particles from the reaction were dissolved in nanopure water (9.24 mL) in a 50 mL conical, then 2 M NH_4OAc (0.76 mL, 1.52 mmol, 0.076 M final concentration) was added. The solution was thoroughly mixed followed by the addition of MeOH (10 mL, 50%). The suspension was shaken again to mix and the conical was centrifuged at 4,000 rpm and 4 ºC. The supernatant was decanted into a new 50 mL conical and then re-spun until pellets (larger

impurities) no longer formed. The remaining black solution (purified Au_{102}(*p*MBA)$_{44}$) was again transferred to a new 50 mL conical. MeOH was then added to the conical until the total volume was about 45 mL. The conical was shaken to mix and was then centrifuged at 4 ºC for 10 min. The resulting supernatant was decanted and the precipitate (purified Au_{102}(*p*MBA)$_{44}$) was dried *in vacuo* at room temperature for at least 2 h.

Deprotection of [11-(Methylcarbonylthio)undecyl]tetra(ethylene glycol) (AcS-$(CH_2)_{11}$-EG_4-OH)[35]

The acyl-protected thiol was refluxed at 100 ºC in 10% HCl/MeOH for 18 h. The reaction mixture was cooled and dichloromethane was added. The separated organic layer was washed twice with H_2O, twice with saturated $NaHCO_3$, and dried with Na_2SO_4. The solvent was removed in vacuo to give the product 23-mercapto-3,6,9,12-tetraoxatricosan-1-ol [HS-$(CH_2)_{11}$-EG_4-OH] as a clear oil. ^{1}H NMR (300 MHz, $CDCl_3$) δ 3.80-3.76 (m, 2H), 3.75-3.61 (m, 14H), 3.50 (t, *J* = 6.0 Hz, 2H), 2.58 (q, *J* = 6.0 Hz, 1H), 2.23 (brs, 1H), 1.70-1.58 (m, 4H), 1.47-1.29 (m, 14H).

Ligand exchange reaction of Au_{102}(pMBA)$_{44}$ with 23-mercapto-3,6,9,12-tetraoxatricosan-1-ol [HS-$(CH_2)_{11}$-EG_4-OH] (Compounds 5 and 6)

A 500 μM solution of Au_{102}*p*MBA$_{44}$ (6.6 μmol, 178 mg in 13.37 mL H_2O) and a 0.1 M solution of HS-$(CH_2)_{11}$-EG_4-OH (0.79 mmol, 304 mg in 7.90 mL THF) were prepared. For the 1:1 incoming ligand:outgoing ligand reaction (compound **5**): 3 mL of Au_{102}*p*MBA$_{44}$ solution and 0.66 mL of HS-$(CH_2)_{11}$-EG_4-OH solution were mixed and diluted with H_2O to a final volume of 15 mL. Then the reaction was shaken at rt for 1 h, then the crude product

was purified by ultrafiltration spin columns (5000 Da cutoff) and was washed with 3 x 10 mL 1:1 H_2O:MeOH. The remaining orange liquid was placed into a 15 mL conical and lyophilized until dry. For the 2:1 incoming ligand:outgoing ligand reaction (Compound **6**): 1.32 mL of HS-$(CH_2)_{11}$-EG_4-OH solution was used instead of 0.66 mL (see above).

Animal Models

Animals were housed in polycarbonate cages and kept on a 12 h light/dark cycle with water and food given ad libitum. C57BL/6NCr male mice, 8-14 weeks old, weighing 20 – 30 g, were purchased from the National Cancer Institute (Frederick, MD, USA). Compounds **1**-**4** were dissolved in nanopure water and compounds **5** and **6** were dissolved in 5% DMSO, 5% Tween-80 in 90% D5W solution. All the particle solutions were filtered through a 0.45 micron filter, and the dosage concentrations were determined after the filtration step. Approximate dosage concentration for compound **1** was 2.0 mM, both compounds **2** and **3** were 0.81 mM, compound **4** was 2.71 x 10^{-5} M, compound **5** was 3.14 x 10^{-5} M, and compound **6** was 5.94 x 10^{-5} M. Tail vein injection was carried out and the injection volume was 100 uL of solution / 25 g of mouse body weight. The mice were euthanized at 6, 12, 24, 48, 72, and 96 h time points via cardiac exsanguination under anesthesia (isoflurane). Urine and feces from 0-6 h were collected as they were produced in the cage. Feces from 6-12 h and 12-24 h were collected at the end of the time point from the cage. Urine from 6-12 h and 12-24 h were collected at the end of the time point by washing the cage with 20-30 mL nanopure water followed by lyophilization of the sample. The organs were collected at the end of each time point.

ICP-MS Analysis

Blood: Blood sample (0.5 mL) was measured out using a pipet in a 15 mL conical. Aqua regia (4 mL, approximately 3:1 HCl:HNO_3) was added to the conical and allowed to be stored at room temperature for two days with the conical gently capped. Water was then added to a final volume of 5 mL. Organs/feces: The organs/feces were weighted out in 15 mL conical. Samples that weighted more than 0.3 g were digested with 4 mL of aqua regia at room temperature over two days then diluted with water up to 5 mL total volume. Samples that weighted less than 0.3 g were digested with 2 mL of aqua regia at room temperature over 2 days then diluted with water up to 2.5 or 3 mL total volume. Urine: Liquid urine sample (typically 0.5 mL) was measured out using a pipet and lyophilized urine sample was treated as a dry powder. Aqua regia was added to the conical and incubated at room temperature for two days with the conical gently capped. Water was then added to a final volume of 5 mL. All the samples were sent to MidWest Laboratories, Inc. (Omaha, NE) for ICP-MS analysis.

Luminescence Images

Following collection of tissues for biodistribution, hepatic luminescence in the liver was determined using a cryogenically cooled IVIS 100 imaging system coupled to a data acquisition computer running LivingImage software (PerkinElmer, Waltham, MA. A digital grayscale image was acquired followed by acquisition and overlay of a pseudocolor image representing the spatial distribution of detected photons emerging from within the liver after subtracting background luminescence. Signal intensity was quantified as the sum of

all detected photons within the region of interest per second. The excitation (640 nm ± 25 nm) and emission (732.5 nm ± 37.5 nm) used the Cy 5.5 filters.

4.4 Results and Discussion

A grand challenge in the adaptation of nanoparticles for clinical purpose is the development of robust, predictive structure-activity relationships for *in vivo* nanoparticle behaviors such as ADME and PK. To advance toward this goal, we establish *in vivo* properties for the structurally characterized nanoclusters $Au_{25}(SR)_{18}$ and $Au_{102}(SR)_{44}$ where SR is either the thiolate ligand used in the native synthesis (glutathione for Au_{25} and *p*-mercaptobenzoic acid for Au_{102}) or ligand exchanged preparations of these clusters with mixtures of original ligand and tetraethylene glycol. We proceeded with these oligoethylene glycols because of literature showing that these molecules may suppress protein absorption thereby improving predictive biological properties, and also extend or allow the manipulation of blood PK.[4,15,19,36-38]

Predictive Modeling

For each of the compounds listed in Figure 1, we generated atomisitic models (Table 1). The inorganic portion of each atomistic model was taken from the X-ray crystal structure of either Au_{25}[39,40] or Au_{102}.[41] Ligand placement on exchanged models draws partially from our and other studies of structural ligand exchange, enabling some speculation as to the location of exchanged ligands.[42] For instance, in Au_{25}, the more exchangeable ligand sites are on those sulfur atoms that are closest to Au(0), and on Au_{102}, ligand exchange occurs at solvent exposed Au or adjacent Au atoms. From these atomistic

models, which are accurate for the as-synthesized product and a reasonable approximation as to the structure of ligand exchanged products, we calculated expected hydrodynamic diameter (with HYDROPRO[29]), net surface charge (by simple count), surface charge density (by PDB2PQR[32,33]), and hydrophobicity (by PyMOL).[28] The results of these calculations are summarized in Table 1. While these parameters are widely understood as biochemically significant, previous studies have focused primarily on net charge and hydrodynamic diameter as determinants of PK and excretion mechanism.

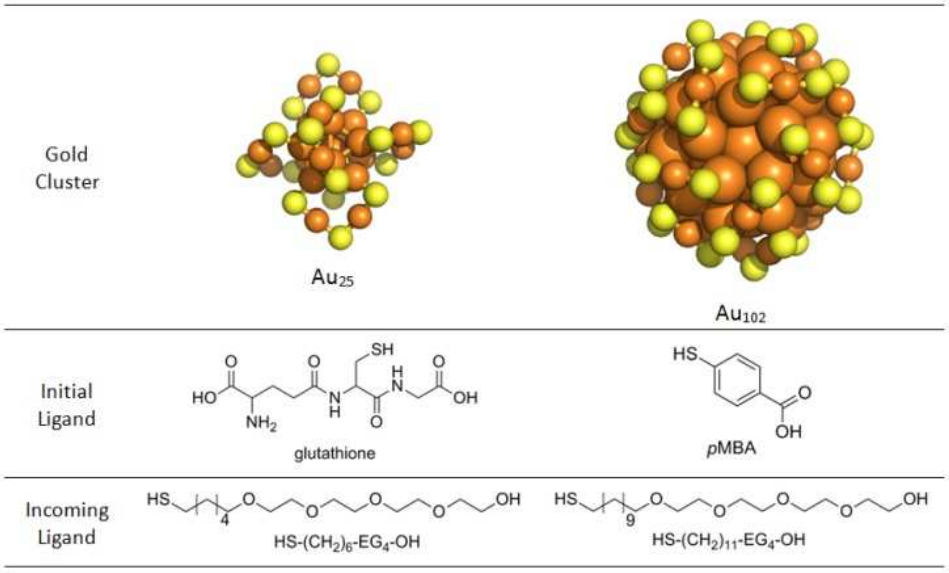

Figure 1. Structures of each molecular component used in the study. Orange spheres depict gold atoms and yellow spheres depict sulfur atoms. The carbon and hydrogen atoms of the ligand layer have been excluded for clarity.

Table 1. Theoretical Properties of Compounds 1-6

Compound	Proposed Molecular Formula	Calculated Stokes Diameter (nm)[a]	Net Surface Charge (e^-)	Surface Charge Density (Charge/Å^2)	Hydrophobic Surface Area (%)	Expected Clearance Mechanism % Renal / % RES
1	$Au_{25}(GSH)_{18}$	2.44	18^-	4.1×10^{-4} (-)	54%	100 / 0
2	$Au_{25}(GSH)_9$ $[S(CH_2)_6(EG)_4OH]_9$	4.55	9^-	1.9×10^{-4} (-)	62%	60 / 40
3	$Au_{25}(GSH)_6$ $[S(CH_2)_6(EG)_4OH]_{12}$	4.72	6^-	1.3×10^{-4} (-)	66%	60 / 40
4	$Au_{102}(p\text{MBA})_{44}$	3.28	44^-	1.1×10^{-3} (-)	72%	90 / 10
5	$Au_{102}(p\text{MBA})_{22}$ $[S(CH_2)_{11}(EG)_4OH]_{22}$	5.92	22^-	1.8×10^{-4} (-)	74%	40 / 60
6	$Au_{102}(p\text{MBA})_{14}$ $[S(CH_2)_{11}(EG)_4OH]_{30}$	6.24	14^-	9.8×10^{-5} (-)	75%	30 / 70

Atomistic models are especially useful in the case of small nanoclusters because methods for characterizing hydrodynamic diameter and surface charge, such as dynamic light scattering and particle tracking, have large errors for particles substantially smaller than 5 – 10 nm hydrodynamic diameter. Other properties calculated from these atomistic models, such as surface charge density, and hydrophobicity, are more difficult to measure directly and may allow post-experimental explanation of observed *in vivo* properties and development of more sophisticated structure-activity relationships.

Synthesis and Characterization of Au_{25}, Au_{102} & Exchange Products

The Au_{25} and Au_{102} nanoclusters are now well characterized by multiple groups.[39,43-45] The synthesis is described in greater detail in the experimental section. $Au_{25}(GSH)_{18}$ synthesis was by a novel method (manuscript in preparation) and $Au_{102}(p\text{MBA})_{44}$ as previously described.[46] Initial characterization of the $Au_{25}(GSH)_{18}$ by polyacrylamide gel electrophoresis used in this study suggested the presence of a single discrete product, but

subsequent characterization of this product after mouse experimentation had already begun showed the presence of multiple products of which $Au_{25}(GSH)_{18}$ is suggested as the largest product as determined by the visible color of this and other products.[47,48] The $Au_{102}(pMBA)_{44}$ product appears approximately pure as assessed by polyacrylamide gel electrophoresis (Supplementary Info, Figure S21.) There is some uncertainty in the exact nature of this preparation, because the subset of any $Au_{102}(p\text{MBA})_{44}$ preparation that crystallizes is small, and mass spec analysis suggests the presence of neighboring products.[46,49]

Oligoethylene glycol moiety containing (OEG, Figure 1) modifications of the as-synthesized Au_{25} and Au_{102} were made with of 1:1 and 2:1 incoming:outgoing ligand exchanges of OEG compounds shown in Figure 1 onto Au_{25} and Au_{102} cores as described in the experimental section. The molecular formulae of clusters following ligand exchange assumes equilibrium exchange conditions, which is a reasonable assumption given the time frame of the exchange. For Au_{25} this assumption results in average formula of $Au_{25}(GSH)_9(OEG)_9$ (**2**) and $Au_{25}(GSH)_6(OEG)_{12}$ (**3**), and for $Au_{102,}$ average formulae of $Au_{102}(p\text{MBA})_{22}(OEG)_{22}$ (**5**) and $Au_{102}(p\text{MBA})_{14}(OEG)_{30}$ (**6**).

ADME/PK of Au_{25}-based Compounds

The ADME/PK activities of each Au_{25}-based product (compounds **1**, **2**, and **3**) were tested in 8-14 weeks old C57BL/6NCr male mice. Time dependent absorption, biodistribution, and excretion was determined by ICP-MS analysis of gold content in lung, liver, kidney, blood, urine and feces from three mice per time point.

Figure 2 shows the blood drug levels of the Au_{25}-based compounds **1**, **2**, and, **3**. The pharmacokinetic parameters calculated by noncompartmental analyses are shown in Table 2. The calculated circulation half lives of compounds **1**, **2**, and **3** are relatively similar at 20.1, 16.0, and 15.6 hours respectively. Interestingly, modification with increasing coverage of OEG ligand (which also leads to the reduction of GSH coverage), there is an increase in area under the curve (AUC), and a reduction in half-life, clearance and apparent steady state volume of distribution (Table 2). These findings help support the ability to predict the whole blood PK parameters by "tuning" these nanoparticles.

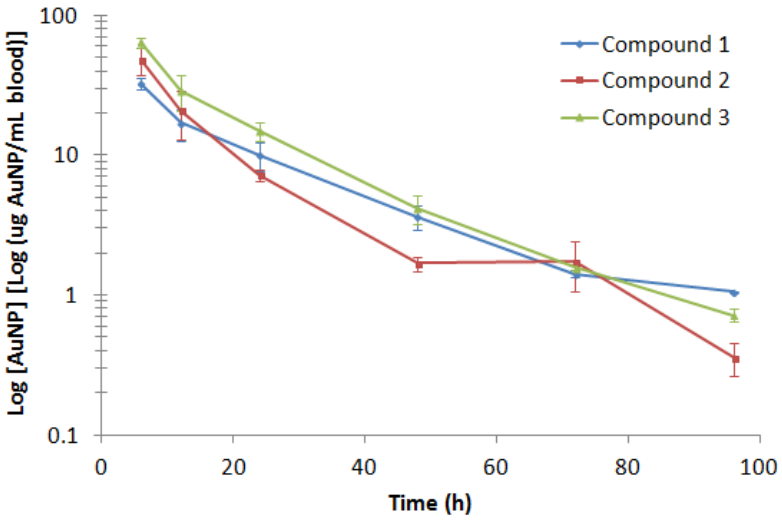

Figure 2. Blood drug concentration vs. time curves of Au_{25}-based compounds. Data represents the mean of three animals per time point per compound.

Time dependent distribution of Au_{25}-based compounds **1**, **2**, and **3** over a 96-hour time course are shown in Figure 3. Notably compound **1** appears to accumulate in the kidneys over the course of the experiment, while compounds **2** and **3** (those with OEG) – also have accumulations in the kidney but even more accumulate in the liver. This change

in distribution predicts the dominance of excretion into urine for compound **1** and in feces for compounds **2** and **3** observed (Figure S22). Analysis of excretion products, shown in Figure 4, confirms this, meaning that a small change in particle surface composition can dramatically change excretion mechanism.

Long term, potentially irreversible accumulation in filtration associated organs such as the lungs, liver and spleen is a major concern emerging investigation of metal nanoparticles in preclinical models.[50] Current studies suggest that smaller gold nanoparticles may be metabolized and excreted by hepatic mechanisms,[18] while larger gold nanoparticles persist in the liver indefinitely.[13] Metabolism of smaller particles may be by biologically sourced oxidative thiolate etching,[51] perhaps by intrinsic GSH, which results in $(\text{-Au(I)-SR-})_n$ oligomers similar to Au(I) based FDA approved rheumatoid arthritis drugs such as aurothiomalate (trade name Myochrisine.) The intrinsic luminesence of the $Au_{25}(SR)_{18}$ compound[52,53] allowed observation of the hepatic uptake and clearance of the hepatically cleared Au_{25}-based compound **3** over time. Figure 5 shows the luminescence of compound **3** in livers at the noted time points after administration. We suggest that etching precedes excretion, but speculate that since the analogous rheumatoid arthritis drugs are not associated with long term metal accumulation, that the Au(I)-SR etching products will be excreted. This does appear consistent with analysis of feces over the course of the experiment which shows increasing concentrations of Au as the experiment progressed toward its 96 hour termination point.

With no OEG, particles locate primarily to the kidneys and urine – consistent with the other observations of GSH-Au, although we surprisingly observe more kidney residence than other studies.[18] With an average of half a ligand shell of OEG (Compound **2**), particles

locate primarily in the liver, and with an average of two thirds of a ligand shell of OEG (Compound **3**) the particles locate initially in the lungs (Figure 3). While particles of similar size are known to locate to similar organ systems,[12,14,54] we believe this is the first observation of particle modification destination based on a mixed ligand shell composition.

Table 2. Whole Blood Pharmacokinetic Values of Compounds 1, 2, and 3[a]

Compound	$Dose_{ave}$ (mg)	$AUC_{0\rightarrow 96\ h}$ ($\mu g/mL$)*h	$t_{1/2}\lambda$ (h)	CL (mL/h)	V_{ss} (mL)
1	2.16	847	20.1	2.47	53.4
2	0.923	1020	16.0	0.797	10.4
3	0.989	1480	15.6	0.542	8.02

[a]Noncompartmental modeling was used for the calculation of pharmacokinetic parameters based on the composite data in Figure 2.

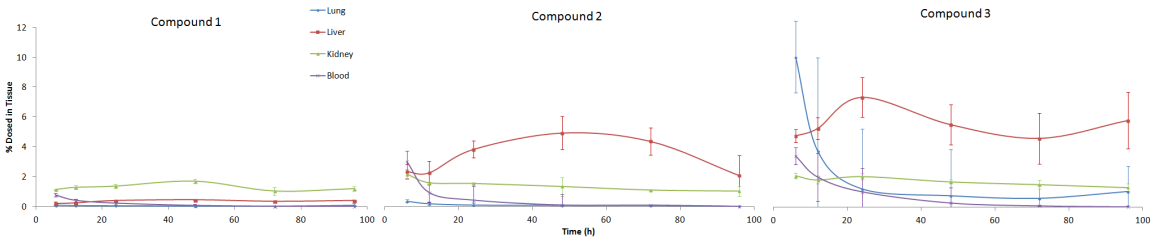

Figure 3. Percent of Au nanoparticles found (of total amount dosed) in tissue of Au_{25}-based compounds in various tissues at noted post-injection times. See Figure S31-S34 for the graphs zoomed in at the lower percentages.

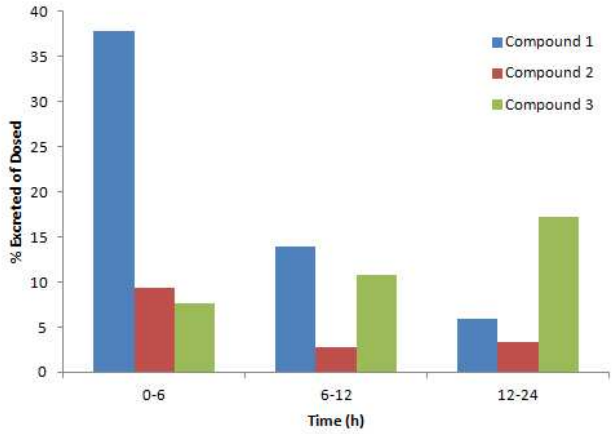

Figure 4. Percent of Au nanoparticles found (of total amount dosed) in excretion (urine and feces combined) for Au_{25}-based compounds.

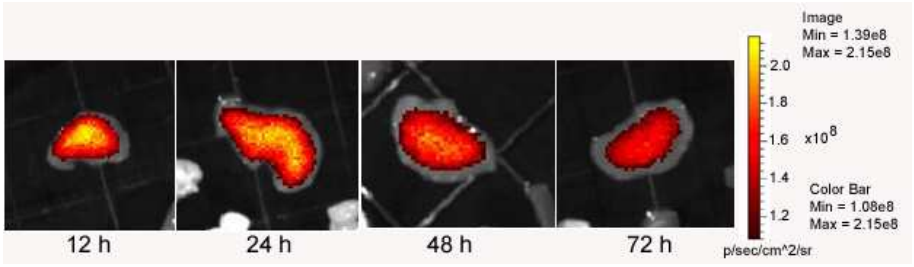

Figure 5. The luminescence within representative livers ex vivo at noted post-injection time points for compound **3**.

ADME/PK of Au_{102}

Establishing the ADME/PK properties of the $Au_{102}(pMBA)_{44}$ based compounds **4**, **5**, and **6** was attempted in the same manner as for the $Au_{25}(GSH)_{18}$ compounds **1**, **2,** and **3**. Analysis of time-dependent biodistribution and excretion suggests that the Au_{102} compounds locate primarily to the liver and spleen, regardless of the composition of the ligand shell (Figures 6, 7). In each case, the hydrodynamic diameter of the compound predicts substantial renal clearance, and the accumulation in RES suggests substantial binding of proteins to these particles, increasing their hydrodynamic diameter resulting in

RES accumulation. Surprisingly, the incorporation of OEG in these compounds did not change their distribution properties, indicating that in this case OEG did not suppress protein binding.

Analysis of excretion products for compounds **4** and **6** show excretion of 4.8% and 0.9% of the starting material within 12 hours. Figure S23 shows the relative amounts of each in urine and feces at 6, 12 and 24 hours post injection. Notably, excretion mechanism does not appear to change with ligand shell modification.

Predictive SAR may enable design of nanoparticles with predictable excretion mechanism, biodistribution, metabolism and blood PK. Precise and predictable tuning of these properties is desirable. Nanoparticles are investigated as diagnostic imaging agents, therapeutic agents, and combined theranostic agents. Each of these modalities has a different optimal corporeal half life[20].

The seminal work of *Choi et al*[4,5] suggested that the ADME/PK properties of inorganic nanoparticles and explicitly their excretion mechanism might be predicted by comparison to proteins with comparable hydrodynamic diameter, as long as the particles had a net surface charge of zero achieved either through zwitterionic ligands such as cysteine or neutral ligands such as oligoethylene glycols. Subsequent work from many groups demonstrate that nanoparticle ADME/PK is much more complex. For instance, particles with net-negative charge can avoid opsonization and protein corona formation which can dramatically increase the effective hydrodynamic diameter of nanoparticles, as judged by renal clearance. Thus, in some instances particles with a net negative charge behave as predicted by their hydrodynamic diameter,[7,18,37,55] but in other instances do not.[22] Moreover, the models for predictive ADME/PK do not yet account at all for the result

of targeting molecules (RGD, folate, antibodies, etc) on ADME/PK, which is a serious limitation.

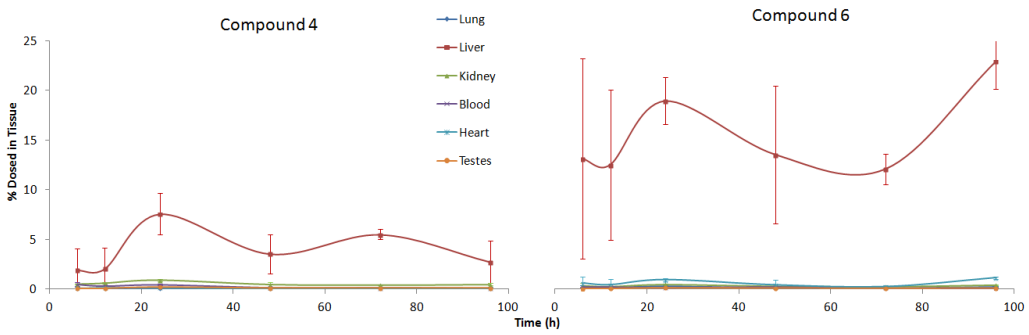

Figure 6. Percent of Au nanoparticles found (of total amount dosed) in tissue of Au_{102}-based compounds in various tissues at noted post-injection times. See Figure S35 & S37 for the graph zoomed in at the lower percentages.

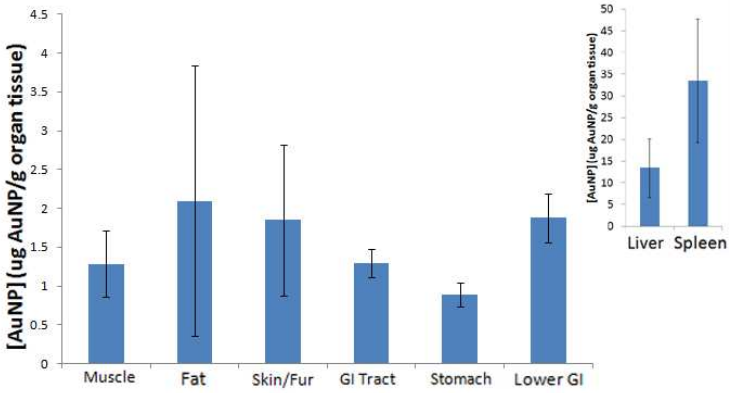

Figure 7. Concentration of compound **4** in various tissues at 24 h. The inset shows the concentration of compound **4** in the liver and spleen on a different scale.

In this study six compounds were tested, all with hydrodynamic diameter less than 6.25 nm. Since these diameters are smaller than the 8 nm cutoff commonly cited for filtration through the glomural wall of the kidney, and have net negative charge, substantial

renal excretion is predicted. This is observed only for compound **1**. To explain the excretion properties of compounds **2**, **3**, **4**, **5**, and **6**, we offer insights into SAR that arise from the atomistic models.

The distribution of compounds **2**, **3**, **4**, **5**, and **6** into the RES is consistent with an increase in their effective hydrodynamic diameter above the ~8 nm cutoff for renal filtration that can result from opsonization (absorption of immuno-proteins) and protein corona formation (absorption of other proteins.) The net negative charge of compounds **2**, **3**, **4**, **5**, and **6** and the addition of OEG are hypothesized to suppress these effects. Furthermore the apparent absorption of proteins to compounds **2** and **3** is especially surprising, as the OEG added to these compounds is hypothesized to decrease protein absorption compared to compound **1** because of several other studies that show decrease in protein binding as a result of OEG addition.[15,56]

A possible explanation for this unpredicted behavior arises from analysis of hydrophobic surface area in the atomistic models. Hydrophobic interactions are well known to drive substantial specific and non-specific biological interactions. Larger relative amounts of hydrophobic surface area on a nanoparticle might provoke both specific (immuno-) and nonspecific protein nanoparticle aggregation. Table 1 shows the calculated percentage of hydrophobic surface area for each compound, calculated in PyMol as described in the methods section. The amount of hydrophobic surface area increases after OEG addition because the OEG used in this study incorporates a C6 or C11 linker, separating the tetraethylene glycol functionality from the metal core. When packed into a monolayer, for instance on a sufficiently large {111} facet, this aliphatic region is buried and not solvent accessible. In the case of the small nanoclusters used in this study, two

aspects may expose the aliphatic region: First, the ligand shell is a mixed monolayer of GSH and OEG, and this may allow solvent exposure of the aliphatic region. Second, the high radius of curvature of the particles may expose the aliphatic region even in areas where the surface is essentially OEG saturated. Thus, especially in the case of compounds **2** and **3**, the Au_{25}-based nanoclusters, with an inorganic diameter of 1.1 nm, are the smallest OEG passivated particles studied *in vivo* so far, and small size and mixed ligand shell may account in large part for the unpredicted results.

The blood pharmacokinetics of the GSH protected particles indicates a substantially longer blood half-life than suggested by a simple hydrodynamic diameter calculation and comparison to naturally occurring proteins of similar size. For instance, the 2.44 nm hydrodynamic diameter of compound **1** is comparable to that of the inulin with a 3.0 nm hydrodynamic diameter.[4,57] These molecules have respective circulation half life of 20.1 hours and 9 minutes, respectively. The high density of negative charge on compound **1** may account for the long circulation half life, because glomerular filtration is faster for neutral or positively charged compounds.[58] Other published examinations of the properties of injected GSH protected nanoparticles show similarly extended circulation times with substantial renal clearance, indicating that this somewhat surprising result is not artifactual.[18]

4.5 Conclusions

For the first time, the circulation properties of nanomaterials characterized in terms of molecular formula are examined. We show that the characteristics (i.e., circulation half

life and especially biodistribution) of such particles depend critically upon their surface structure, as inferred from putative molecular formula atomistic models.

In aggregate, our results suggest that blood PK, distribution and excretion mechanism depend not only on the widely recognized parameters of net charge and hydrodynamic diameter, but also on exposed hydrophobic surfaces and surface charge density. Additionally, the specific 3-D structure of the organic portion of the cluster may also play an important role. Furthermore, we establish SAR properties for atomistically modeled particles, showing that renal clearance, transient lung accumulation, and RES accumulation are all highly sensitive to surface structure of nanoclusters, if not actual 3-D relationships of ligands. The increasingly precise surface modifications that now appear available[42] for some clusters may ultimately enable quantitative understanding.

We further show that the partial exchange with OEG in this instance increased the hydrophobicity of the nanoparticles, resulting in either opsonization or protein corona formation, resulting in particle entrapment in the reticuloendothelial system. These results in whole are superficially contradictory to many others that suggest that OEG increases circulation lifetime and biocompatibility, primarily by suppressing (rather than increasing as we observe here) protein absorption.

REFERENCES

1. J. F. Hainfeld, D. N. Slatkin, T.M. Focella and H.M. Smilowitz, *Brit. J. Radiol.* 2006, **79**, 248-253.

2. J. F. Hainfeld, M. J. O'Connor, F. A. Dilmanian, D. N. Slatkin, D. J. Adams and H. M. Smilowitz, *Brit. J. Radiol.* 2011, **84**, 526-533.

3. W. E. Ghann, O. Aras, T. Fleiter and M.-C. Daniel, *Langmuir* 2012, **28**, 10398–10408.

4. H. S. Choi, W. Liu, P. Misra, E. Tanaka, J. P. Zimmer, B. I. Ipe, M. G. Bawendi and J. V. Frangioni, *Nat. Biotechnol.* 2007, **25**, 1165–1170.

5. H. S. Choi, W. Liu, F. Liu, K. Nasr, P. Misra, M. G. Bawendi and J. V. Frangioni, *Nat. Nanotechnol.* 2010, **5**, 42–47.

6. T. Huang and R. Murray, *J. Phys. Chem. B* 2001, **105**, 12498–12502.

7. C. Zhou, M. Long, Y. Qin, X. Sun and J. Zheng, *Angew. Chem. Int. Ed.* 2011, **50**, 3168–3172.

8. J. Bresee, K. E. Maier, C. Melander and D. L. Feldheim, *Chem. Commun.* 2010, **46**, 7516–7518.

9. P. Cherukuri, E.S. Glazer and S.A. Curley, *Adv. Drug Deliv. Rev.* 2010, **62**, 339–345.

10. W. Chen, R. Bardhan, M. Bartels, C. Perez-Torres, R. G. Pautler, N. J. Halas and A. Joshi, *Mol. Cancer Ther.* 2010, **9**, 1028–1038.

11. R. Bardhan, S. Lal, A. Joshi and N. J. Halas, *Acc. Chem. Res.* 2011, **44**, 936–946.

12. G. Sonavane, K. Tomoda and K. Makino, *Colloid and Surface B* 2008, **66**, 274–280.

13. C. Lasagna-Reeves, D. Gonzalez-Romero, M. A. Barria, I. Olmedo, A. Clos, V. M. Sadagopa Ramanujam, A. Urayama, L. Vergara, M. J. Kogan and C. Soto, *Biochem. Biophys. Res. Commun.* 2010, **393**, 649–655.

14. W. H. De Jong, W. I. Hagens, P. Krystek, M. C. Burger, A. J. Sips and R. E. Geertsma, *Biomaterials* 2008, **29**, 1912–1919.

15. N. T. Huynh, E. Roger, N. Lautram, J.-P. Benoît and C. Passirani *Nanomedicine*, **5**, 1415–1433.

16. S. D. Perrault, C. Walkey, T. Jennings, H. C. Fischer and W. C. W. Chan, *Nano Lett.* 2010, **9**, 1909–1915.

17. E. Sadauskas, H. Wallin, M. Stoltenberg, U. Vogel, P. Doering, A. Larsen and G. Danscher, *Particle and Fibre Toxicology* 2007, **4**, 10.

18. C. A. Simpson, K. J. Salleng, D. E. Cliffel and D. L. Feldheim *Nanomedicine: Nanotechnology, Biology and Medicine*, 2013, **9**, 257-263.

19. W.-S. Cho, M. Cho, J. Jeong, M. Choi, H. Y. Cho, B. S. Han, S. H. Kim, H. O. Kim, Y. T. Lim, B. H. Chung and J. Jeong, *Toxicol. Appl. Pharmacol.* 2009, **236,** 16–24.

20. Z. Cheng, A. A. Zaki, J. Z. Hui, V. R. Muzykantov and A. Tsourkas, 2012, **338**, *Science* **338,** 903–910.

21. Y. Matsumura and H. Maeda, *Cancer Res.* 1986, **46,** 6387–6392 .

22. C. A. Simpson, B. J. Huffman, A. E. Gerdon and D. E. Cliffel, *Chem. Res. Toxicol.* 2010, **23**, 1608-1616.

23. Y. Pan, S. Neuss, A. Leifert, M. Fischler, F. Wen, U. Simon, G. Schmid, W. Brandau and W. Jahnen-Dechent, 2007, *Small* **3**, 1941–1949.

24. Y. Pan, A Leifert, D. Ruau, S. Neuss, J. Bornemann, G. Schmid, W. Brandau, U. Simon and W. Jahnen-Dechent, *Small* **5**, 2009, 2067–2076.

25. M. Walter, J. Akola, O. Lopez-Acevedo, P. D. Jadzinsky, G. Calero, C. J. Ackerson, R. L. Whetten, H. Grönbeck and H. Häkkinen *Proc. Natl. Acad. Sci. U S A* 2008, **105**, 9157–9162.

26. R. Jin, *Nanoscale* 2010, **2**, 343–362.

27. A. W. Schüttelkopf and D. M. F. van Aalten, *Acta Crystallogr. D* 2004, **60**, 1355–1363.

28. W. deLano, PyMol User Manual.

29. A. Ortega, D. Amorós, D. and J. García de la Torre, *Biophys. J.* 2011, **101**, 892–898.

30. S. Chien, S. Usami, H. M. Taylor, J. L. Lundberg and M. I. Gregersen, *J. Appl. Physiol.* 1966, **21**, 81–87.

31. H. Durchschlag and P. Zipper, *Ultracentrifugation*, ed. M. D. Lechner, Springer, Darmstadt, **1994**, 20–39.

32. T. J. Dolinsky, P. Czodrowski, H. Li, J. E. Nielsen, G. Klebe and N. A. Baker, *Nucleic Acids Res.* 2007, **35**, W522–5.

33. T. J. Dolinsky, J. E. Nielsen, J. A. McCammon and N. A. Baker, *Nucleic Acids Res.* 2004, **32**, W665–7.

34. N. A. Baker, D. Sept, S. Joseph, M. J. Holst and J. A. McCammon, *Proc. Natl. Acad. Sci. USA* 2001, **98**, 10037–10041.

35. I. Choi, Y.-K. Kim, D.-H. Min, S. Lee and W.-S. Yeo, *J. Am. Chem. Soc.* 2011, **133**, 16718–16721.

36. L. Tong, Q. Wei, A. Wei and J.-X. Cheng, *Photochem. Photobiol.* 2009, **85**, 21–32.

37. C. A. Simpson, A. C. Agrawal, A. Balinski, K. M. Harkness and D. E. Cliffel, *ACS Nano* 2011, **5**, 3577-3584.

38. D. Kim, S. Park, J. H. Lee, Y. Y. Jeong and S. Jon, *J. Am. Chem. Soc.* 2007, **129**, 7661–7665.

39. M. W. Heaven, A. Dass, P. S. White, K. M. Holt and R. W. Murray, *J. Am. Chem. Soc.* 2008, **130**, 3754–3755.

40. M. Zhu, C. M. Aikens, F. J. Hollander, G. C. Schatz and R. Jin, *J. Am. Chem. Soc.* 2008, **130**, 5883–5885.

41. P. D. Jadzinsky, G. Calero, C. J. Ackerson, D. A. Bushnell and R. D. Kornberg, *Science* 2007, **318,** 430–433.

42. C. L. Heinecke, T. W. Ni, S. Malola, V. Mäkinen, O. A. Wong, H. Häkkinen and C. J. Ackerson, *J. Am. Chem. Soc.* 2012, **134**, 13316–13322.

43. T. Schaaff, G. Knight, M. Shafigullin, R. Borkman and R. L. Whetten, *J. Phys. Chem. B*, 1998, **102**, 10643–10646.

44. M. A. Muhammed, P. K. Verma, S. K. Pal, R. C. Kumar, R. V. Omkumar and T. Pradeep, *Eur. J. Chem.* 2009, **15,** 10110–10120.

45. M. A. Tofanelli and C. J. Ackerson, *J. Am. Chem. Soc.* 2012, **134**, 16937-16940.

46. O. A. Wong, C. L. Heinecke, A. R. Simone, R. L. Whetten and C. J. Ackerson, *Nanoscale*, 2012, **4**, 4099-4012.

47. T. Schaaff and R. L. Whetten, *J. Phys. Chem. B* 2000, **104**, 2630–2641.

48. Y. Negishi, K. Nobusada and T. Tsukuda, *J. Am. Chem. Soc.* 2005, **127**, 5261–5270.

49. Y. Levi-Kalisman, P. D. Jadzinsky, N. Kalisman, H. Tsunoyama, T. Tsukuda, D. A. Bushnell and R. D. Kornberg, *J. Am. Chem. Soc.* 2011, **133**, 2976–2982.

50. R. Arvizo, R. Bhattacharya and P. Mukherjee, *Expert. Opin. Drug Deliv.* 2010, **7**, 753–763.

51. T. Schaaff and R. L. Whetten, *J. Phys. Chem. B* 1999, **103**, 9394–9396.

52. Z. Wu and R. Jin, *Nano Lett.* 2010, **10**, 2568–2573.

53. A. Templeton, S. Chen, S. Gross and R. W. Murray, *Langmuir* 1999, **15**, 66–76.

54. M. Semmler-Behnke, W. G. Kreyling, J. Lipka, S. Fertsch, A. Wenk, S. Takenaka, G. Schmid and W. Brandau, *Small* 2008, **4,** 2108–2111.

55. H. Mattoussi and V. M. Rotello, *Adv. Drug Deliv. Rev.* 2013, **65**, 605-606.

56. M. P. Monopoli, C. Aberg, A. Salvati and K. A. Dawson *Nat. Nanotechnol.* 2012, **7,** 779–786.

57. L. F. Prescott, J. A. N. McAuslane and S. Freestone *Eur. J. Clin. Pharmacol.* 1991, **40**, 619–624.

58. B. M. Brenner, T. H. Hostetter and H. D. Humes *Am. J. Physiol.Renal Physiol* 1978, **234**, F455–60.

CHAPTER 5

Dynamic Diglyme-Mediated Self-Assembly of Gold Nanoclusters

5.1 Synopsis

We report the assembly of gold nanoclusters by the non-thiolate ligand diglyme into discrete and dynamic assemblies. To understand this surprising phenomenon, the assembly of $Au_{20}(SC_2H_4Ph)_{15}$-diglyme into $Au_{20}(SC_2H_4Ph)_{15}$-diglyme-$Au_{20}(SC_2H_4Ph)_{15}$ is explored in detail. The assembly is examined by high-angle annular dark field scanning transmission electron microscopy, size exclusion chromatography, mass spectrometry, IR spectroscopy, and calorimetry. We establish a dissociation constant for dimer to monomer conversion of 20.4 μM. Theoretical models validated by transient absorption spectroscopy predict a low-spin monomer and a high-spin dimer, with assembly enabled through weak diglyme oxygen-gold interactions. Close spatial coupling allows electron delocalization between the nanoparticle cores. The resulting assemblies thus possess optical and electronic properties that emerge as a result of assembly.

5.2 Introduction

Modern gold nanoscience builds substantially on the still-used 1951 Turkevich synthesis of citrate passivated colloidal gold.[1] Subsequent synthetic developments

---

[*] *The work presented herein is published in ACS Nano. W. Scott Compel's contributions include experimental design, data analysis, and synthetic development and characterization of gold nanoclusters and assemblies.* *ACS Nano*, ***2015***, *9(12), 11690–11698*.

produce gold nanoparticles (AuNPs) passivated by an array of electron donating ligands,[2] including amines,[3,4] phosphines[5] and thiolates.[6]

The notable works of Mingos[7] underpin the contemporary investigation of <1 nm gold "nanoclusters" (AuNC), referred to as such due to their molecular character.[8] While exciting recent developments in phosphine-protected AuNCs are recently reported,[9] thiolate protected gold spurs the majority of contemporary AuNC research. Thiolate ligation produces the most stable AuNPs due to the covalent nature of the Au-S bond.

The high stability of thiolate-protected AuNP allows their use in downstream applications, many of which involve self-assembly. The self-assembly of metal nanoparticles driven by interactions of surface-anchored ligands such as DNA,[10] multivalent thiolates,[11] and proteins[12,13] results in 1-, 2-, and 3-dimensional nanoparticle superstructures.[14,15] Such superstructures display emergent fundamental properties absent in discrete metal nanoparticles allowing applications in sensing,[16,17] plasmonics[18] and biology.[19-21] In the pioneering works of Alivisatos, AuNP dimers were tethered through complementary ssDNA pair hybridization.[14,22] Subsequent work on DNA based assembly now produces an impressive array of planet-satellite bundles and close-packed lattices.[23] However, most self-assembled AuNP superstructures are static, with any plasticity in the assembly resulting from plasticity in the ligand.

Here we report on self-assembly of AuNCs mediated by Au-Ligand interactions with non-thiolate ligands. Our findings have some precedent in recent work showing that para-amino phenylthiolate ligands can similarly provoke aggregation (non-discrete assemblies).[24]

We observed this apparently general formation of diethylene glycol dimethyl ether (diglyme, dg) mediated self-assembly events during a recent synthetic screen of solvents.[25] Here we found that AuNCs synthesized in the presence of diglyme as a cosolvent would self-assemble (Figure 1) where extent of assembly is apparently an equilibrium-governed process. Purification of any discrete assembly resulted regeneration of all constituents of the original mixture. The post-synthetic assembly is observed *only if diglyme is a synthetic cosolvent.* The observed assembly required no post-synthetic treatment of the AuNC, implying that the attractive force between particles arises from diglyme-induced surface modifications of the AuNC. Similar apparent self-assembly of nanoclusters syntheiszed in diglyme cosolvent systems was observed for glutathione, *p*-mercaptobenzoic acid, and phenylethane thiolate (PET) protected gold nanoclusters. Our characterization of this system suggests that synthesis of gold nanoclusters in diglyme results in clusters that incorporate the solvent as a ligand, in a manner reminiscent of hot-injection synthesis of semiconductor quantum dots.[26]

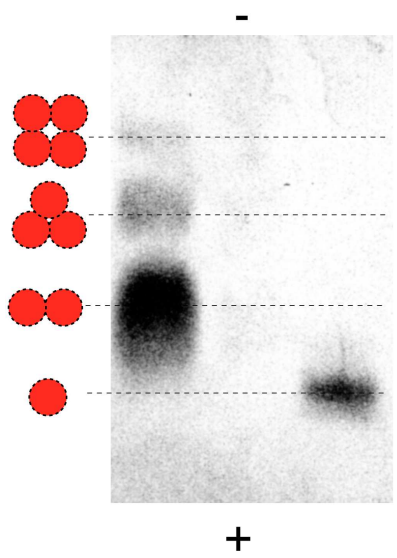

Figure 1. PAGE image of post-synthetic self-assembly of glutathione-protected AuNCs. The purified AuNC, seen on the right of the gel, was exposed to diglyme and heat to produce the assembled structures seen on the left of the gel. Attempting to extract the clusters from the gel resulted in dissociation into smaller assemblies, *i.e.,* extraction of the band corresponding to the trimer would appear to have trimer, dimer, and monomer when run on PAGE again.

To gain greater insight into this apparently general route to diglyme-mediated nanoparticle assembly, we completed the detailed study of the single product and resulting assembly of PET-protected nanoclusters synthesized in a diglyme cosolvent system. We chose to complete the study with PET ligation instead of *p*-mercaptobenzoic acid or glutathione ligation because characterization of organosoluble compounds is more facile than for water-soluble compounds.

5.3 Experimental Methods

Chemicals

Gold(III) chloride trihydrate ($HAuCl_4 \bullet 3H_2O$, ACS reagent, ≥49.0% Au basis), sodium borohydride ($NaBH_4$, powder, ≥98.0%) and 2-phenylethanethiol ($PhCH_2CH_2SH$, ≥99%) obtained from Sigma-Aldrich was used as received. Tetrahydrofuran (ACS reagent, ≥99.0%) and diethylene glycol dimethyl ether (diglyme, anhydrous, 99.5%) were obtained from Sigma-Aldrich and stored over activated molecular sieves. Other solvents: methanol (ACS reagent, ≥99.8%), hexanes (anhydrous, 95%), dichloromethane (spectral grade, stabilized), chloroform (ACS reagent, stabilized). Silica gel used in chromatography: high-purity grade, pore size 60 Å, 2-25 μm particle size, without binder, pore volume 0.75 cm^3/g, (Sigma-Aldrich). Bio-Beads SX-1 (styrene divinylbenzene) beads were used for size exclusion chromatography: 1% crosslinkage, 40–80 μm bead size, 600–14,000 MW exclusion range. For electrochemistry, the supporting electrolyte used was tetrabutylammonium hexafluorophosphate ($TBAPF_6$, >98%) obtained from TCI Chemicals and recrystallized in methanol.

Purification of Au clusters

Normal phase silica gel flash column chromatography was used to separate out the crude clusters with no prior purification necessary. A solution of 9:11 hexanes:chloroform was used as the mobile phase. Fractions were collected directly into methanol-filled and LN_2-chilled glass centrifugation tubes. This precipitates clusters following elution, preventing interconversion. Spinning the tubes containing product at 1811 g (maximum for our glass tubes) for 5 min at 4 ºC sediments the clusters and the clear supernatant is

discarded. Products are air dried in the centrifugation tubes. This results in $Au_{20}(PET)_{15}$(dg), **1**, and $(Au_{20}(PET)_{15})_2$(dg), **2**, as yellow and orange powders, respectively. Products are stored under argon in the dark. An example thin layer chromatography (TLC) plate is shown in Figure 17, revealing purity of **1** and **2** after column elution. Extinction coefficients of **1** and **2** were determined from known masses of **1** and **2.**

For size exclusion chromatography, beads were allowed to swell in THF overnight. A 60-cm long (2.5 cm diameter) column was filled to 40 cm height. The column was flushed with 500 mL of THF before each separation. Samples were loaded onto the column and absorbance was measured on fractions collected in 15 second intervals (total volume of fractions was dependent on flowrate, which was emperically determined for each run, and was typically between 0.25 – 0.50 mL). Standards used for calibration were recrystallized $Au_{25}(PET)_{18}$ and $Au_{144}(PET)_{60}$, which are approximately spherically symmetric.

Instrumentation

Linear absorbance spectra were measured in a NanoDrop 2000c Spectrophotometer and a Hewlett-Packard 8452A diode array spectrophotometer. Kinetics measurements were acquired on an Evolution 300 spectrophotometer (Thermo Electron) in a sealed cuvette, preventing solvent evaporation. The ratio of absorbance at 454 and 484 nm, local minimum and maximum for **2**, was used to quantify the relative amount of **1** and **2** in mixtures as equilibrium was reached. The ratio change over time was calculated under the assumption that the molecular weight of **1** and **2** were 5,997.7 and 11,995.4 Da, respectively. Together with the known extinction coefficients of **1** and **2** and 454 and 484

nm, this provided a quantifiable relative concentration of **1** and **2** in mixtures of the clusters.

Matrix-assisted laser desorption/ionization mass spectroscopy (MALDI-MS) spectra were obtained with a Bruker Ultraflex MALDI-TOF/TOF using the matrix trans-2-[3-(4-tert-Butylphenyl)-2-methyl-2-propenylidene]malononitrile (DCTB). Solid sample was dissolved in a minimal amount of DCTB (10 mg/mL, $CHCl_3$). Typically, ~3 μL was spotted on the plate and allowed to air dry for 30 min. Dissolved single crystals of $Au_{25}(PET)_{18}$ were used to determine the optimal laser power, accellerating voltage, and detector gain. Identical parameters were subsequently used to obtain spectra of **1** and **2**. Spectra were collected in reflective positive mode for greatest resolution.

Infrared (IR) spectra of ~1 mg of solid samples were measured on a Thermo Nicolet 380 FT-IR (ATR on ZnSe).

A TA TGA 2950 Thermogravimetric analyzer was used for thermogravimetric analysis (TGA). Roughly 1.5580 mg of sample was placed in a platinum pan. Temperature increased at 10 ºC/min to 400 ºC and N_2 flow rate was kept at 55 mL/min.

A TA Modulated 2920 differential scanning calorimeter (DSC) was used to measure thermal stability. For both **1** and **2**, 1.500 mg of sample was used. Temperature increased at 10 ºC/min to 400 ºC and N_2 flow rate was kept at 90 mL/min.

Differential pulse voltammetry (DPV) was performed in dichloromethane solutions containing 100 mmol $TBAPF_6$ using a CH Instruments CHI750D potentiostat.

Centrifugation was in an Eppendorf 5810 R Centrifuge. Sonication was used to assist dissolution of BH_4 in a Digital Ultrasonic Cleaner UD50SH-2L.

HAADF-STEM images were obtained with a JEOL JEM 2100F operated at 200 kV and using the JEOL ADF detector at 20 cm camera length. Images were collected at 1MX magnification using a 1024 x 1024 scan. Samples were deposited onto carbon coated copper grids after a 1 minute full power plasma discharge (Harrick Plasma Cleaner) under vacuum. For the first 30 seconds of plasma discharge, toluene fumes were vented to the vacuum chamber at a rate empirically determined to preserve the plasma..

Transmission Electron Microscopy

Particles imaged with transmission electron microscopy (TEM) were analyzed using the freely available software ImageJ.[6] The ~1 nm particles of interest were difficult to clearly distinguish from grid background in the original image. Adapting procedures used to clarify the particle edges in quantum dots[7] allowed for greater particle resolution. Adjusting the threshold of the original dark-field image effectively eliminates noise by making a binary image; remaining noise is excluded while measuring particles by limiting the area of particles to analyze to > 0.5 nm^2 with sphericity of > 0.5.

Particle agglomeration due to drying was impeded by plasma cleaning the grid in the presence of toluene prior to sample deposition to increase the surface affinity of the individual particles. To do this, the grid was placed on a piece of filter paper in a glass dish and plasma cleaned in Ar/O_2 80/20 gas mixture for 10 min next to a piece of filter paper saturated with HPLC-grade toluene. The dish containing the grid was removed and 1 μL of pure **2** (~10 μM in HPLC-grade toluene) was dropped onto the grid; the solution quickly dispersed across the entire grid and onto the clean filter paper underneath.

Radii were calculated from areas provided by ImageJ assuming the particles were circular. Seven different HAADF-STEM images (an example seen in Figure 7) were analyzed in an identical manner, and resulting histograms can be seen in Figure 8. Because the particles in each image suffer from an inconsistent amount of beam damage, the perceived sizes are different for each image. Due to this, histograms of perceived radii could not be summed together before normalizing the data to a point. Since the second peak in each histogram is centered at 1.0 nm in most cases, the outlying histograms were shifted so that the second peak was centered at 1.0 nm. After this necessary normalization step, the frequency of each calculated radii was summed and the resulting histogram seen in Figure 8 was used for our analysis. Though the accuracy of the measured radii is thus questionable, the ubiquitous bimodal distribution in each micrograph is testament to the presence of monomer and dimer throughout the sample.

Preventative measures were developed to diminish electron beam damage resulting in particle sintering. Contamination in TEM imaging was suppressed by using a 100 micron condenser aperture instead of the nominal 40 micron aperture. This provided that the beam was spread to about 180 nm diameter on the sample. Contamination in STEM imaging was minimized using 1MX low magnification scanning.

Synthesis

A 250-mL Erlynmeyer flask was charged with 2-phenylethanethiol (48 mL, 100 mM, 4.8 mmol, 3 equiv.) in tetrahydrofuran and $HAuCl_4 \cdot 3H_2O$ (16 mL, 100 mM, 1.6 mmol, 1 equiv.) in diethylene glycol dimethyl ether (diglyme) solution was added to the reaction flask. The reaction was stirred at room temperature for 3 h or until the cloudy yellow

solution turned milky white. 5 min prior to the end of the 3 h, a suspension of $NaBH_4$ in diglyme (8 mL, 50 mM, 0.8 mmol, 0.5 equiv.) was sonicated at room temperature for 5 min. 120 mL of diglyme was added to the reaction vessel, followed by dropwise-addition of 8 mL of the $NaBH_4$ suspension over the course of 1 minute. The reaction appears yellow/orange, indicating the formation of both $Au_{20}(PET)_{15}$dg and the dimer. The reaction is allowed to stir at room temperature for an additional hour. Precipitated by-products were filtered out using a Büchner funnel with medium frit, and the remaining orange solution was transferred to a 1-L fleaker. The reaction was quenched *via* the addition of methanol to 1 L, and the quenched solution was split into 20 50-mL polypropylene centrifugation conicals tubes. Centrifugation proceeds in a swinging bucket rotor at 4,000 rpm and 4 ºC for 10 min. The clear and colorless supernatant is decanted and the orange precipitate was air-dried. Thin layer chromatography was run using 9:11 hexanes:chloroform to characterize the product.

Density Functional Theory

Computations for the model structures were performed with density functional theory code GPAW,[48] which implements projector-augmented wave method in a real-space grid. The real space had a grid spacing 0.2 Å. Au($5d^{10}6s^1$), S($3s^23p^4$), C($2s^22p^2$), O($2s^22p^4$) and H($1s^1$) electrons were regarded as the valence, and the PAW setups for Au included scalar-relativistic corrections. Total energies were evaluated at the GGA-PBE level (gradient-corrected functional of Perdew, Burke and Ernzerhof).[49] All calculations were spin-polarized. All the atoms were relaxed during the geometry optimization until the maximum force acting on atoms below 0.05eV/Å. Optical absorption spectra were

calculated with the PBE level using spin-polarized linear-response (LR) time-dependent DFT (LR-TDDFT) formalism in GPAW.[50]

Spectroscopy

The femtosecond pump-probe laser system has been described previously,[51] and details are provided as supporting information. Both species 1 and 2 were excited using the 400-nm second harmonic of an amplified Ti:sapphire laser, and transient spectra and dynamics were recorded using temporally delayed continuum laser pulses. The polarization state of the pump and probe laser pulses was set using a combination of linear polarizers and wave plates. Transient dynamics were analyzed using software program written in house. The data acquisition time for each pump-probe measurement was less than one hour. A fresh sample was used in a flow cell for each scan to avoid decomposition.

We validated the theoretical predictions of a zero-spin multiplicity for **1** and triplet-spin multiplicity for **2** through femtosecond time-resolved transient absorption pump-probe measurements to compare the electronic relaxation dynamics of **1** and **2.** Consistent with both linear absorption and theoretical calculations (Figure 4A), the differential absorption spectrum of **2**, resulting from 400-nm excitation, showed a prominent transient bleach centered at 484 nm and broad excited-state absorption (ESA) at longer wavelengths (Figure 7A). In contrast, the transient difference spectrum of **1** consisted only of broad ESA; the transient bleach at 484 nm was specific to **2**.

5.4 Results and Discussion

The synthesis of PET-protected AuNC in a 3:1 diglyme:tetrahydrofuran (THF) solvent mixture results in two major products. These products, which are yellow (**1**) and orange (**2**) under ambient lab lighting, are isolable by silica gel chromatography. While stable as dry powders, these products interconvert in solution to form a mixture comprised of **1** and **2.** Fractionation of the mixture by thin layer chromatography, silica gel chromatography or size exclusion chromatography results again in only pure **1** and **2**. Three hypotheses were considered to account for interconversion: (i) **1** and **2** are redox pairs, (ii) **1** and **2** are isomers, or (iii) **2** is an assembly of **1**.

The hypothesis of **1** and **2** existing in different oxidation states was tested using differential pulse voltammetry. It was found that the clusters exhibit irreversible electrochemical behavior, indicating that **1** and **2** are unlikely to represent different oxidation states (Figure 2).

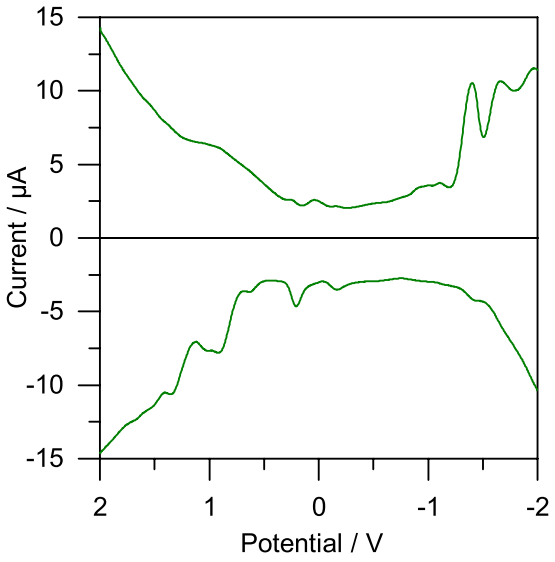

Figure 2. Differential pulse voltammogram of equilibrium mixture of **1** and **2** (100 mM, CH_2Cl_2). The mixture exhibits irreversible electrochemical behavior, indicating that the clusters are unlikely to be redox pairs.

We tested the hypothesis that **1** and **2** are isomers by size exclusion chromatography (SEC) following protocols previously successful in separating $Au_{38}(PET)_{24}$ from $Au_{40}(PET)_{24}$.[27] The column was calibrated using recrystallized $Au_{25}(PET)_{18}$ and $Au_{144}(PET)_{60}$ as standards, representing approximately spherical compounds as known from x-ray crystallography[28] and combined theoretical-TEM studies.[29] SEC suggests a Stokes-Einstein radius of 0.78 nm for **1** and 0.94 nm for **2**, which correspond to molecular weights of 6.0 kDa and 10.0 kDa (Figure 3a). We ruled out the possibility that **1** and **2** are isomers because of the apparently large difference in hydrodynamic diameter.

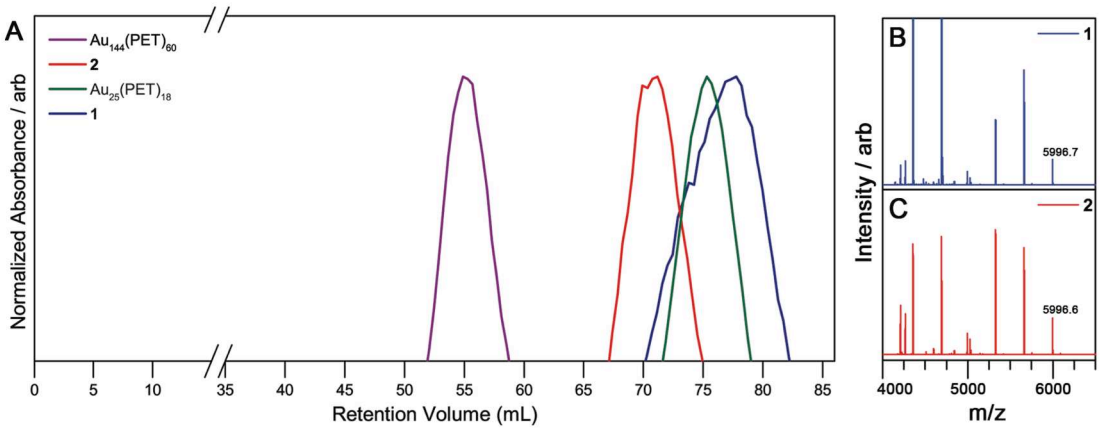

Figure 3. The size and mass of products **1** and **2** as determined by size exclusion chromatography and mass spectrometry. Panel A shows the size exclusion chromatography of **1** and **2** relative to the well known gold nanoparticles $Au_{144}(PET)_{60}$ and $Au_{25}(PET)_{18}$. Panels B and C show the MALDI mass spectrum of each product.

Matrix-assisted laser desorption ionization (MALDI) mass-spectrometry produces nearly-identical spectra for **1** and **2** when analyzed under identical conditions (Figure 3b, 3c). The parent peaks for **1** and **2** are 5996.7 and 5996.6 m/z, respectively, which correspond to the formula $Au_{20}(PET)_{15}$ with a molar mass of 5997.7 Da. All peaks at lower m/z are assignable as laser-induced fragments (-AuSR) of the parent, which is a known and expected result of analyzing AuNC under the ionization conditions of MALDI.[30,31] No other peaks are apparent at higher m/z (Figure 4), implying that the samples studied are pure, and the theoretical isotope pattern for $Au_{20}(PET)_{15}$ agrees with the experimentally obtained spectrum (Figure 5). We validated our mass spectrometry methods by verifying that recrystallized $Au_{25}(PET)_{18}$ gives the expected spectrum (Figure 6).

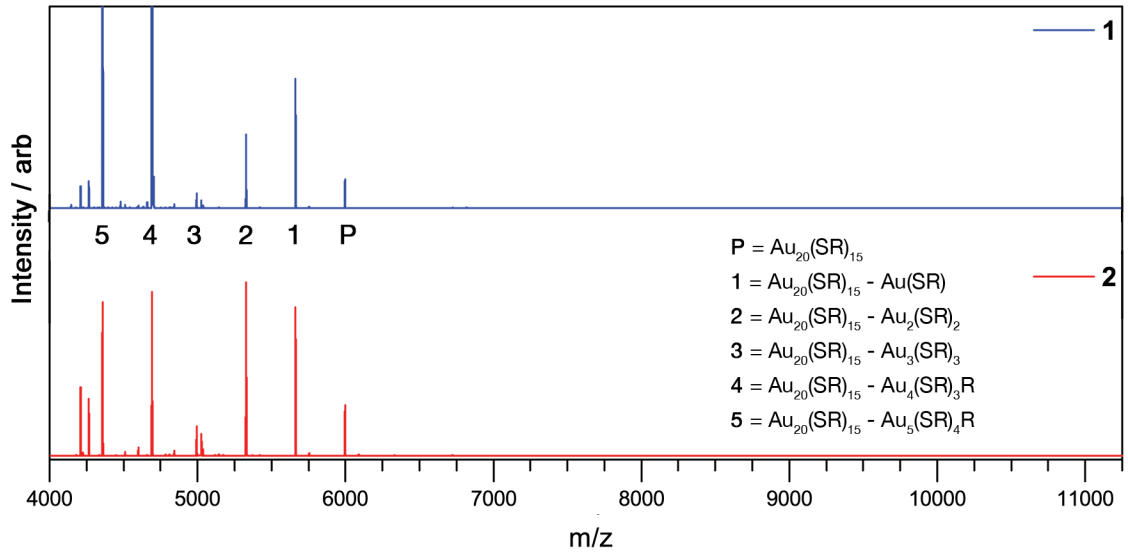

Figure 4. Full MALDI spectra of **1** and **2**. Parent peak corresponds to $Au_{20}(PET)_{15}$ with lower peaks corresponding to expected –Au(SR) fragments. Lack of peaks higher than 6000 m/z indicates that the samples studied were pure.

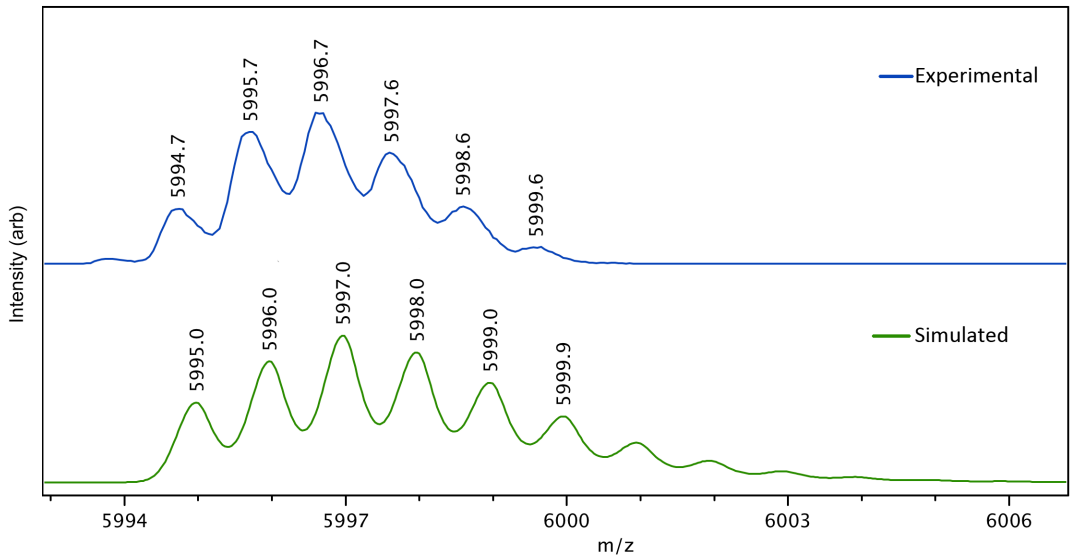

Figure 5. Experimental MALDI mass spectra matches simulated isotope pattern of $Au_{20}(PET)_{15}$ parent mass. The ~0.3 *m/z* discrepancy is attributed to error in calibration.

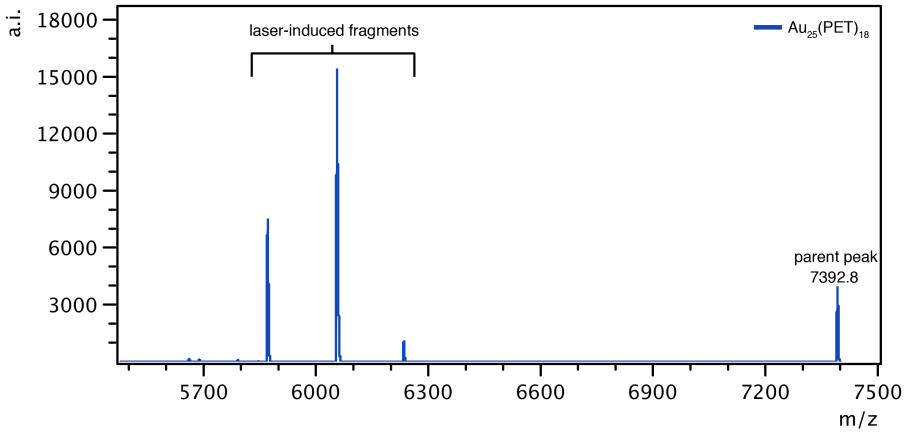

Figure 6. MALDI spectrum of recrystallized $Au_{25}(PET)_{18}$ used to calibrate mass assignment of **1** and **2**. Due to the nature of the instrument, the laser-induced fragmentation could not be avoided and is omnipresent in all Au nanocluster samples we studied.

Purified **1** and **2** were examined by high angle annular dark field scanning transmission electron microscopy (HAADF-STEM). $Au_{25}(SR)_{18}$ single-crystals were also dissolved, drop-cast and imaged as a control. HAADF-STEM gives contrast proportional to atomic number, thus small gold clusters are more easily distinguishable on the carbon support film compared to conventional TEM[32] (see Experimental Methods for details). In addition, this so-called "Z-contrast" can in practice be used to quantify the number of atoms in a cluster. In conventional TEM it is difficult to distinguish gold clusters with fewer than ~50 atoms from the continuous carbon support.[33]

Carbon coated TEM grids were glow-discharged under a toluene atmosphere. This grid treatment appeared to reduce otherwise problematic aggregation of particles on the grid. HAADF-STEM images were acquired as described in the SI. Processing of the data was done by a researcher who was blinded to the identity of the sample. We measured both diameters and integrated intensities for all three samples.

Measurement of the diameters of **1**, $Au_{25}(SR)_{18}$, and **2** reveal average diameters of 1.33 ± 0.07 (99.9% t-test confidence interval, n=305), 1.50±0.09 (99.9% confidence interval, n=200) and 1.66±0.1 (99.9% confidence interval, n=250) respectively. We applied a t-test to determine if these diameters have statistically significant differences. The $t_{calculated}$ values of 8.7, 4.2, and 3.6, for comparison of **1** to **2**, **1** to $Au_{25}(SR)_{18}$, and **2** to $Au_{25}(SR)_{18}$ are all substantially larger than the t_{table} value of 1.980 for a 95% confidence interval. In statistical convention, **1**, **2** and $Au_{25}(SR)_{18}$ diameters are significantly different as determined by analysis of HAADF-STEM micrographs.

Because the measured diameters are larger than expected, with values of 1.3, 1.5 and 1.7 nm compared to calculated diameter values of 0.91, 0.99 and 1.15 nm, we suspected that the particles may both be damaged by the TEM beam and interacting with the carbon film in a way 'flattens' particles that were approximately spherical prior to deposition on a grid and exposure to an electron beam.

To address this, we used the 'Z-contrast' encoded in each HAADF-STEM micrograph. We integrated the pixel intensity over the area of each measured cluster in a micrograph. From this integrated pixel intensity we subtracted the integrated pixel intensity from an equal area of neighboring carbon support (Figure 7 gives example). This blank correction was done for each particle because STEM-based carbon contamination of the grid resulted in a background intensity gradient across each micrograph.

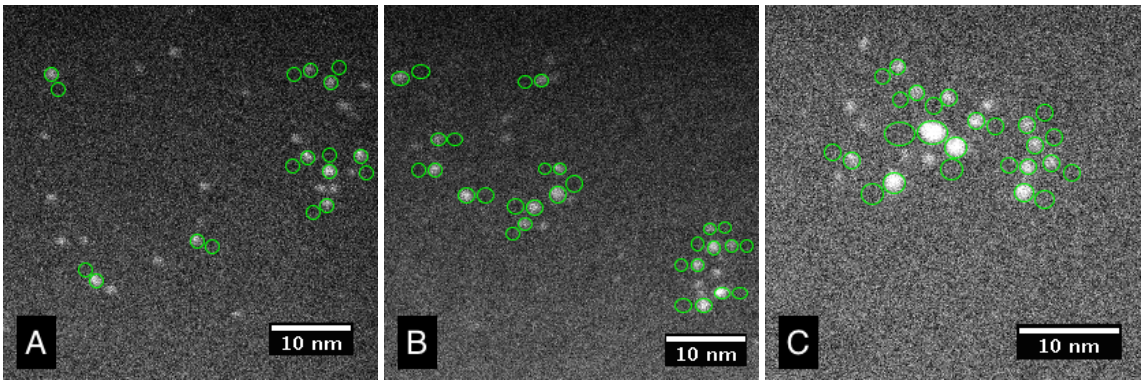

Figure 7. Example HAADF-STEM micrograph used to measure particle sizes for (A) **1**, (B) $Au_{25}(PET)_{18}$, and (C) **2**. Green circles represent area measured on each particle; each particle has a neighboring background measurement of the same area that was subtracted from the particle measurement.

To generate an approximate value for the number of atoms in each cluster, we normalized the pixel intensity per gold atom for the $Au_{25}(SR)_{18}$ control sample. Applying this normalized pixel intensity per atom to the experimental samples gives values of 19.3 ± 2.1 atoms (99.9% t-test confidence interval, n=204) for the monomer sample and 39.0 ± 2.6 atoms (99.9% t-test confidence interval, n=141) for the dimer, in close agreement with the expected values of 20 and 40. Histograms of the associated particle diameters are shown in Figures 8 and 9. A t-test to determine if the distributions are significantly different gives $t_{calculated}$ values of 5.3, 12 and 7.5 for comparison of **1** to $Au_{25}(SR)_{18}$, **1** to **2**, and **2** to $Au_{25}(SR)_{18}$ for n=204, 137, 141 respectively. This $t_{calculated}$ value is greater than the 95% confidence interval t_{table} value of 1.970, so the samples are judged as different in a statistically significant manner.

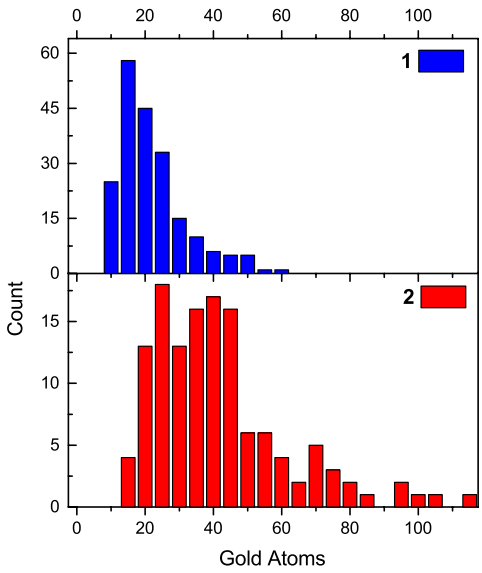

Figure 8. Approximate atom count histograms correlating to integrated pixel intensities from HAADF-STEM examination of **1** (top panel) and **2** (bottom panel).

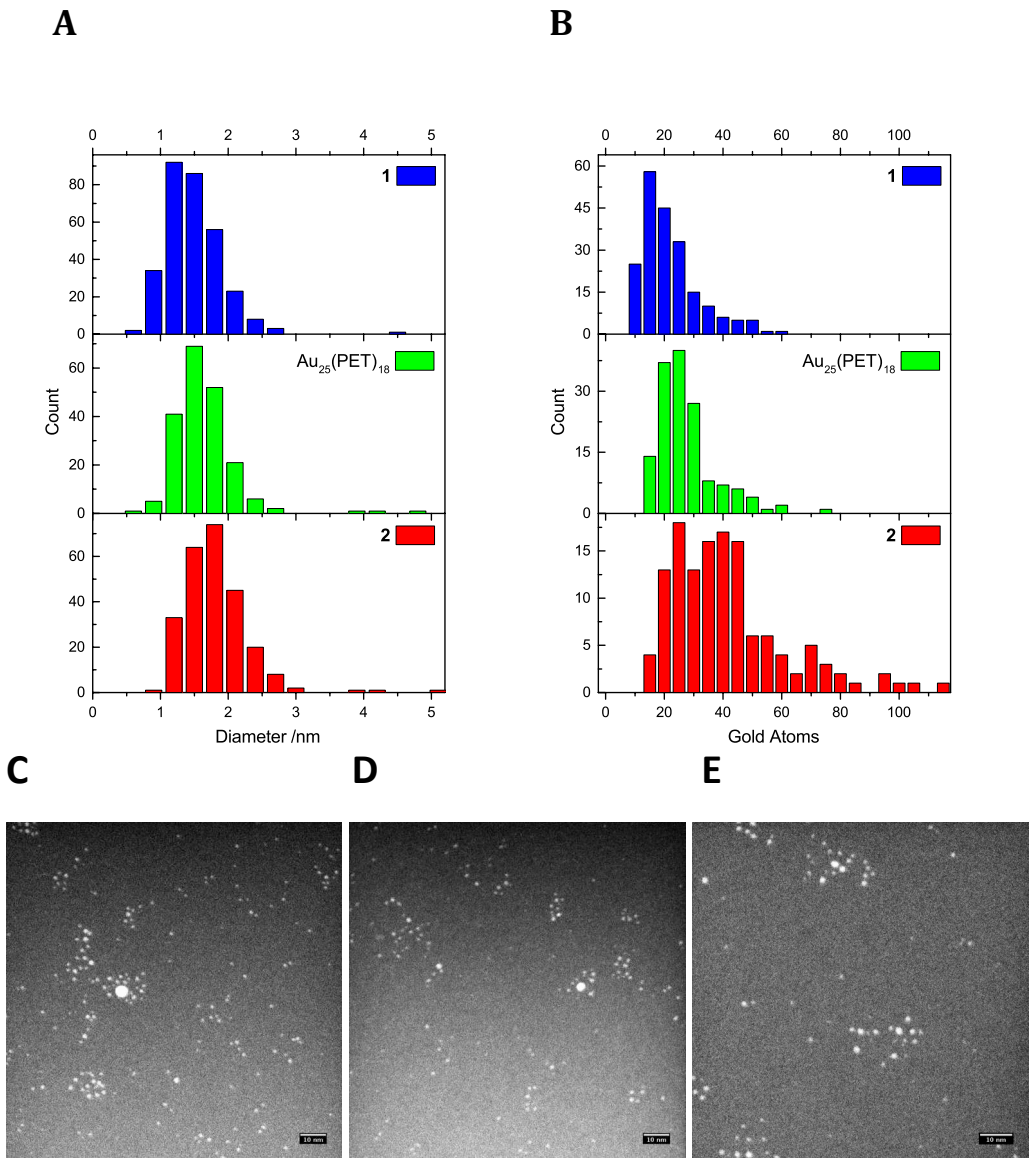

Figure 9. A) Histogram of particle size, B) histogram of gold atoms, example micrographs of C) **1**, D) $Au_{25}(PET)_{18}$, and E) **2**.

Taken together, SEC and TEM suggest that **1** and **2** differ significantly in size, while MALDI-MS suggests that each compound is of identical mass. Since the harsh ionization technique of MALDI may break weak aggregates, *we proceeded under the hypothesis that **1** and **2** represent a monomer and (weakly bound) dimer, respectively.* Because the phenomenon is only observed when synthesis is executed in a diglyme cosolvent, this

working hypothesis incorporates diglyme as a criticial component that induces dimerization.

Under the dimerization hypothesis, recent work by Pettersson suggests that the FTIR spectra of monomer and dimer may differ. Specifically, the work of Pettersson shows that $Au_{144}(PET)_{60}$ in a semi-crystalline state exhibits strong ligand-layer vibrational coupling among neighboring clusters, evidenced by increase in intensity of a set of vibrations.[34] In particular, the crystalline product exhibits three peaks between 1750 and 2000 cm^{-1}. We observe similar emergent features in the same region for **2** that are absent in **1** (Figure 10). Under the dimerization hypothesis, these additional vibrations in **2** are attributed to the proximity of ligands in the dimer. Also consistent with the diglyme hypothesis is a vibration at *ca.* 1125 cm^{-1} for **2** which is consistent with to the ether stretch-mode of diglyme.[35]

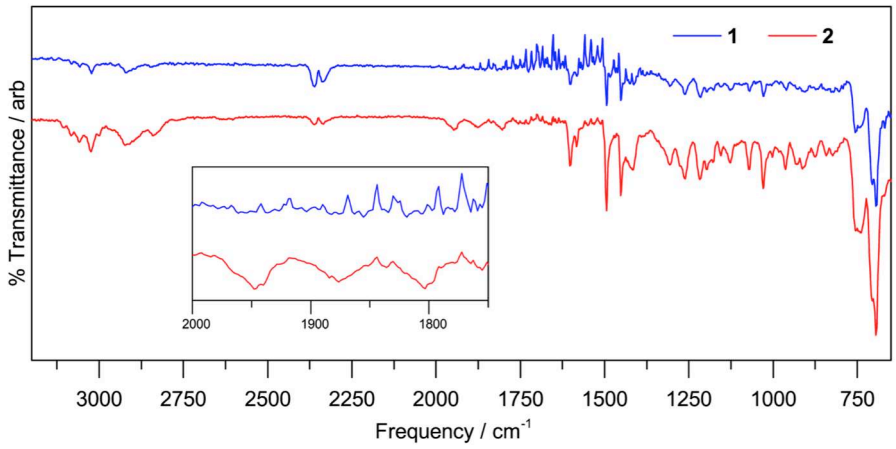

Figure 10. IR spectra of solid **1** and **2**, where **2** is offset for clarity. Spectra appear identical with the exception of the set of peaks at 1750 – 2000 cm^{-1} present in **2** and absent in **1** (inset), which correspond to the forced ligand-ligand interactions caused by dimerization.

Under the dimerization hypothesis, the monomer and dimer are in equilibrium. Thus, the decay of **2** into **1** as well as assembly of **1** into **2** may be measured to establish an equilibrium constant. Differences in the optical spectra of **1** and **2** enable assignment of the relative fraction of each in a mixture. Figure 11A shows the measured spectra for each product (full spectra in Figure S38). The unique peak for **2** at 484 nm enables quantitative determination of relative concentration of **1** and **2** through Beer's law, using the empirically determined extinction coefficients of $\varepsilon_{484,\mathbf{1}}$=2,583 $M^{-1}cm^{-1}$ and $\varepsilon_{484,\mathbf{2}}$=15,347 $M^{-1}cm^{-1}$ (see Experimental Methods for more details).

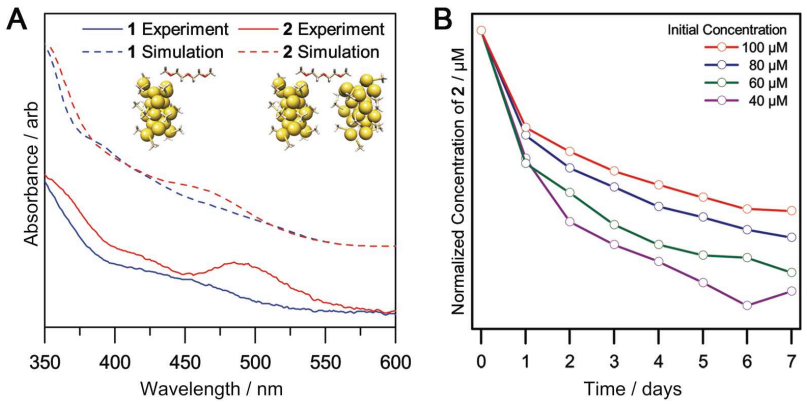

Figure 11. The optical spectra of **1** and **2** allow monitoring of their interconversion. Panel **A** shows linear absorption of **1** and **2** as both measured and calculated for a monomer-dimer model. Relaxed structures of **1** and **2** used to calculate theoretical spectra are shown below the legend. Panel **B** shows first order decay of an isolated dimer into monomer, starting at different concentrations. The concentration dependence of the decay suggests an equilibrium between the reactant and product.

Solutions of isolated **2** at various concentrations were allowed to equilibrate in sealed vessels with periodic monitoring. Figure 11b shows the decreasing concentration of **2** due to dissociation into **1** as equilibrium is approached. From this data we determined a dissociation constant (K_d) of 20.4 ± 1.88 μM when starting from **2**, by kinetic analysis in COPASI.[36] A dissociation constant of this magnitude is on the order of a typically weak

biological interaction. The raw data used to generate the isotherms shown in Figure 11b is given in Figure 12. We also include data showing, with linear optical spectra, the assembly of **1** into **2** in Figure 12.

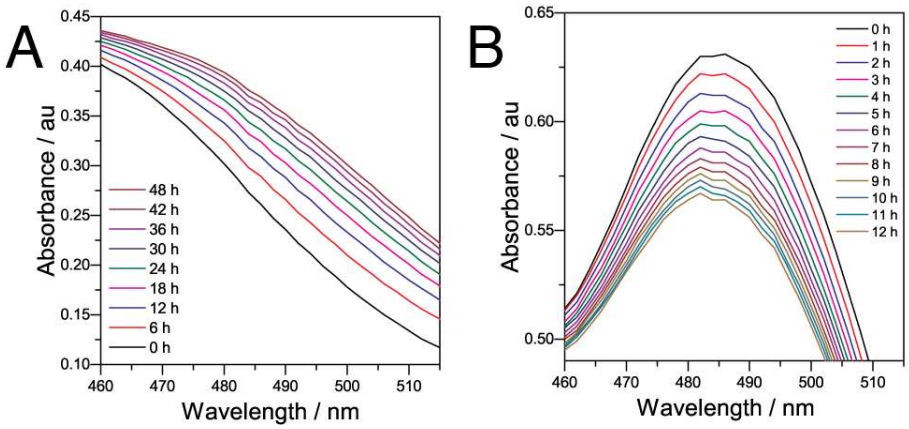

Figure 12. Monitoring the decay of (A) **1** into **2** and (B) **2** into **1**. The pure samples equilibrated at room temperature under continuous UV-Vis monitoring.

Under the dimerization hypothesis**,** **1** and **2** may display different behaviors in differential scanning calorimetry (DSC); specifically, the breaking of a dimer may be observable as a thermal event. To test this **1** and **2** were analyzed by DSC. Both products exhibit an exotherm at approximately 230 °C which we assign as thermal degradation of the cluster (Figure 13). We attribute the differences in the temperature at which the high temperature exotherm appears to experimental variation. For instance, we did not control for oxidation state or air exposure in this experiment. Previously we observed that a single electron oxidation event influences the temperature at which $Au_{25}(SC_6H_{13})_{18}^{-1}$ substantially, with degradation peaks observed by DSC in the range of 205°C to 230°C.[37]

Notably, however, **2** exhibits an exotherm at 170 °C that is not present in the trace of **1**. We attribute this additional peak to dissociation of the dimer caused by sufficient

thermal energy. The subsequent endotherm at 180 °C, which is near the boiling point of diglyme, could represent the desorption of diglyme for both **1** and **2**, and the remaining clusters degrade at *ca.* 230 °C.

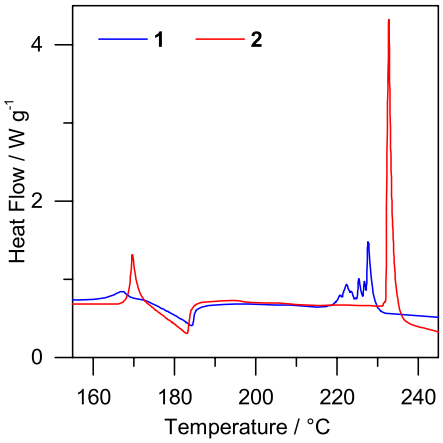

Figure 13. DSC traces of **1** and **2**. 1.500 mg of **1** and **2** were heated at a ramp of 10 ºC/min with N_2 flow rate of 90 mL/min. The exotherm evident in **2** at 170 ºC corresponds to the dimer breaking. Both **1** and **2** then behave similarly after the dimer is broken, exhibiting diglyme loss at 185 ºC and subsequent cluster degradation *ca*. 220 – 235 ºC.

Thermal gravimetric analysis (TGA) reveals 36.4% organic fraction for **2**, compared to an expected organic fraction of 35.0% under the dimerization hypothesis (Figure 14). This is consistent with the formula $Au_{20}(PET)_{15}$-dg-$Au_{20}(PET)_{15}$. The alternative hypothesis of a single 0.95 nm Stokes-Einstein radius cluster, consistent with the SEC measurements, theoretically produces a mass loss of 29.8%.

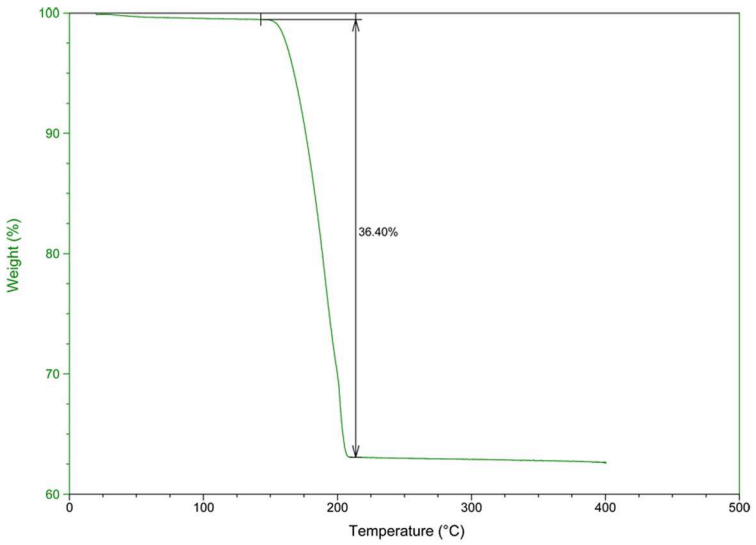

Figure 14. Thermogravimetric analysis on **2**, (Au20(PET)15)2dg. 1.558 mg of sample was heated at a ramp of 10 ºC/min with N2 flow rate of 55 mL/min. Mass loss percent corresponds closely to percent of organic matter in the formula (Au20(PET)15)2dg (actual loss 36.4%, expected loss 34.0%), which is roughly equivalent to the percent of organic matter in **1**.

The plausibility of the diglyme-induced dimerization hypothesis was further investigated through density functional theory (DFT). For DFT modeling we considered the previously published theoretical structure of $Au_{20}(SR)_{16}$[38] and replaced a single –SR ligand with a diglyme and the rest of –SR by –SMe (Me = methyl). A relaxed structure of such $(Au_{20}(SMe)_{15})_2$dg is shown as inset to Figure 11. In the relaxed structure, the terminal methoxy groups of diglyme interact weakly *via* oxygen lone pair orbitals with gold atoms that are part of extended, protecting MeS-Au-Au-SMe units of each cluster. These two gold atoms in the units are proximal to the methoxy oxygen and have a typical metal-metal distance of 2.64 Å. The diglyme-mediated binding of the clusters is close to thermoneutral but very slightly endothermic by 0.07 eV (6.8 kJ/mol). However, this estimate does not take into account the solvent effects, which we understand are primarily responsible for the formation and stability of **1**. While the electronic structure of a single $Au_{20}(SMe)_{15}$dg

cluster shows a zero-spin ground state configuration stabilized by a large HOMO-LUMO gap, the calculations surprisingly predict a spin-triplet ground state for $(Au_{20}(SMe)_{15})_2dg$. The twice-degenerate HOMO orbital of the dimer is delocalized over the large part of the system including the carbon-oxygen backbone of the linker (Figure 15). Computed optical spectra of $Au_{20}(SR)_{15}dg$ monomer and $(Au_{20}(SMe)_{15})_2dg$ dimer are rather similar except for a distinct broad peak for the dimer at around 470 nm, which is in excellent agreement (a difference of only 0.08 eV) to the observed peak at 484 nm for **2** that is lacking for **1** (Figure 11a). The low-energy peak at 470 nm in the computed spectra of the model structure for compound **2** arises from the intercluster interaction mediated by the linker, which gives qualitative support for the hypothesized linking mechanism. Because we do not yet have empirical data on the exact atomic structure of this compound, the qualitative agreement between the experimental and theoretical spectra is remarkable.

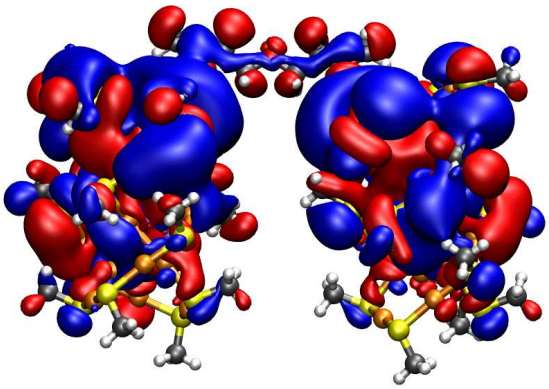

Figure 15. Combined orbital contours of the twice-degenerate HOMO of the computed diglyme-linked $Au_{20}(SMe)_{15}$ dimer.

The theoretical prediction for the dimerization hypothesis of a zero-spin multiplicity for **1** and triplet-spin multiplicity for **2** was interrogated through femtosecond time-

resolved transient absorption pump-probe measurements to compare the electronic relaxation dynamics of **1** and **2.** Consistent with both linear absorption and theoretical calculations (Figure 11a), the differential absorption spectrum of **2**, resulting from 400-nm excitation, showed a prominent transient bleach centered at 484 nm and broad excited-state absorption (ESA) at longer wavelengths (Figure 16a). In contrast, the transient difference spectrum of **1** consisted only of broad ESA; the transient bleach at 484 nm was specific to **2**.

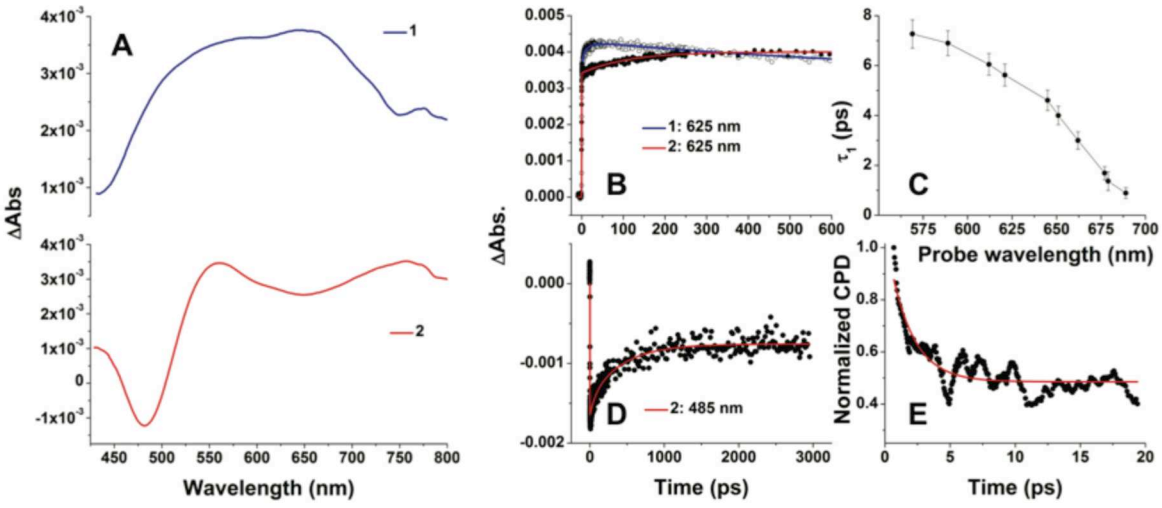

Figure 16. Femtosecond transient absorption pump-probe results for 1 and 2 dispersed in tetrahydrofuran following 400-nm excitation (800 nJ/pulse). (a) Transient absorption spectra of 1 (blue) and 2 (red) recorded at 1-ps pump-probe time delay. Species 2 exhibited a prominent transient bleach at 485 nm. (b) Comparison of time-dependent differential amplitude at 625-nm probe wavelength for 1 (blue) and 2 (red). Species 2 included an approximately 100 ps transient absorption growth not detected for species 1. (c) Summary of electronic relaxation time constants for species 1 plotted versus probe wavelength. (d) Bleach recovery kinetics monitored at 485 nm for species 2. (e) Normalized difference between co- and counter-circularly polarized transient absorption signal (black) monitored at 485 nm plotted versus pump-probe time delay along with the fit result for a first-order exponential decay. The fit yielded a 1.56 ± 0.24 ps time constant, which was attributed to a spin-flip-relaxation process.

The electronic relaxation dynamics (Figure 16b) of **1** were fit using two components: (i) a first-order picosecond ESA growth and (ii) a non-decaying plateau that persisted for the three nanosecond dynamic range of the transient absorption measurement. The ESA growth component exhibited a probe wavelength dependence that was consistent with internal electron thermalization processes (Figure 16c, blue trace). In contrast to **1**, species **2** exhibited multiple relaxation components. Figure 16d portrays the relaxation dynamics obtained by monitoring the amplitude of the differential response at 485 nm for **2** following excitation by linearly polarized 400-nm light. The transient bleach was fit to a recovery time constant of 260 ± 50 ps; a non-decaying plateau function was also included to accurately fit the data. Monitoring the electronic relaxation dynamics of **2** at 625-nm probe wavelength (Figure 16b, red trace) revealed an approximately 100 picosecond ESA growth; these time domain data were clearly different from those obtained from **1** at the same probe wavelength (Figure 16b, blue trace).

In order to examine whether the dramatic differences in electronic energy relaxation of **1** and **2** originated from the theoretically predicted high-spin configuration of **2**, we studied both nanocluster species using co- and counter-circularly polarized pump and probe laser pulses, which is an established method for isolating spin-dependent dynamics.[39] The difference between co- and counter-circularly-polarized transient absorption data monitored at 484 nm for **2** is shown in Figure 16e. These data revealed a spin-dependent relaxation process with a decay time constant of 1.56 ± 0.24 ps, which was not detected for **1**. This relaxation process, which was observable only by using appropriate laser pulse polarizations, is attributed to a spin-flip mechanism that is unique to the high-spin dimer species. Taken together, the distinguishable transient difference

spectra, along with the electronic and spin-dependent relaxation dynamics of **2** confirm the experimental and theoretical aspects of the model.

Overall, we considered three hypotheses to account for the observed dynamic behavior. Of these hypotheses, a dimerization hypothesis appears to be the best fit for the data. Under this hypothesis, the synthetic cosolvent diglyme in which these AuNCs are synthesized substitutes for a thiolate ligand in the ligand shell. In this model developed under this hypothesis, the terminal methoxy group coordinates to the Au surface. We propose that **1** is structurally similar to $Au_{20}(PET)_{16}$ except that a molecule of diglyme substitutes for a single thiolate ligand. This Au-O interaction with the AuNC surface is driven by the large molar excess of diglyme as the synthetic solvent. Without the large molar excess of diglyme (*i.e.* 3:1 diglyme:THF solvent systems), these assemblies do not form. Overall, the evidence suggests that diglyme substitutes for a single thiolate ligand. We cannot rule out THF playing a role in similar ligation of the cluster, but the model we propose adequately accounts for our data without invoking the complication of THF ligation.

Initial association among clusters may be driven in part by poor solvation of clusters by diglyme, resulting in clusters of nanoparticles,[40] consistent with our observation that nanoparticles are insoluble in neat diglyme. Within the aggregates of clusters diglyme can become a crosslinker. In this case, two species of **1** bind to the terminal ends of diglyme to form **2**, losing a molecule of diglyme in the process. The resulting dimer would have the formula $Au_{20}(PET)_{15}$-dg-$Au_{20}(PET)_{15}$. The Au-O bond between the cluster cores and diglyme is weak, allowing spontaneous dissociation of **2** into **1**. Under the dimerization hypothesis, the mass spectrum of **1** and **2** appear identical because the weak interaction of

diglyme-induced dimerization in **2** does not survive the ionization in MALDI. We do not expect to observe free diglyme in the spectra because it is smaller than the mass range studied during the experiment (4,000 – 15,000 Da).

We expect that we do not observe discrete dimers in TEM because of electron beam induced sintering of neighboring particles in this high electron flux method. Such dynamic instability of small metal clusters under an electron beam is well documented.[41-44] Likewise, we observe many larger aggregates, which we attribute to clusters-of-clusters forming during solvent evaporation, followed by beam-induced sintering. In Figure 8, bottom panel, the sample assigned as the dimer appears to have some component of monomer. In this TEM experiment, we are attempting to correlate the observation of a drop cast, desolvated sample to its solvated, solution state. The act of drying a sample on the grid may influence its overall aggregation state.

We considered that the products could be formed by interaction with the silica gel column, but dismissed this possibility by showing that purified **1** and **2** are both stable to subsequent analysis on silica based thin-layer chromatography (Figure 17).

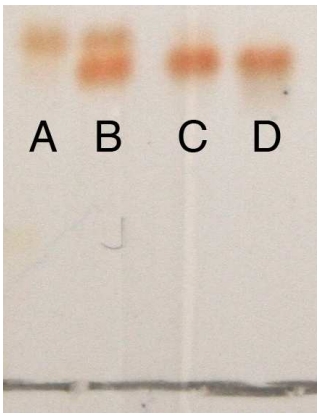

Figure 17. An example thin layer chromatography (TLC) plate of **1** and **2** as fractions eluting from a silica gel column. From left to right, fraction (a) is pure **1**, (b) is a mixture of **1** and **2**, (c) is pure **2**, and (d) is **2** with some apparent byproduct. These fractions show that the materials remain pure after elution from the column and that the material does not undergo any chemistry while moving through the stationary phase of the column.

The most similar $Au_x(SR)_y$ cluster to the $Au_{20}(SR)_{15}$ of the present report is $Au_{20}(SR)_{16}$ reported by Jin[45] and modeled by Zeng.[38] $Au_{20}(PET)_{15}$ is apparently missing a single thiol ligand from the known $Au_{20}(SR)_{16}$. In other mass spectrometry experiments (Figure 18) on $Au_x(SR)_y$ nanoclusters synthesized in diglyme in slightly different conditions, we observe x/y=24/17 and x/y=28/19, which are also one-ligand deletions of the previously reported clusters x/y=24/18 and x/y=28/20.[46,47]

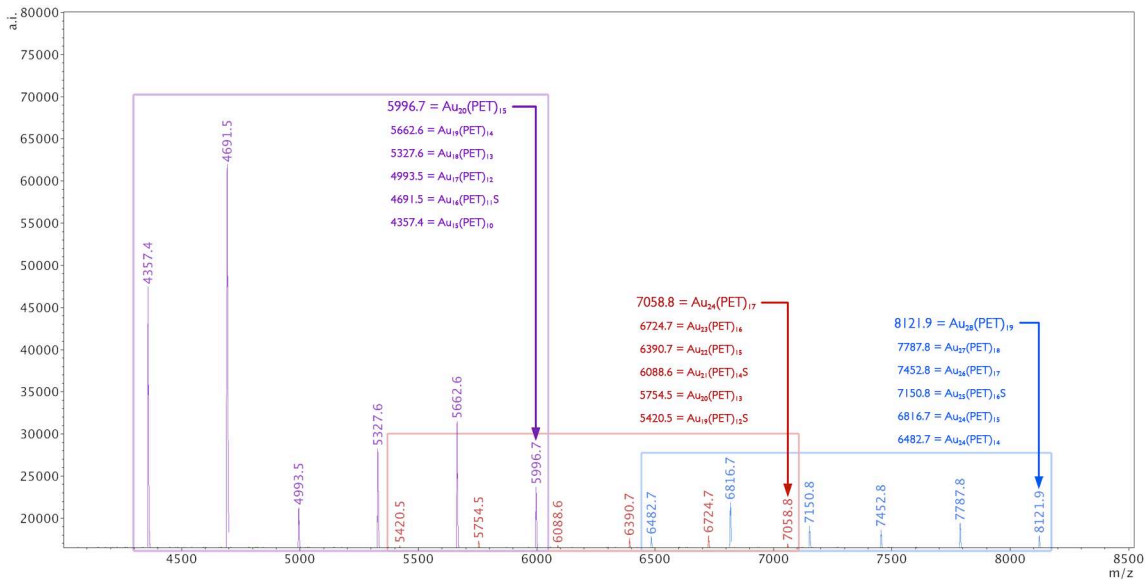

Figure 18. Simplified (low intensity signals removed) MALDI spectrum of crude Au@PET synthesized in the presence of diglyme that highlights three parent peaks corresponding to $Au_{20}(PET)_{15}$, $Au_{24}(PET)_{17}$, and $Au_{28}(PET)_{19}$. Fragmentation patterns of roughly –Au(SR) are color coded to match their parent peak, and their corresponding $Au_x(SR)_y$ is listed with the mass of each fragment.

5.5 Conclusions

In conclusion, we report the assembly of diglyme-mediated dynamic assemblies of AuNCs. Notably, in previous work examining a large set of solvent conditions, we do not observe solvent based assembly except when diglyme is present.[25] While we explored the assembly, dynamics, theory and spectroscopy of **1** and **2** in the present work, the diglyme-mediated assembly into dynamic structures may be a general property of gold nanoparticles Our work opens the avenue to investigate further the dynamic and environmentally responsive nature of these assemblies, control over interparticle spacing, the generality of the electron sharing among neighboring nanoparticles. Applications in sensing may follow from these fundamental properties.

REFERENCES

1. Turkevich, J.; Stevenson, P. S.; Hillier, J. A Study of the Nucleation and Growth Processes in the Synthesis of Colloidal Gold. *Disc. Faraday Soc.* **1951**, *11*, 55–75.

2. Daniel, M.-C.; Astruc, D. Gold Nanoparticles: Assembly, Supramolecular Chemistry, Quantum-Size-Related Properties, and Applications Toward Biology, Catalysis, and Nanotechnology. *Chem. Rev.* **2004**, *104*, 293–346.

3. Leff, D. V.; Brandt, L.; Heath, J. R. Synthesis and Characterization of Hydrophobic, Organically-Soluble Gold Nanocrystals Functionalized with Primary Amines. *Langmuir* **1996**, *12*, 4723–4730.

4. Gomez, S.; Philippot, K.; Collière, V.; Chaudret, B.; Senocq, F.; Lecante, P. Gold Nanoparticles From Self-Assembled Gold(I) Amine Precursors. *Chem. Commun.* **2000**, 1945–1946.

5. Bellon, P.; Manassero, M.; Sansoni, M. Crystal and Molecular Structure of Tri-iodoheptakis(Tri-Para-Fluorophenyl-Phosphine) Undecagold. *J. Chem. Soc., Dalton Trans.* **1972**, 1481–1487.

6. Brust, M.; Walker, M.; Bethell, D.; Schiffrin, D.; Whyman, R. Synthesis of Thiol-Derivatized Gold Nanoparticles in a Two-Phase Liquid-Liquid System. *J. Chem. Soc., Chem. Commun.* **1994**, 801–802.

7. Mingos, D. Gold - a Flexible Friend in Cluster Chemistry. *J. Chem. Soc., Dalton Trans.* **1996**, 561–566.

8. Hutchings, G. J.; Brust, M.; Schmidbaur, H. Gold - an Introductory Perspective. *Chem. Soc. Rev.* **2008**, *37*, 1759–1765.

9. Chen, J.; Zhang, Q.-F.; Bonaccorso, T. A.; Williard, P. G.; Wang, L.-S. Controlling Gold Nanoclusters by Diphospine Ligands. *J. Am. Chem. Soc.* **2014**, *136*, 92–95.

10. Mirkin, C.; Letsinger, R.; Mucic, R.; Storhoff, J. A DNA-Based Method for Rationally Assembling Nanoparticles Into Macroscopic Materials. *Nature* **1996**, *382*, 607–609.

11. Brousseau, L. C., III; Novak, J. P.; Marinakos, S. M.; Feldheim, D. L. Assembly of Phenylacetylene-Bridged Gold Nanocluster Dimers and Trimers. *Adv. Mater.* **1999**, *11*, 447–449.

12. Blum, A.; Soto, C.; Wilson, C.; Cole, J.; Kim, M.; Gnade, B.; Chatterji, A.; Ochoa, W.; Lin, T.; Johnson, J.; Ratna, B. Cowpea Mosaic Virus as a Scaffold for 3-D Patterning of Gold Nanoparticles. *Nano Lett.* **2004**, *4*, 867–870.

13. Ackerson, C. J.; Jadzinsky, P. D.; Jensen, G. J.; Kornberg, R. D. Rigid, Specific, and Discrete Gold Nanoparticle/Antibody Conjugates. *J. Am. Chem. Soc.* **2006**, *128*, 2635–2640.

14. Zanchet, D.; Micheel, C.; Parak, W.; Gerion, D.; Williams, S.; Alivisatos, A. Electrophoretic and Structural Studies of DNA-Directed Au Nanoparticle Groupings. *J. Phys. Chem. B* **2002**, *106*, 11758–11763.

15. Park, S. Y.; Lytton-Jean, A. K. R.; Lee, B.; Weigand, S.; Schatz, G. C.; Mirkin, C. A. DNA-Programmable Nanoparticle Crystallization. *Nature* **2008**, *451*, 553–556.

16. Willner, I.; Basnar, B.; Willner, B. Nanoparticle-Enzyme Hybrid Systems for Nanobiotechnology. *FEBS J.* **2007**, *274*, 302–309.

17. Nam, J.-M.; Park, S.-J.; Mirkin, C. Bio-Barcodes Based on Oligonucleotide-Modified Nanoparticles. *J. Am. Chem. Soc.* **2002**, *124*, 3820-3821.

18. Storhoff, J. J.; Lazarides, A. A.; Mucic, R. C.; Mirkin, C. A.; Letsinger, R. L.; Schatz, G. C. What Controls the Optical Properties of DNA-Linked Gold Nanoparticle Assemblies? *J. Am. Chem. Soc.* **2000**, *122*, 4640–4650.

19. Xiao, Y.; Patolsky, F.; Katz, E.; Hainfeld, J. F.; Willner, I. "Plugging Into Enzymes": Nanowiring of Redox Enzymes by a Gold Nanoparticle. *Science* **2003**, *299*, 1877–1881.

20. Aubin-Tam, M.-E.; Hwang, W.; Hamad-Schifferli, K. Site-Directed Nanoparticle Labeling of Cytochrome C. *Proc. Natl. Acad. Sci. USA* **2009**, *106*, 4095–4100.

21. Chou, L. Y. T.; Zagorovsky, K.; Chan, W. C. W. DNA Assembly of Nanoparticle Superstructures for Controlled Biological Delivery and Elimination. *Nat. Nanotechnol.* **2014**, *9*, 148–155.

22. Zanchet, D.; Micheel, C.; Parak, W.; Gerion, D.; Alivisatos, A. Electrophoretic Isolation of Discrete Au Nanocrystal/DNA Conjugates. *Nano Lett.* **2001**, *1*, 32–35.

23. Schreiber, R.; Do, J.; Roller, E.-M.; Zhang, T.; Schüller, V. J.; Nickels, P. C.; Feldmann, J.; Liedl, T. Hierarchical Assembly of Metal Nanoparticles, Quantum Dots and Organic Dyes Using DNA Origami Scaffolds. *Nat. Nanotechnol.* **2014**, *9*, 74–78.

24. Lavenn, C.; Albrieux, F.; Bergeret, G.; Chiriac, R.; Delichère, P.; Tuel, A.; Demessence, A. Functionalized Gold Magic Clusters: $Au_{25}(SPhNH_2)_{17}$. *Nanoscale* **2012**, *4*, 7334–7337.

25. Wong, O. A.; Compel, W. S.; Ackerson, C. J. Combinatorial Discovery of Cosolvent Systems for Production of Narrow Dispersion Thiolate-Protected Gold Nanoparticles. *ACS Comb. Sci.* **2015,** *17*, 11-18.

26. Murray, C. B.; Norris, D. J.; Bawendi, M. G. Synthesis and Characterization of Nearly Monodisperse CdE (E = Sulfur, Selenium, Tellurium) Semiconductor Nanocrystallites. *J. Am. Chem. Soc.* **1993**, *115*, 8706–8715.

27. Knoppe, S.; Boudon, J.; Dolamic, I.; Dass, A.; Bürgi, T. Size Exclusion Chromatography for Semipreparative Scale Separation of $Au_{38}(SR)_{24}$ and $Au_{40}(SR)_{24}$ and Larger Clusters. *Anal. Chem.* **2011**, *83*, 5065–5061.

28. Heaven, M. W.; Dass, A.; White, P. S.; Holt, K. M.; Murray, R. W. Crystal Structure of the Gold Nanoparticle $[N(C_8H_{17})_4]$ $[Au_{25}(SCH_2CH_2Ph)_{18}]$. *J. Am. Chem. Soc.* **2008**, *130*, 3754–3755.

29. Bahena, D.; Bhattarai, N.; Santiago, U.; Tlahuice, A.; Ponce, A.; Bach, S. B. H.; Yoon, B.; Whetten, R. L.; Landman, U.; Jose-Yacaman, M. STEM Electron Diffraction and High-Resolution Images Used in the Determination of the Crystal Structure of the $Au_{144}(SR)_{60}$ Cluster. *J. Phys. Chem. Lett.* **2013**, *4*, 975–981.

30. Dass, A.; Stevenson, A.; Dubay, G. R.; Tracy, J. B.; Murray, R. W. Nanoparticle MALDI-TOF Mass Spectrometry Without Fragmentation: $Au_{25}(SCH_2CH_2Ph)_{18}$ and Mixed Monolayer $Au_{25}(SCH_2CH_2Ph)_{18-X}(L)_X$. *J. Am. Chem. Soc.* **2008**, *130*, 5940–5946.

31. Qian, H.; Zhu, Y.; Jin, R. Size-Focusing Synthesis, Optical and Electrochemical Properties of Monodisperse $Au_{38}(SC_2H_4Ph)_{24}$ Nanoclusters. *ACS Nano* **2009**, *3*, 3795–3803.

32. Menard, L.; Gao, S.; Xu, H.; Twesten, R.; Harper, A.; Song, Y.; Wang, G.; Douglas, A.; Yang, J.; Frenkel, A.; Nuzzo, R.; Murray, R. Sub-Nanometer Au Monolayer-Protected Clusters Exhibiting Molecule-Like Electronic Behavior: Quantitative High-Angle Annular Dark-Field Scanning Transmission Electron Microscopy and Electrochemical Characterization of Clusters with Precise Atomic Stoichiometry. *J. Phys. Chem. B* **2006**, *110*, 12874–12883.

33. Hainfeld, J. F.; Furuya, F. R. A 1.4-Nm Gold Cluster Covalently Attached to Antibodies Improves Immunolabeling. *J. Histochem. Cytochem.* **1992**, *40*, 177–184.

34. Koivisto, J.; Salorinne, K.; Mustalahti, S.; Lahtinen, T.; Malola, S.; Häkkinen, H.; Pettersson, M. Vibrational Perturbations and Ligand–Layer Coupling in a Single Crystal of $Au_{144}(SC_2H_4Ph)_{60}$Nanocluster. *J. Phys. Chem. Lett.* **2014**, *5*, 387–392.

35. Stein, S. E. Infrared Spectra. In *NIST Chemistry WebBook, NIST Standard Reference Database Number 69*; Lindstrom, P. J.; Mallard, W. G., Eds.; National Institute of Standards and Technology: Gaithersburg MD; http://webbook.nist.gov

36. Hoops, S.; Sahle, S.; Gauges, R.; Lee, C.; Pahle, J.; Simus, N.; Singhal, M.; Xu, L.; Mendes, P.; Kummer, U. COPASI--a COmplex PAthway SImulator. *Bioinformatics* **2006**, *22*, 3067–3074.

37. Tofanelli, M. A.; Ackerson, C. J. Superatom Electron Configuration Predicts Thermal Stability of $Au_{25}(SR)_{18}$ Nanoclusters. *J. Am. Chem. Soc.* **2012**, *134*, 16937–16940.

38. Pei, Y.; Gao, Y.; Shao, N.; Zeng, X. C. Thiolate-Protected $Au_{20}(SR)_{16}$ Cluster: Prolate Au_8 Core with New $[Au_3(SR)_4]$ Staple Motif. *J. Am. Chem. Soc.* **2009**, *131*, 13619–13621.

39. Baumberg, J.; Awschalom, D.; Samarth, N.; Luo, H.; Furdyna, J. Spin Beats and Dynamical Magnetization in Quantum Structures. *Phys. Rev. Lett.* **1994**, *72*, 717–720.

40. Yan, H.; Cingarapu, S.; Klabunde, K. J.; Chakrabarti, A.; Sorensen, C. M. Nucleation of Gold Nanoparticle Superclusters From Solution. *Phys. Rev. Lett.* **2009**, *102*, 95501-95504.

41. Bals, S.; Van Aert, S.; Romero, C. P.; Lauwaet, K.; Van Bael, M. J.; Schoeters, B.; Partoens, B.; Yücelen, E.; Lievens, P.; Van Tendeloo, G. Atomic Scale Dynamics of Ultrasmall Germanium Clusters. *Nat. Commun.* **2012**, *3*, 897.

42. Taylor, K. A.; Glaeser, R. M. Retrospective on the Early Development of Cryoelectron Microscopy of Macromolecules and a Prospective on Opportunities for the Future. *J. Struct. Biol.* **2008**, *163*, 214–223.

43. Azubel, M.; Koivisto, J.; Malola, S.; Bushnell, D.; Hura, G. L.; Koh, A. L.; Tsunoyama, H.; Tsukuda, T.; Pettersson, M.; Häkkinen, H.; *et al.* Nanoparticle Imaging. Electron Microscopy of Gold Nanoparticles at Atomic Resolution. *Science* **2014**, *345*, 909–912.

44. Udayabhaskararao, T.; Sun, Y.; Goswami, N.; Pal, S. K.; Balasubramanian, K.; Pradeep, T. Ag_7Au_6: a 13-Atom Alloy Quantum Cluster. *Angew. Chem. Int. Ed. Engl.* **2012**, *51*, 2155–2159.

45. Zhu, M.; Qian, H.; Jin, R. Thiolate-Protected Au_{20}Clusters with a Large Energy Gap of 2.1 eV. *J. Am. Chem. Soc.* **2009**, *131*, 7220–7221.

46. Pei, Y.; Pal, R.; Liu, C.; Gao, Y.; Zhang, Z.; Zeng, X. C. Interlocked Catenane-Like Structure Predicted in $Au_{24}(SR)_{20}$: Implication to Structural Evolution of Thiolated Gold Clusters From Homoleptic Gold(I) Thiolates to Core-Stacked Nanoparticles. *J. Am. Chem. Soc.* **2012**, *134*, 3015–3024.

47. Zeng, C.; Li, T.; Das, A.; Rosi, N. L.; Jin, R. Chiral Structure of Thiolate-Protected 28-Gold-Atom Nanocluster Determined by X-Ray Crystallography. *J. Am. Chem. Soc.* **2013,** *135*, 10011-10013

48. Enkovaara, J.; Rostgaard, C.; Mortensen, J. J.; Chen, J.; Dułak, M.; Ferrighi, L.; Gavnholt, J.; Glinsvad, C.; Haikola, V.; Hansen, H. A.; Kristoffersen, H.; Kuisama, M.; Larsen, A.; Lehtovaara, L.; Ljungberg, M.; Lopez-Acevedo, O.; Moses, P.; Ojanen, J.;

Olsen, T.; Petzold, V.; *et al.* Electronic Structure Calculations with GPAW: a Real-Space Implementation of the Projector Augmented-Wave Method. *J Phys. Condens. Matter.* **2010**, *22*, 253202.

49. Perdew, J.; Burke, K.; Ernzerhof, M. Generalized Gradient Approximation Made Simple. *Phys. Rev. Lett.* **1996**, *77*, 3865–3868.

50. Walter, M.; Häkkinen, H.; Lehtovaara, L.; Puska, M.; Enkovaara, J.; Rostgaard, C.; Mortensen, J. J. Time-Dependent Density-Functional Theory in the Projector Augmented-Wave Method. *J Chem. Phys.* **2008**, *128*, 244101.

51. Dowgiallo, A.-M.; Schwartzberg, A. M.; Knappenberger, K. L. Structure-Dependent Coherent Acoustic Vibrations of Hollow Gold Nanospheres. *Nano. Lett.* **2011**, *11*, 3258–3262.

CHAPTER 6

Summary

The research reported herein details a novel approach for Au cluster total synthesis. Glymes drastically increase the monodispersity of products formed and appear to favor one size for each ligand. Although the exact mechanism is yet to be understood, glyme is observed coordinating to the metal in the metallopolymer precursor and in the final cluster product. All products formed using this approach appear to undergo a surface modification and sacrifice a single thiol ligand in favor of a single molecule of glyme on the cluster surface. This modification results in spontaneous self-assembly with other products that incorporate glyme and potentially allows for single glyme-for-thiol exchange to tailor the cluster properties for specific application. These clusters are metastable and rely on the presence of glyme or another coordinating molecule for stability once removed from their reaction conditions.

SUPPLEMENTAL INFORMATION

Table S1. Table of Solvent Properties

Solvent	Dielectric Constant	Solvent	Dipole Moment	Solvent	Density
Dioxane	2.3	Dioxane	0	iPrOH	0.785
DMM	2.7	DMM	0.74	MeCN	0.786
DME	7.2	iPrOH	1.58	EtOH	0.789
Diglyme	7.3	nPrOH	1.55	MeOH	0.791
THF	7.6	nBuOH	1.66	nPrOH	0.803
nBuOH	17.5	EtOH	1.69	nBuOH	0.81
iPrOH	19.9	MeOH	1.7	DMM	0.86
nPrOH	20.3	THF	1.75	DME	0.868
EtOH	24.6	DME	1.8	THF	0.886
MeOH	32.7	Diglyme	1.97	Diglyme	0.943
DMF	36.7	DMF	3.82	DMF	0.944
MeCN	37.5	MeCN	3.93	Dioxane	1.033
DMSO	46.7	DMSO	3.96	DMSO	1.092

Ref: Lide, D.R. CRC Handbook of Chemistry and Physics 77th Edition; CRC Press: Boca Raton, 1996.

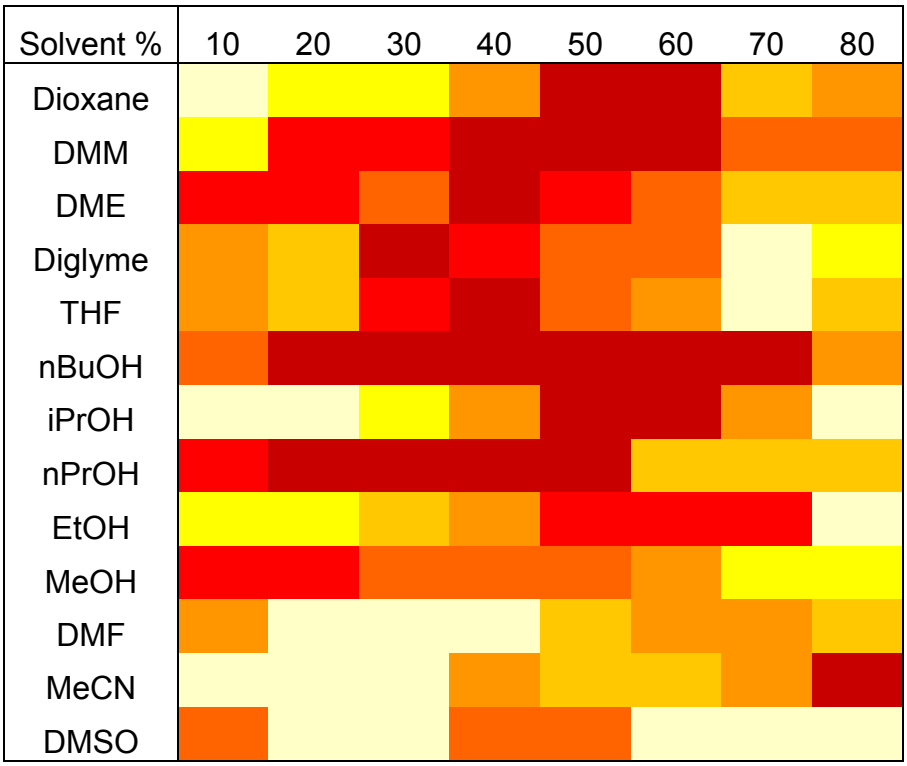

Figure S1. With *p*-mercaptobenzoic acid as the ligand (arranged by dielectric constant)

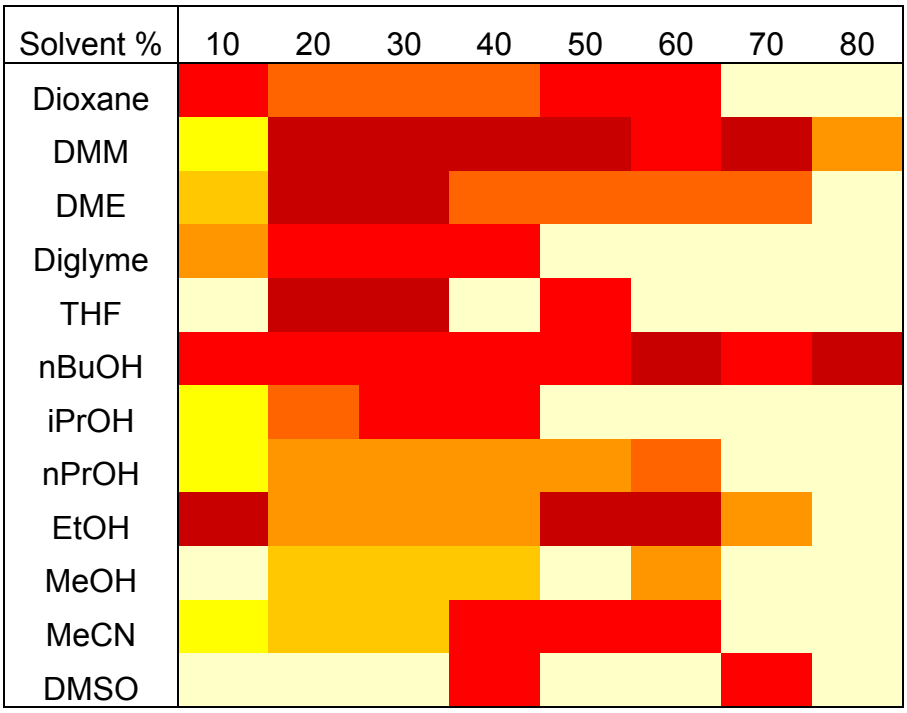

Figure S2. With thiomalic acid as the ligand (arranged by dielectric constant)

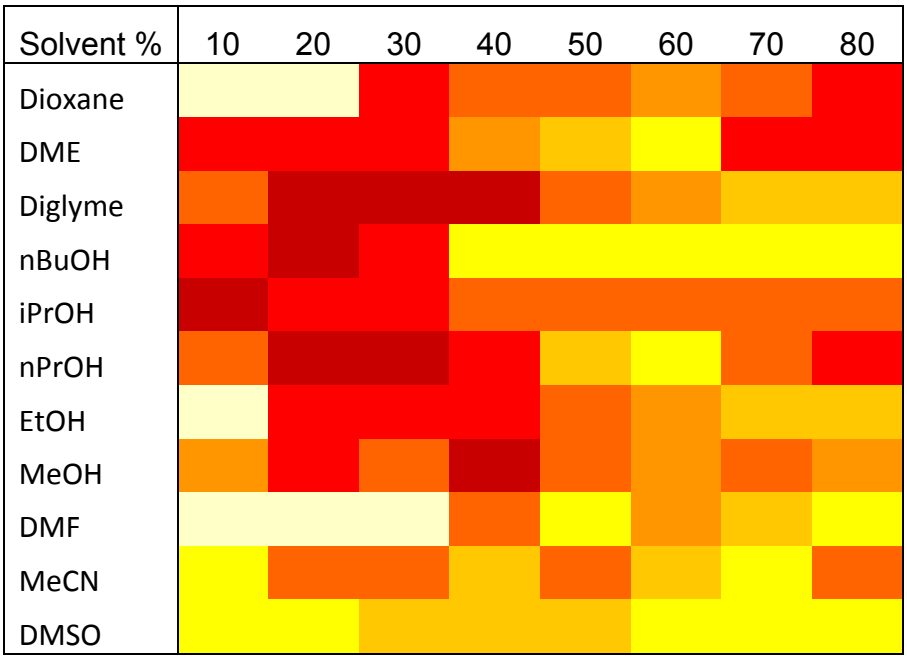

Figure S3. With glutathione as the ligand (arranged by dielectric constant)

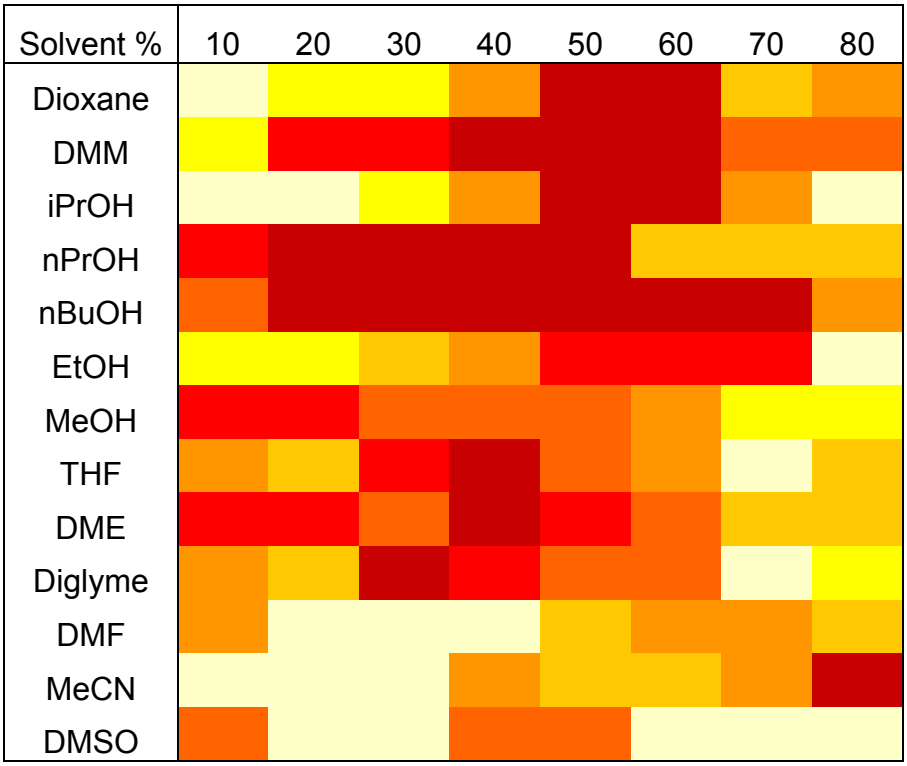

Figure S4. With *p*-mercaptobenzoic acid as the ligand (arranged by dipole moment)

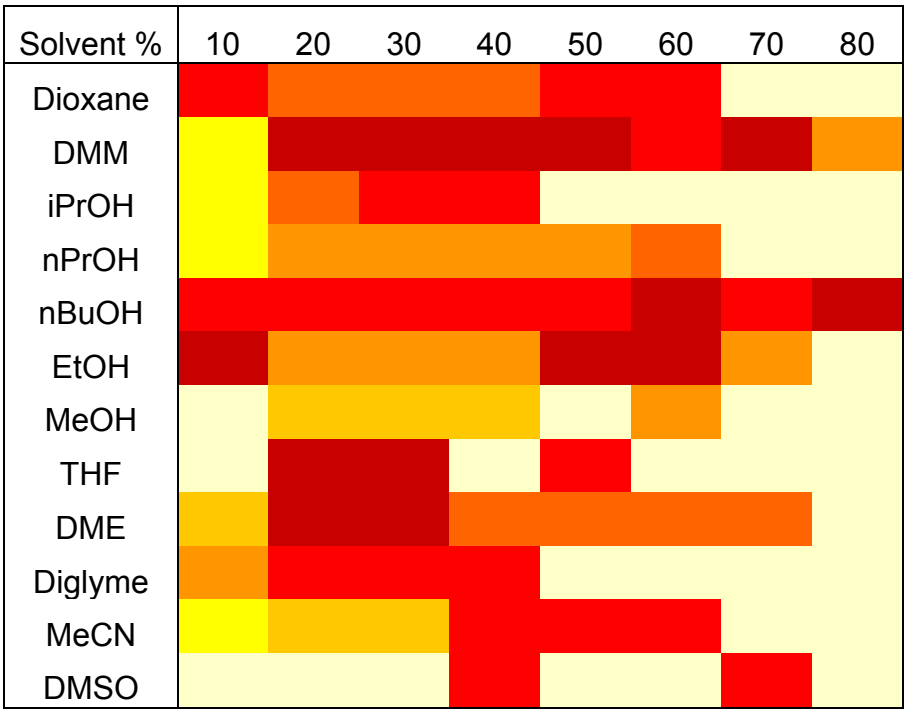

Figure S5. With thiomalic acid as the ligand (arranged by dipole moment)

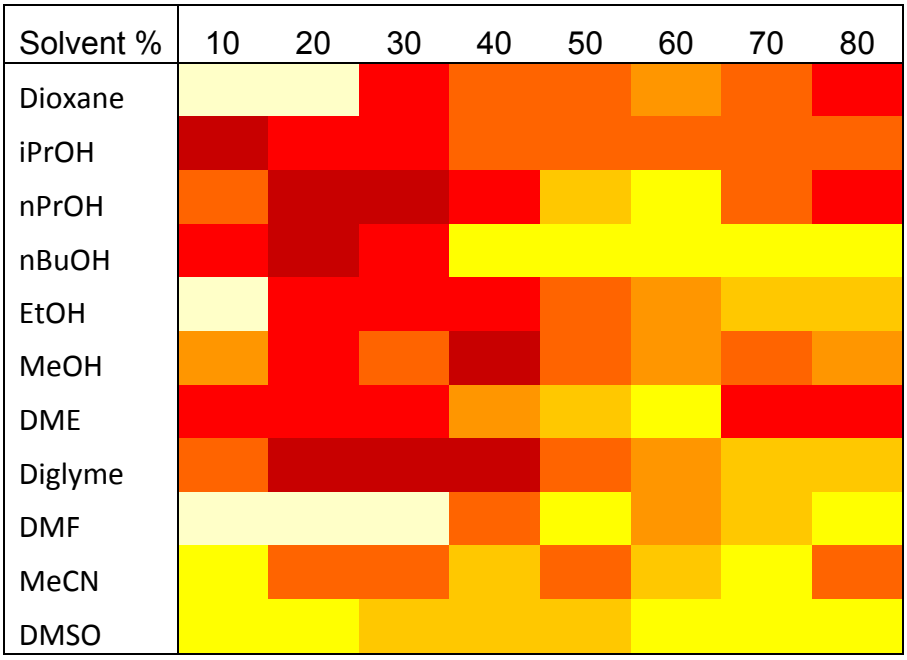

Figure S6. With glutathione as the ligand (arranged by dipole moment)

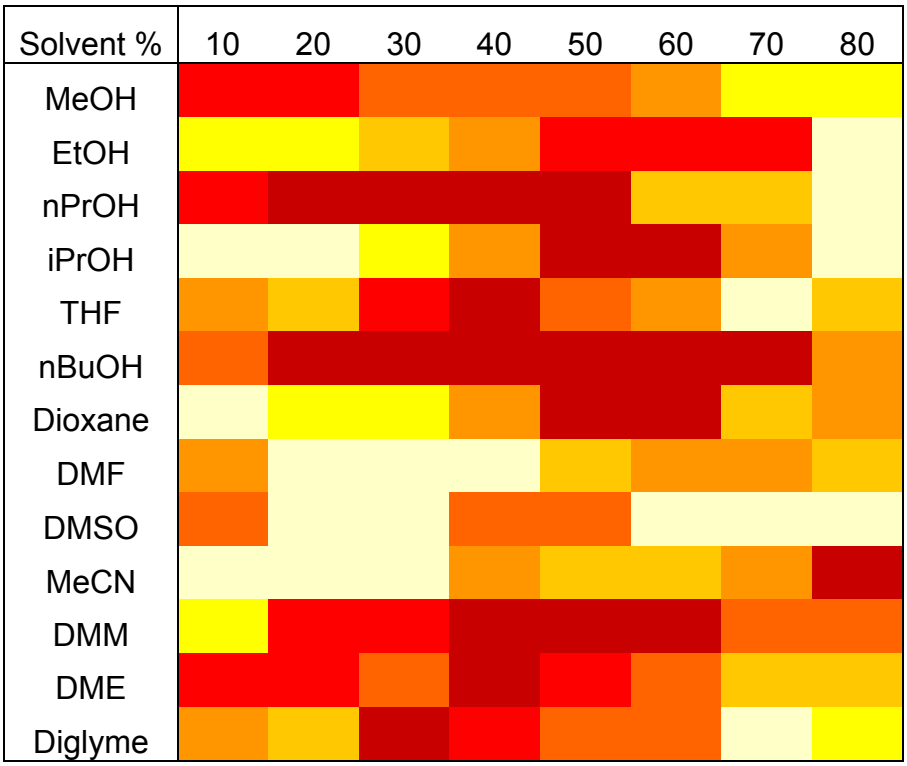

Figure S7. With *p*-mercaptobenzoic acid as the ligand (arranged by chelating ability)

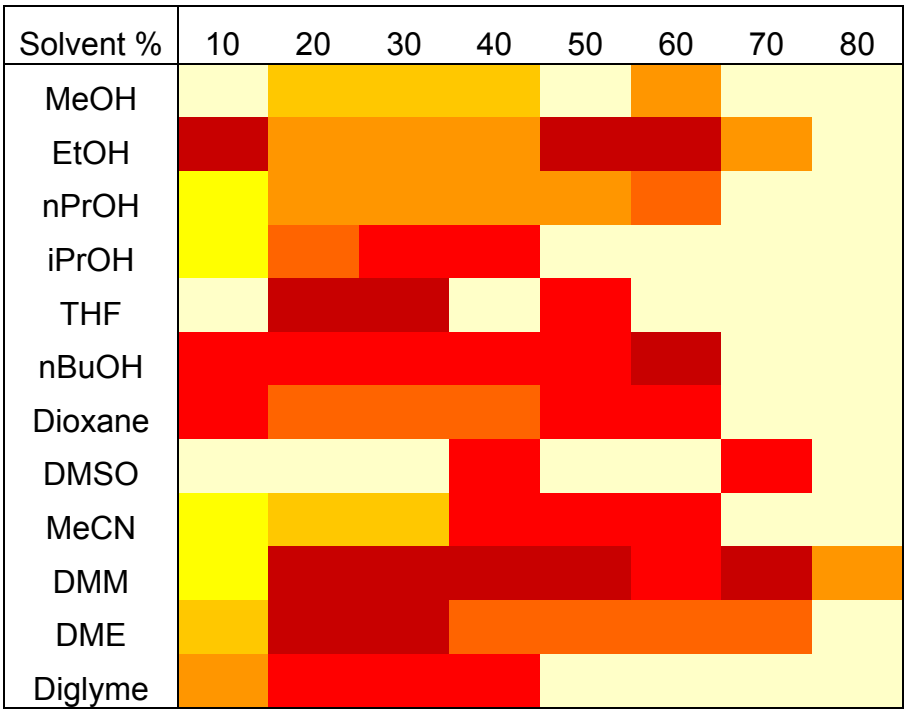

Figure S8. With thiomalic acid as the ligand (arranged by chelating ability)

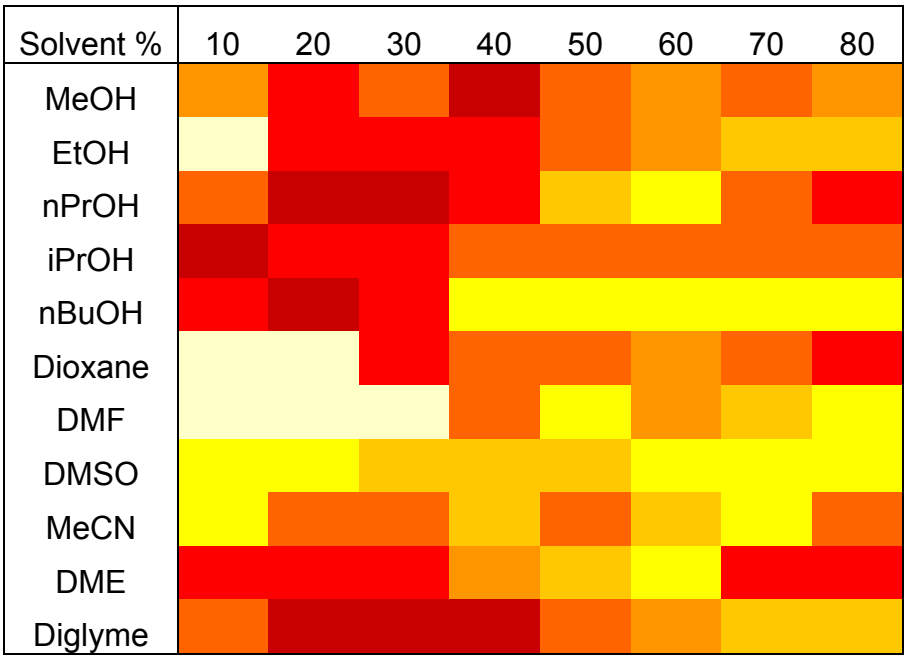

Figure S9. With glutathione as the ligand (arranged by chelating ability)

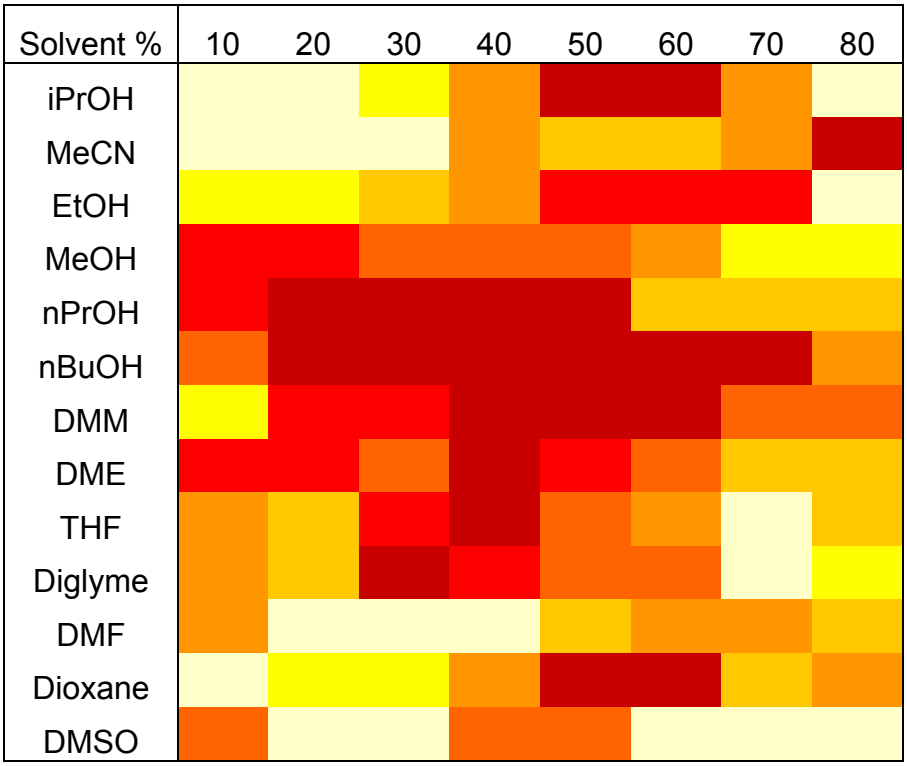

Figure S10. With *p*-mercaptobenzoic acid as the ligand (arranged by density)

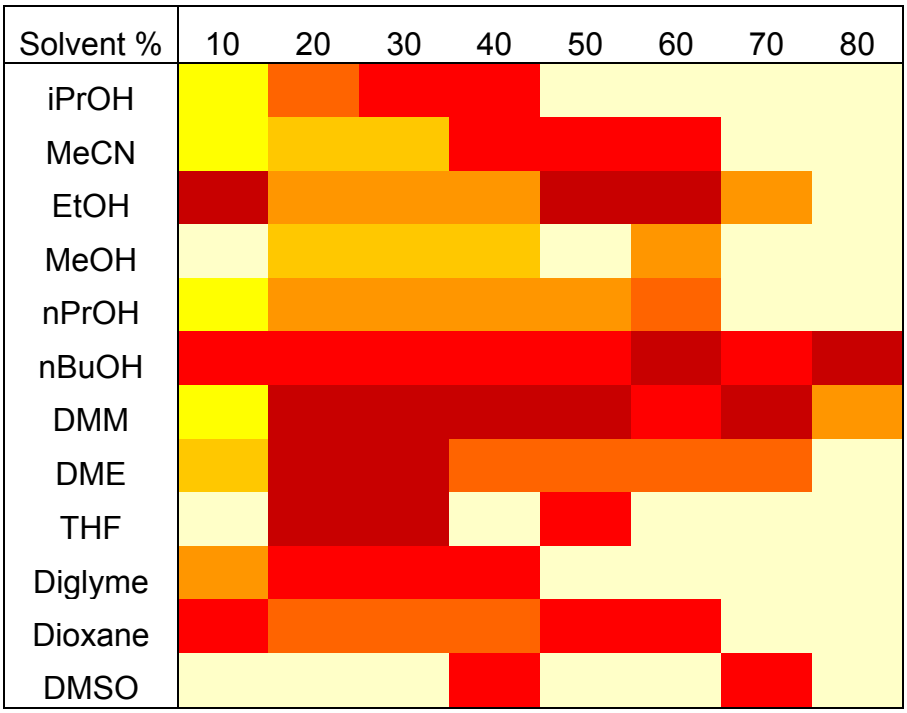

Figure S11. With thiomalic acid as the ligand (arranged by density)

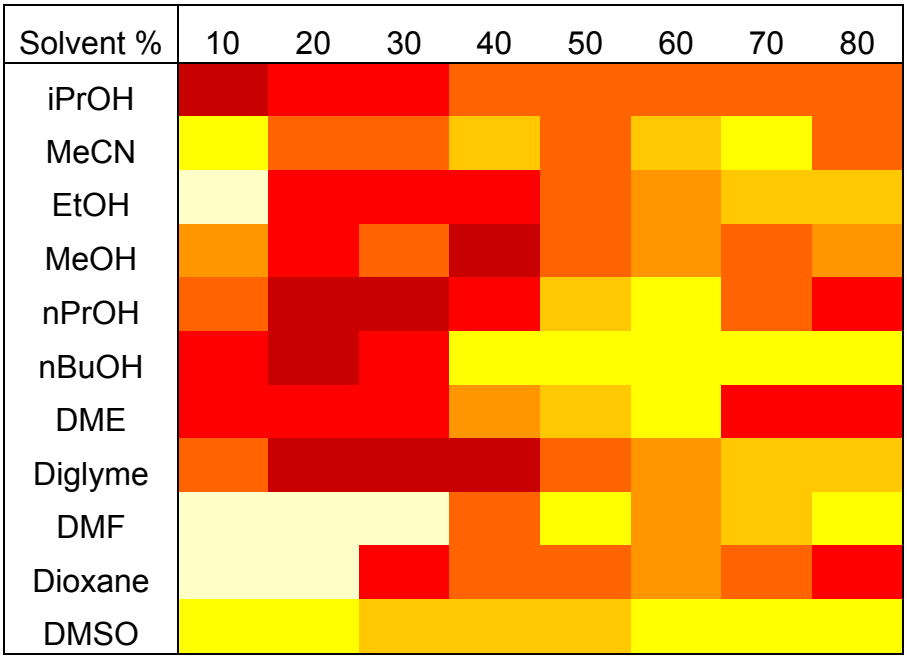

Figure S12. With glutathione as the ligand

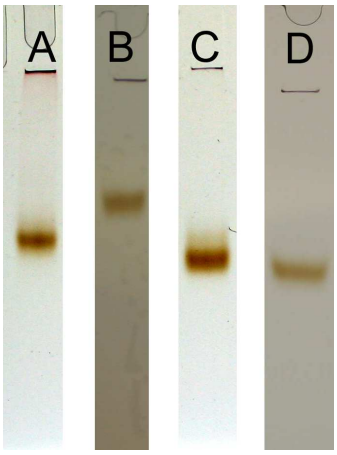

Figure S13. Monodispersed products as synthesized after the refinement process. Solvent conditions: A – 40% *n*BuOH, B – 20% THF, C – 30% DMM, D – 20% DME.

The reaction parameters of four solvent conditions from the thiomalic acid solvent screen were slightly adjusted (Au:Tm ratio, method of addition, order of addition, pH and/or [NaOH], and [BH_4^-]) and was upscaled to 5 μmol scale from 0.5 μmol scale. A reasonable amount of monodispersed product was obtained from each of these reactions, however, we were not able to assign molecular formula to these compounds. The final conditions that yield monodispersed products are A) 40% *n*BuOH, 1:1 Au:Tm, 1 equivalent BH_4^-, reduction at rt for 3 h; B) 20% THF, 1:1 Au:Tm, 0.5 equivalent BH_4^-, reduction at rt for 3 h; C) 30% DMM, 1 equivalent BH_4^-, reduction at rt for 3 h; D) 20% DME, 0.3 equivalent BH_4^-, reduction at rt for 3 h (Figure 5). All these products run faster in PAGE in comparison to Au_{102}*p*MBA_{44}.

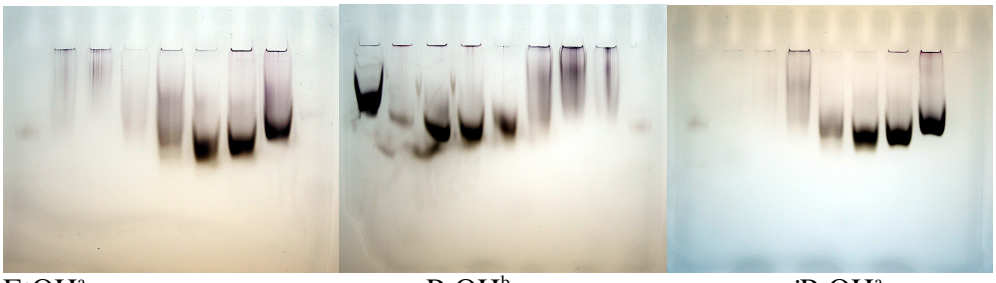

EtOH[a] *n*PrOH[b] *i*PrOH[a]

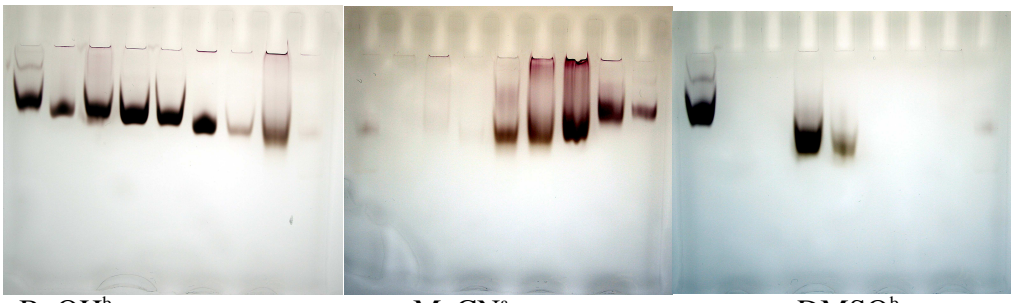

*n*BuOH[b] MeCN[a] DMSO[b]

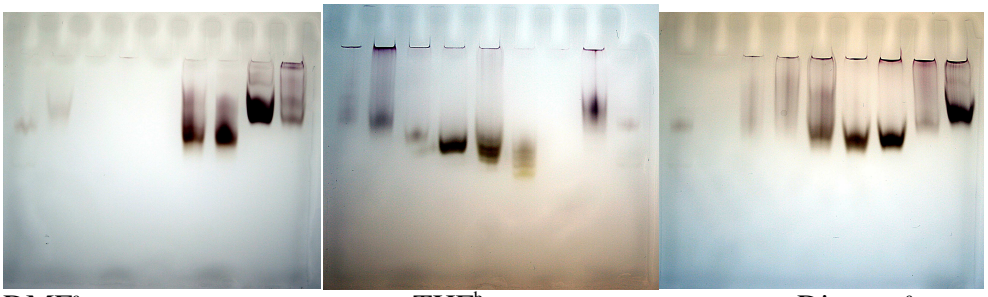

DMF[a] THF[b] Dioxane[a]

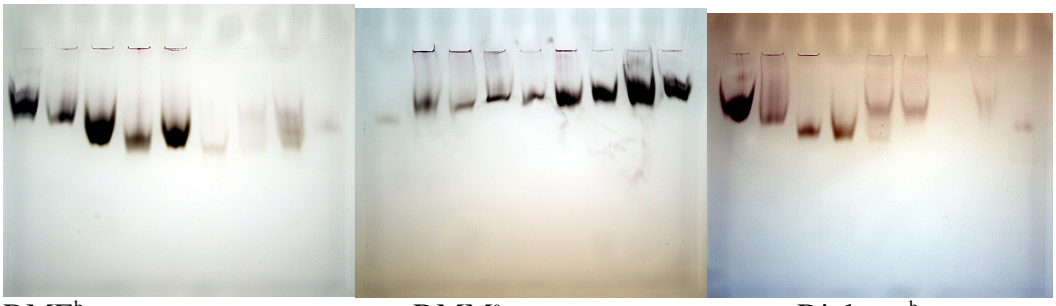

DME[b] DMM[a] Diglyme[b]

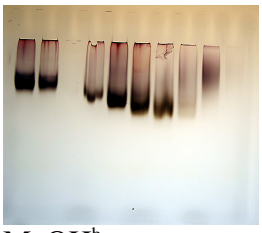

MeOH[b]

Figure S14. Original PAGE images of the solvent screen with *p*MBA as the ligand (increasing solvent concentration from 10% to 80% from left to right)

[a] First lane is $Au_{102}pMBA_{44}$ and $Au_{144}pMBA_{60}$ standards

[b] Last lane is $Au_{102}pMBA_{44}$ and $Au_{144}pMBA_{60}$ standards

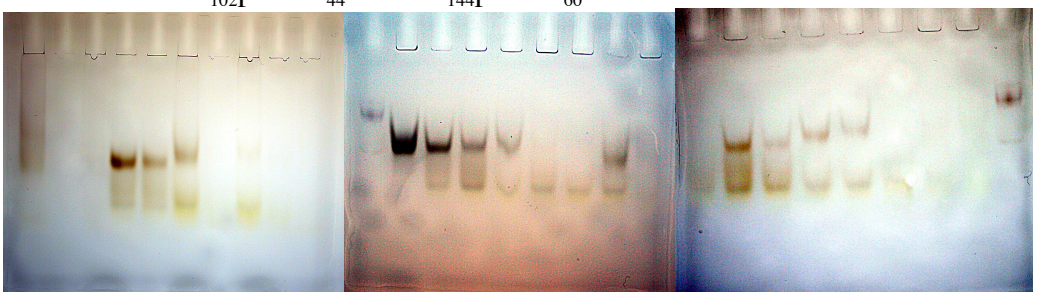

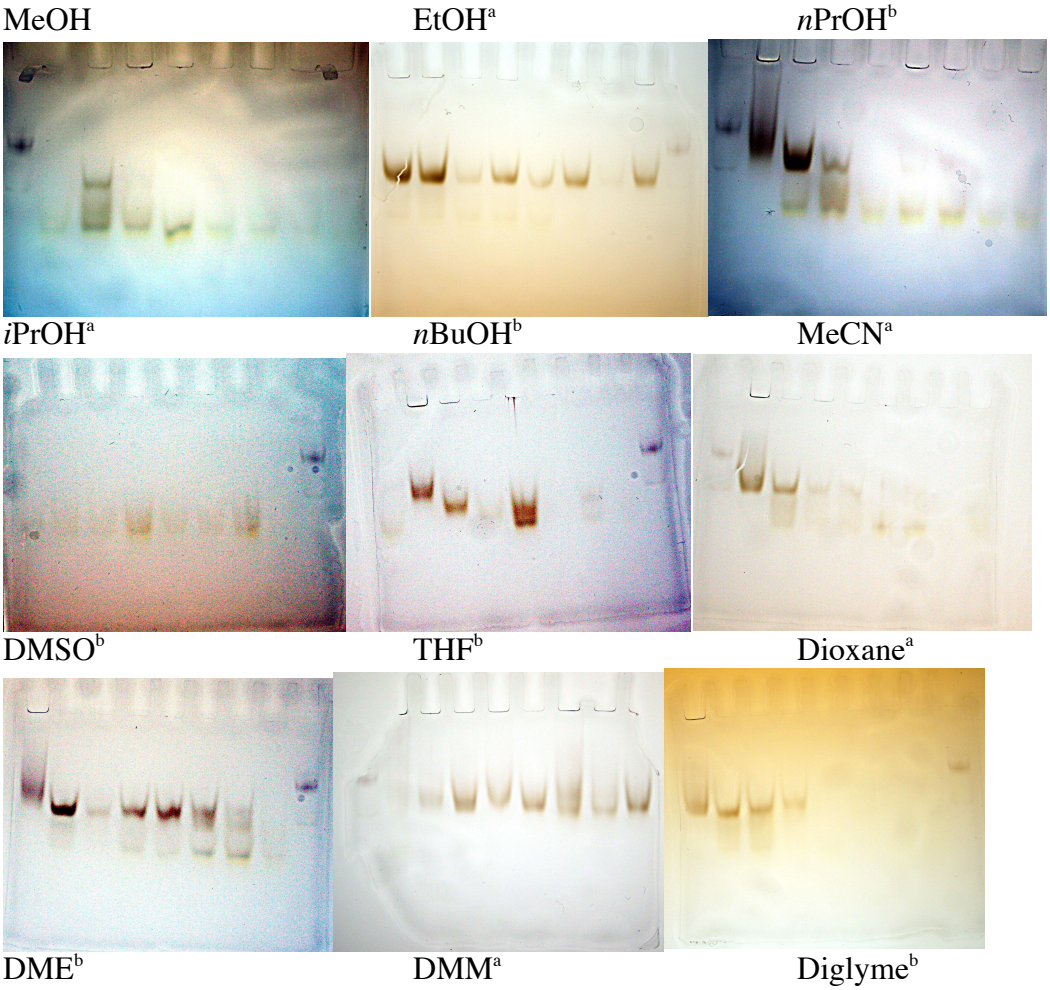

Figure S15. Original PAGE images of the solvent screen with thiomalic acid as the ligand (increasing solvent concentration from 10% to 80% from left to right)
[a] First lane is $Au_{102}pMBA_{44}$ and $Au_{144}pMBA_{60}$ standards
[b] Last lane is $Au_{102}pMBA_{44}$ and $Au_{144}pMBA_{60}$ standards

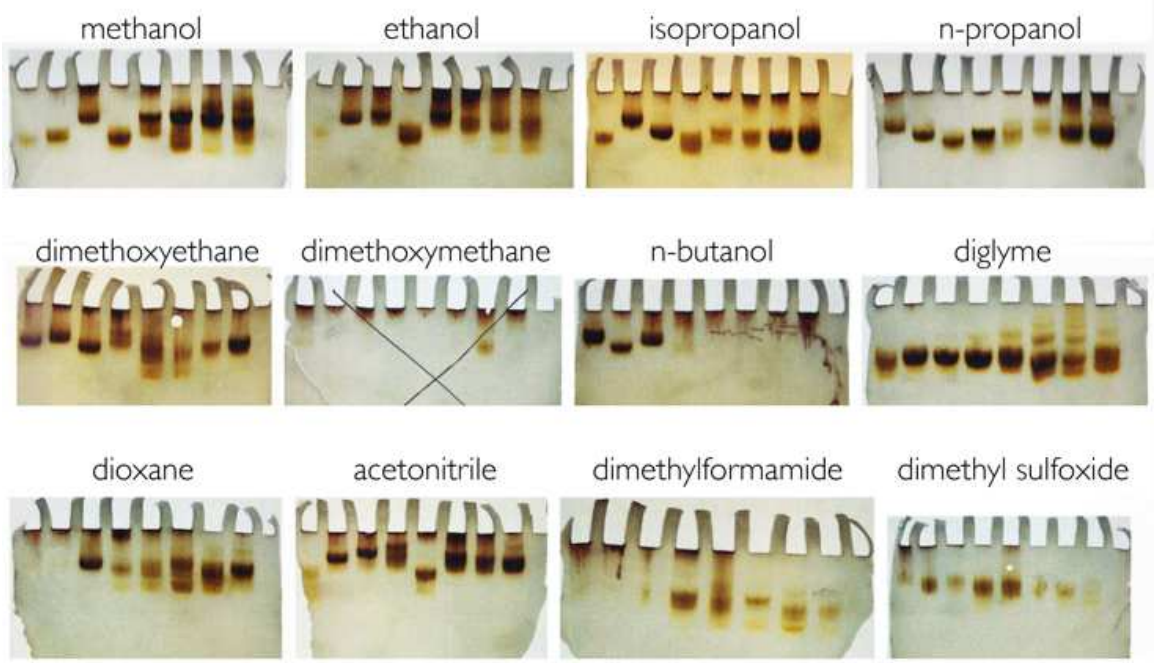

Figure S16. Original PAGE images of the solvent screen with glutathione as the ligand

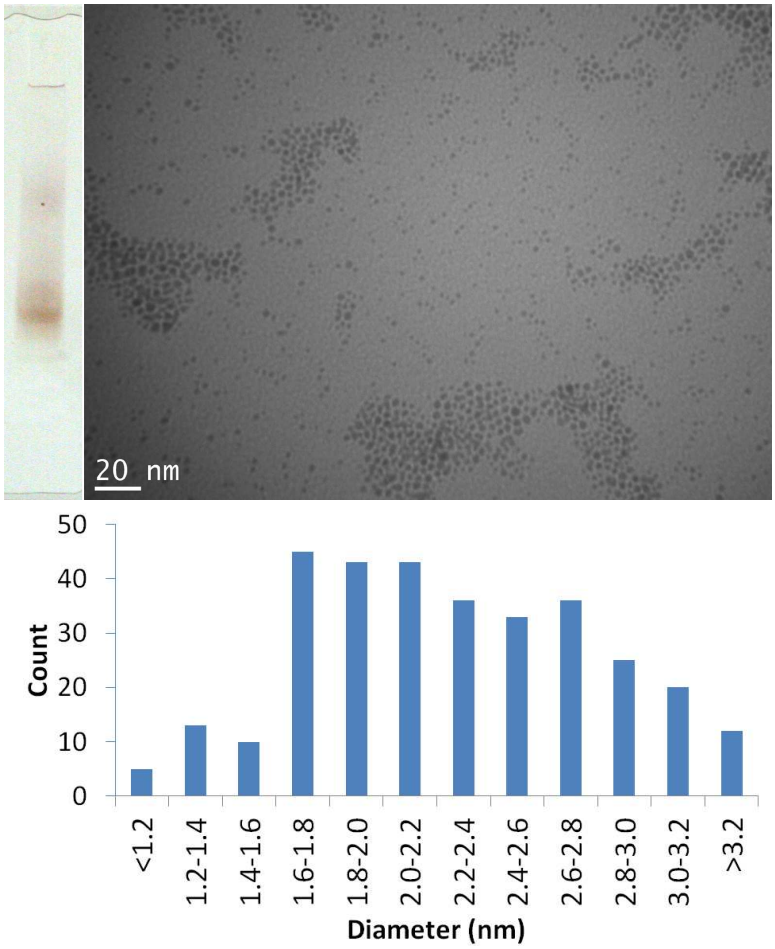

Figure S17. PAGE, TEM image, and histogram of the *p*MBA protected-AuNP synthesized using 40% *i*PrOH.
Particle size: 2.30 nm ± 0.59 nm.

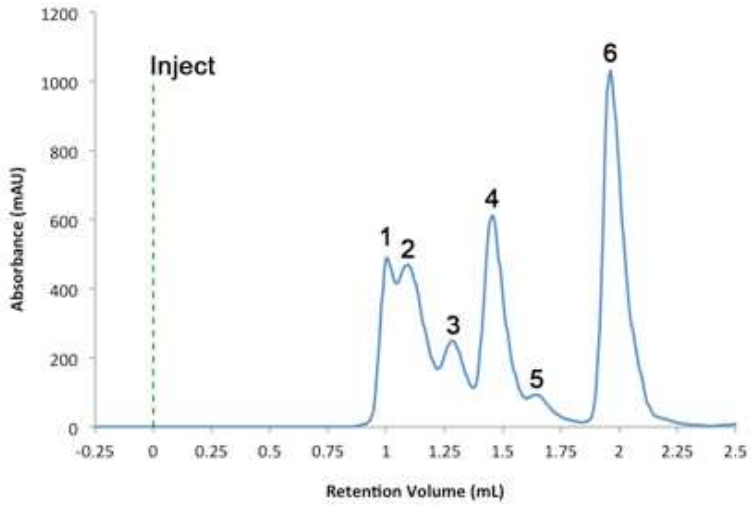

Peak #	Compound	Mass (Da)	Stokes Radius (nm)	Ret. Vol. (mL)
1	Thyroglobulin	670,000	8.6	1.00
2	γ-globulin	158,000	5.1	1.09
3	Ovalbumin	44,000	2.8	1.28
4	Myoglobin	17,000	1.9	1.46
5	Aprotinin	6,500	1.35	1.64
6	Vitamin B12	1,350	0.85	1.96

Figure S18. Standard calibration curve of proteins with mass ranging from 1350 Da to 67000 Da.

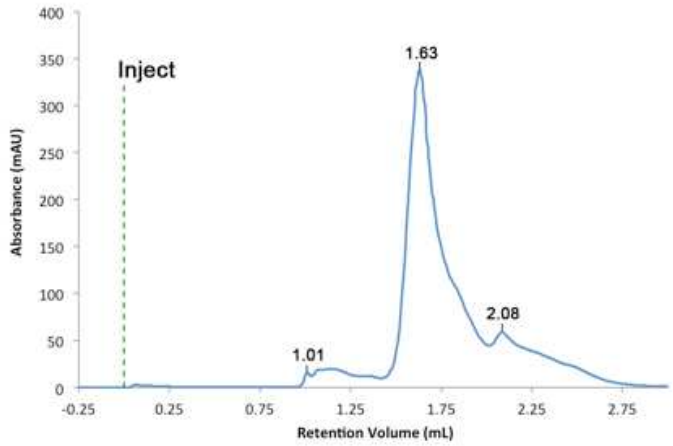

Figure S19. Chromatogram of the Au cluster synthesized with 76% diglyme

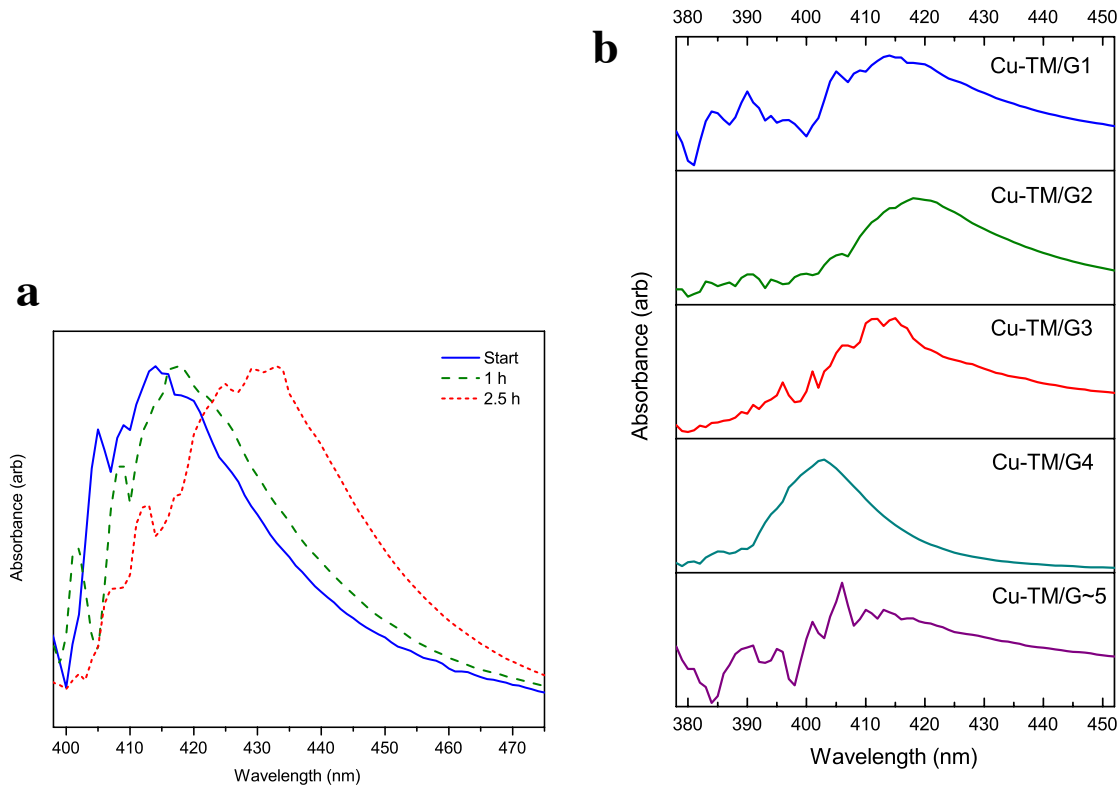

Figure S20. Raw linear absorption (a) of Cu-TM/G*n* while drying and (b) comparison between Cu-TM/G*n*. Data presented in the main text (Figure 11) were smoothed under Savitzky-Golay method with a 10-point window.

Figure S21. Polyacrylamide gel electrophoresis of $Au_{102}(p\text{MBA})_{44}$ that shows the purity of the compound.

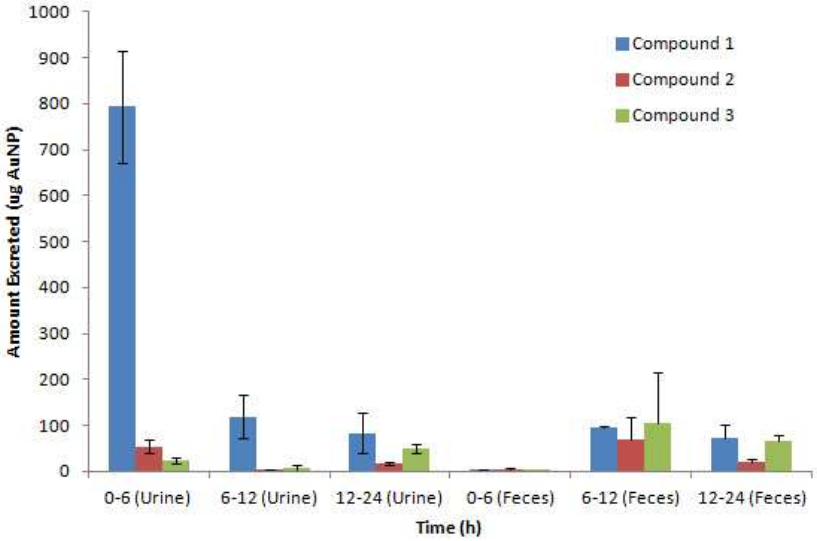

Figure S22. Relative amounts of compounds **1**-**3** in urine and feces at 6, 12, and 24 hours post injection time.

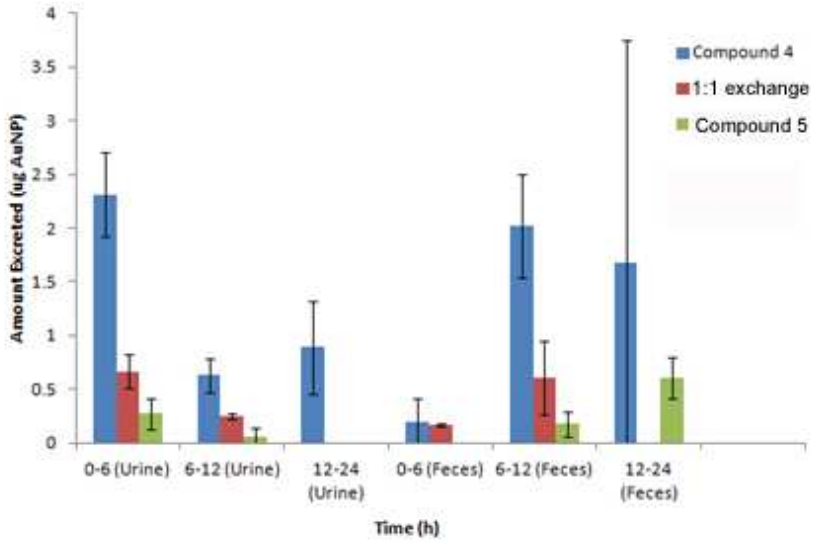

Figure S23. Relative amounts of compounds **4**,**5**, and the 1:1 exchange Au_{102}-based compound (Au_{102}*p*MBA_{44} exchanged with HS-$(CH_2)_{11}$-EG_4-OH) in urine and feces at 6, 12, and 24 hours post injection time.

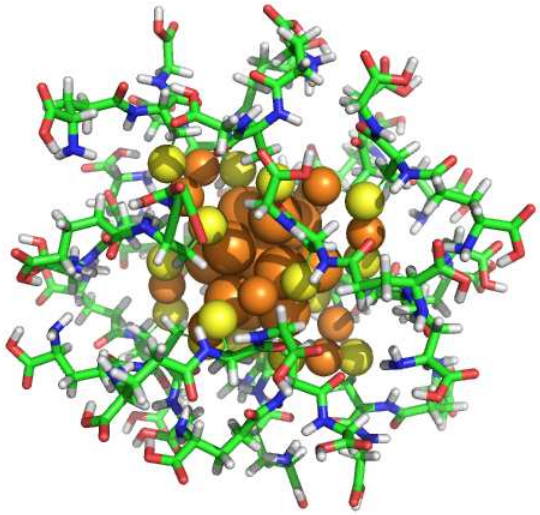

Figure S24. $Au_{25}(GSH)_{18}$, Compound **1**

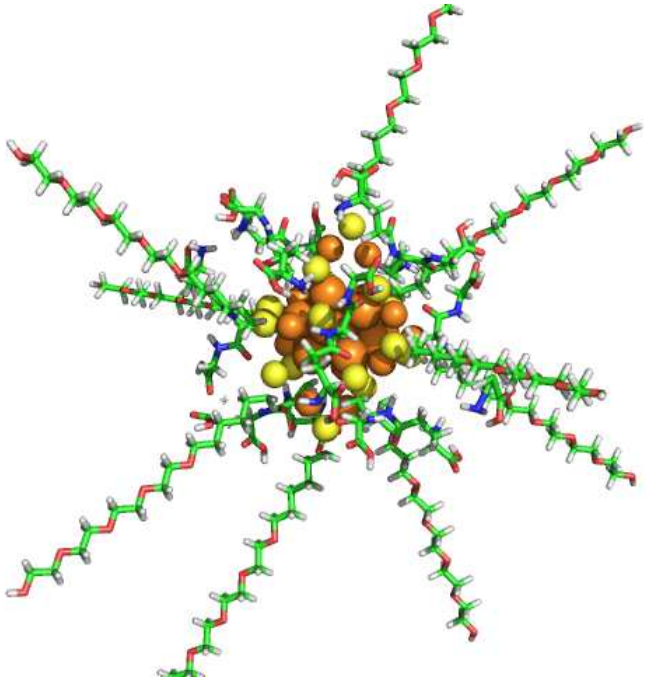

Figure S25. $Au_{25}(GSH)_9(OEG)_9$, (OEG = HS-$(CH_2)_6$-EG-OH), Compound **2**

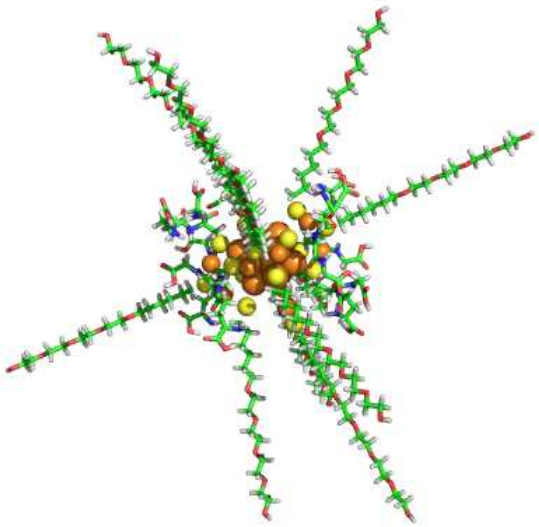

Figure S26. $Au_{25}(GSH)_6(OEG)_{12}$, (OEG = HS-$(CH_2)_6$-EG-OH), Compound **3**

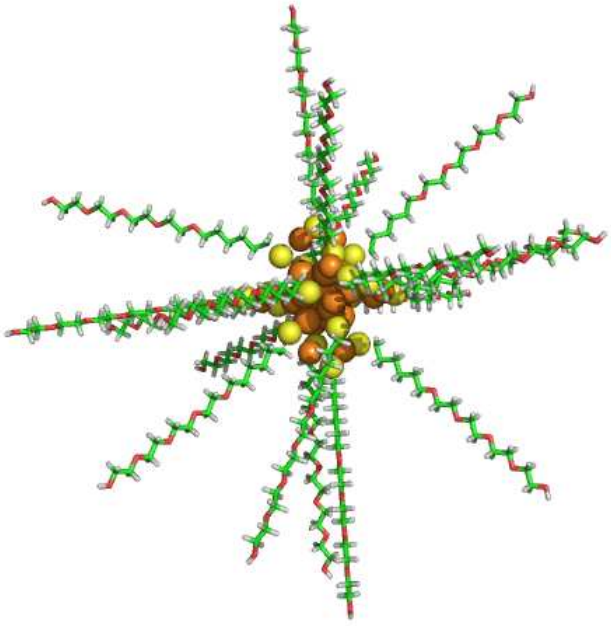

Figure S27. $Au_{25}(OEG)_{18}$, (OEG = HS-$(CH_2)_6$-EG-OH)

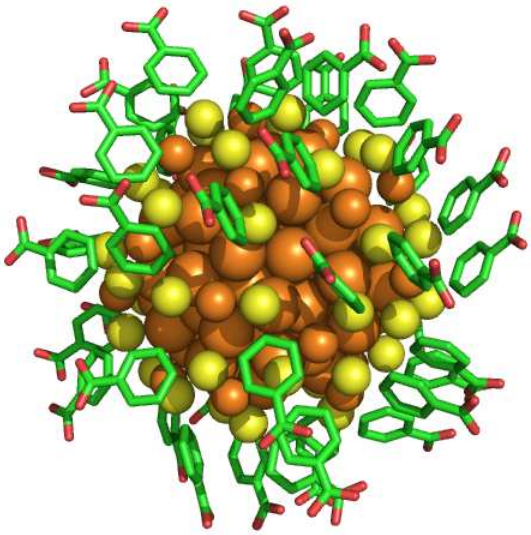

Figure S28. $Au_{102}(p\text{MBA})_{44}$, Compound **4**

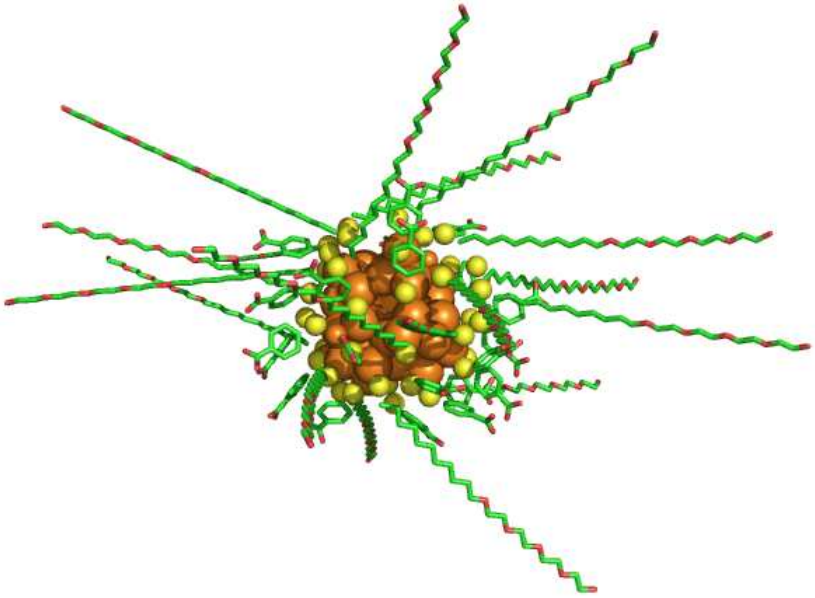

Figure S29. $Au_{102}(p\text{MBA})_{25}(\text{OEG})_{19}$, (OEG = $HS\text{-}(CH_2)_{11}\text{-EG-OH}$), Compound **5**

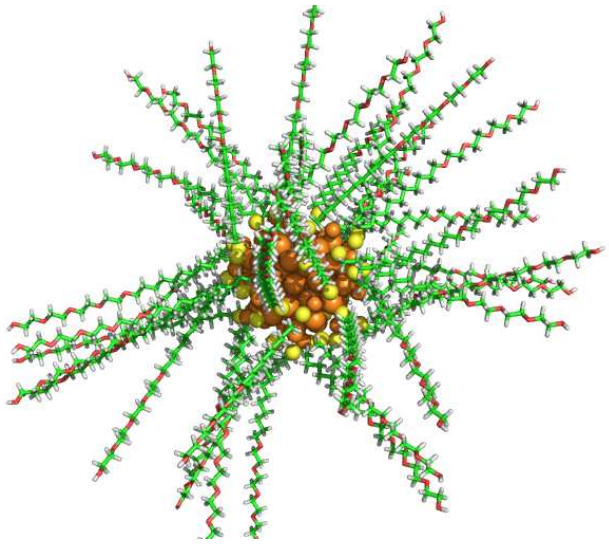

Figure S30. $Au_{102}(OEG)_{44}$, (OEG = HS-$(CH_2)_{11}$-EG-OH)

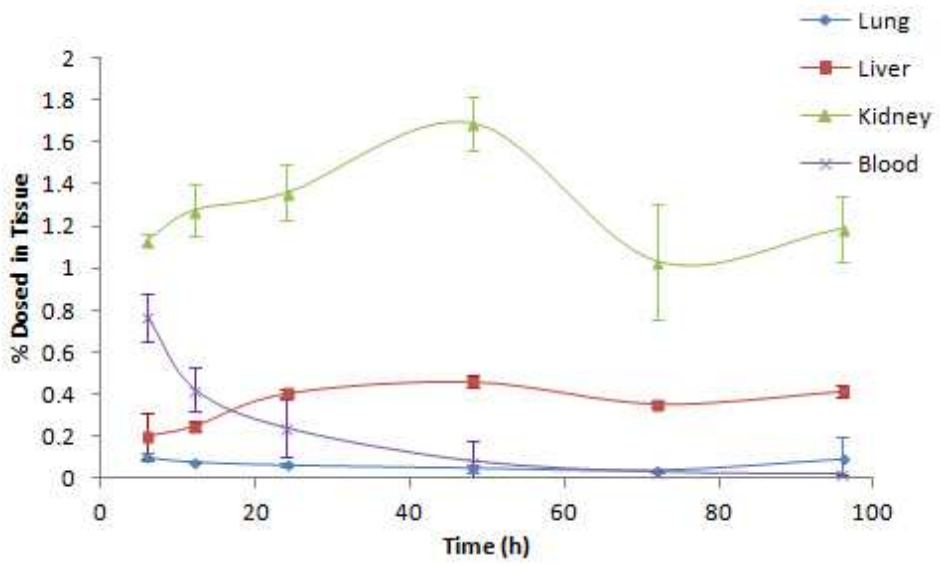

Figure S31. Percent dosed in tissue for compound **1** at noted post-injection time points.

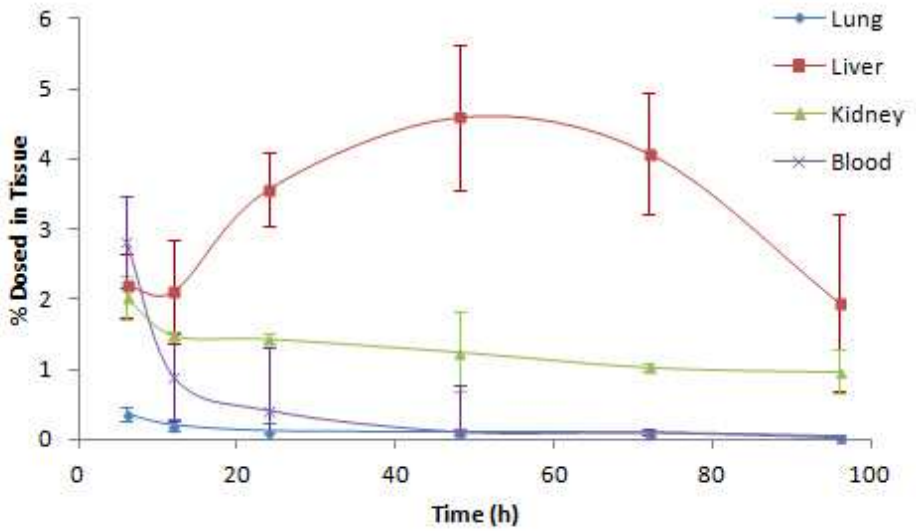

Figure S32. Percent dosed in tissue for compound **2** at noted post-injection time points.

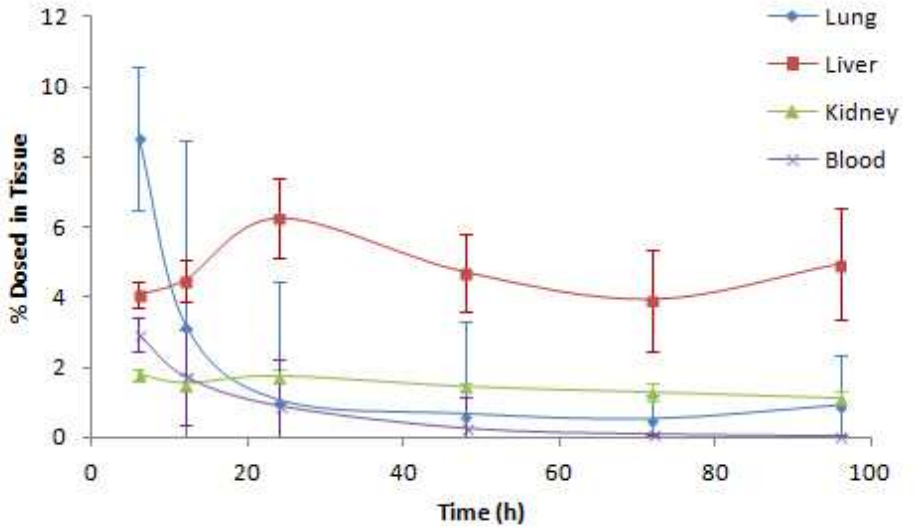

Figure S33. Percent dosed in tissue for compound **3** at noted post-injection time points.

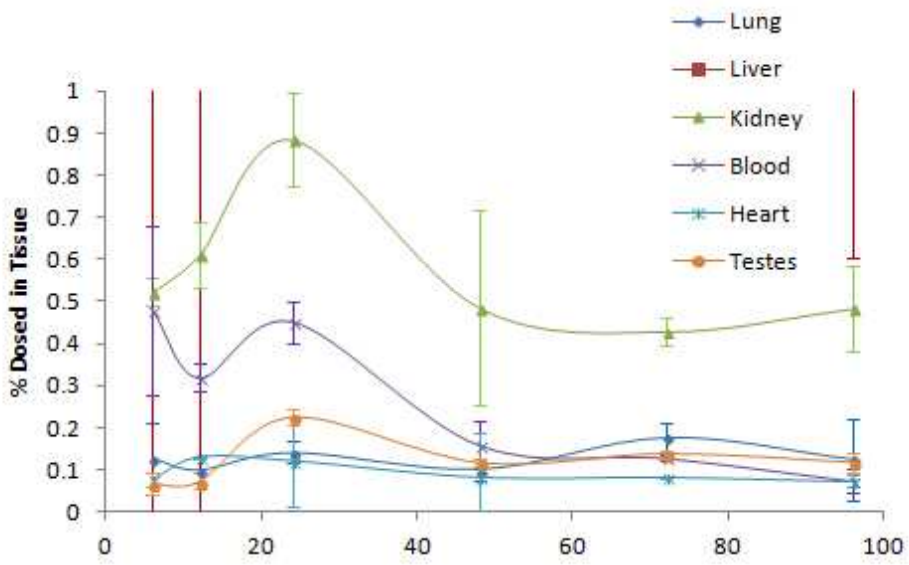

Figure S34. Percent dosed in tissue for compound **4** at noted post-injection time points. Data points of liver are not included.

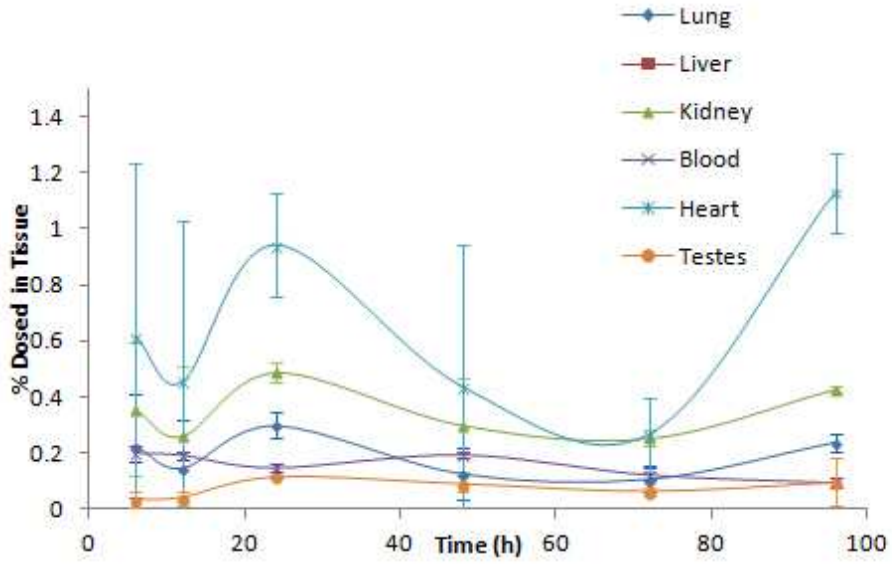

Figure S35. Percent dosed in tissue for compound **5** at noted post-injection time points. Data points of liver are not included.

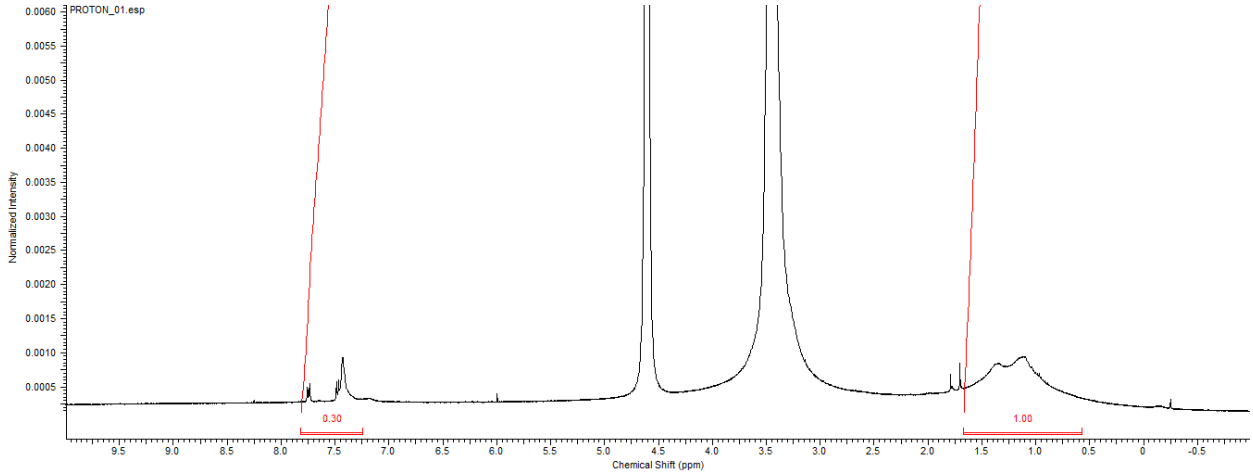

Figure S36. ^{1}H NMR of compound **5**

Table S2 Information on Au_{102}-based 1:1 exchanged compound

Calculated Stokes Diameter (nm)[a]	Net Surface Charge (e^-)	Surface Charge Density (Charge/Å^2)	Hydrophobic Surface Area (%)	Expected Clearance Mechanism % Renal / % RES
5.92	22^-	1.8×10^{-4} (-)	74%	40 / 60

Ligand exchange reaction of $Au_{102}(pMBA)_{44}$ with 23-mercapto-3,6,9,12-tetraoxatricosan-1-ol [HS-$(CH_2)_{11}$-EG_4-OH]

A 500 μM solution of $Au_{102}p$MBA$_{44}$ (6.6 μmol, 178 mg in 13.37 mL H_2O) and a 0.1 M solution of HS-$(CH_2)_{11}$-EG_4-OH (0.79 mmol, 304 mg in 7.90 mL THF) were prepared. For the 1:1 incoming ligand:outgoing ligand reaction: 3 mL of $Au_{102}p$MBA$_{44}$ solution and 0.66 mL of HS-$(CH_2)_{11}$-EG_4-OH solution were mixed and diluted with H_2O to a final volume of 15 mL. Then the reaction was shaken at rt for 1 h, then the crude product was purified by ultrafiltration spin columns (5000 Da cutoff) and was washed with 3 x 10 mL 1:1 H_2O:MeOH. The remaining orange liquid was placed into a 15 mL conical and lyophilized until dry.

The Au_{102}-based 1:1 exchanged compound was dissolved in 5% DMSO, 5% Tween-80 in 90% D5W solution. The particle solutions were filtered through a 0.45 micron filter, and the dosage concentrations were determined after the filtration step. Approximate dosage concentration for this compound was 3.14×10^{-5} M.

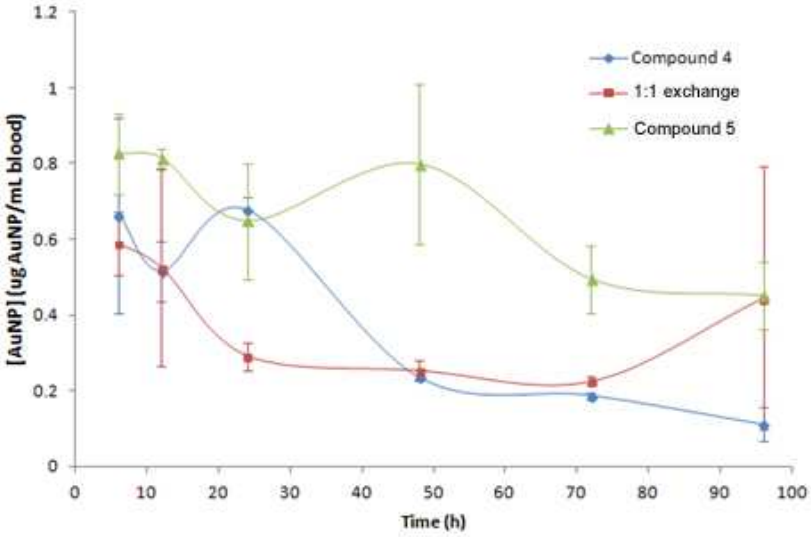

Figure S37. Blood drug concentration vs. time curves of Au_{102}-based compounds

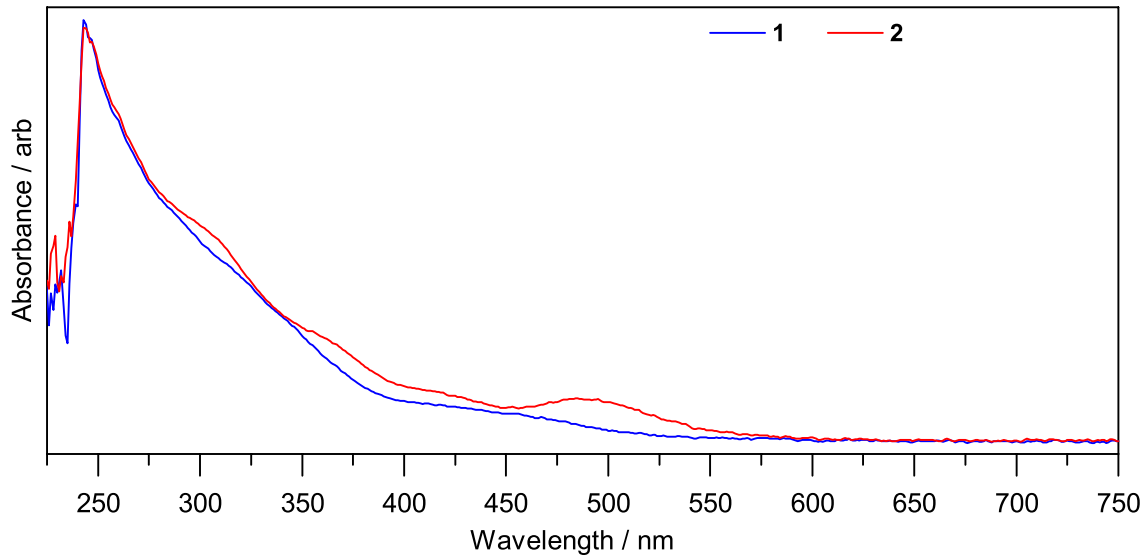

Figure S38. Normalized linear absorbance of **1** and **2** in $CHCl_3$.